ELSEVIER

Comput. Methods Appl. Mech. Engrg. 132 (1996) 63–116

Computer methods in applied mechanics and engineering

Two scale analysis of heterogeneous elastic-plastic materials with asymptotic homogenization and Voronoi cell finite element model

Somnath Ghosh *, Kyunghoon Lee [1], Suresh Moorthy [1]

Applied Mechanics Section, The Ohio State University, Columbus, OH 43210, USA

Received 31 July 1995

Abstract

In this paper, a multiple scale finite element model (VCFEM-HOMO) has been developed for elastic-plastic analysis of heterogeneous (porous and composite) materials by combining asymptotic homogenization theory with the Voronoi Cell finite element model (VCFEM). VCFEM for microstructural modeling originates from Dirichlet tessellation of representative material elements at sampling points in the structure. Structural modeling is done by the general purpose finite element code ABAQUS, and interfacing with the microscale VCFEM analysis is done through the user subroutine in ABAQUS for material constitutive relation, UMAT. Asymptotic homogenization in UMAT generates macroscopic material parameters for ABAQUS. Following the macroscopic analysis, a local VCFEM analysis is invoked to depict the true evolution of microstructural state variables. Various numerical examples are executed for validating the effectiveness of VCFEM-HOMO, and the effect of size, shape and distribution of heterogeneities on local and global response is examined.

1. Introduction

The last three decades have experienced a surge in the advancement of science and technology for heterogeneous materials that contain dispersions of multiple phases in the microstructure. Examples are metal/alloy systems with second phase in the form of precipitates and pores, and composite materials containing a dispersion of fibers, whiskers or particulates in the matrix. In alloy systems, precipitates and pores are results of conventional processing routes. In reinforced composites, stiff, strong and brittle second phase inclusions, e.g. silicon carbide, boron or aluminum oxide, etc. are added to titanium, nickel or aluminum matrices to enhance flow strength, creep resistance and wear resistance of structures. These functionally superior materials have found increasing utilization in the aerospace, automotive, materials and ordnance industries for replacing some of the traditionally used structural materials. The degree of mechanical and thermal property enhancements depends on the size, shape and properties of the second phase, as well as on their spatial distribution within the matrix. For example, ductility is reduced with increasing volume fraction of reinforcements in metal-matrix composites. Christman et. al. [1] have shown that local plastic flow is highly sensitive to shape of the reinforcements under identical global stresses.

---

[*] Corresponding author. Associate Professor.

[1] Graduate Research Associate.

0045-7825/96/$15.00 © 1996 Elsevier Science S.A. All rights reserved

SSDI 0045-7825(95)00974-4

It is clear that rigorous fundamental studies are warranted for understanding deformation and failure mechanisms prior to design of advanced materials in high performance applications. Studies reflecting the details of actual heterogeneous microstructures are indispensable in this respect. It is through these models, that the effect of second phase shapes, sizes and distributions on evolving state variables like stresses, plastic strains, void initiation and growth, and evolving material variables like strain hardening and flow stress can be investigated.

A number of analytical micromechanical models for predicting macroscopic response have evolved within the framework of small deformation linear elasticity theory. Notable among them are models based on: (i) variational approach using extremum principles [2, 3], (ii) probabilistic approach [4], (iii) self-consistent schemes [5, 6] and (iv) the generalized self consistent model [7, 3]. These models follow the idea of equivalent inclusion methods based on eigenstrain formulation. Though analytical micromechanical models are reasonably effective in predicting equivalent material properties for relatively simple geometries and low volume fractions, they are often incapable in depicting the evolution of stresses and strains in the microstructure. Arbitrary microstructural morphology, that are frequently encountered in actual materials cannot be deterministically treated with these models. Constitutive response of the constituent phases are also somewhat restricted and predictions with large property mismatches are not very reliable. Additionally, due to lack of proper representation of microscopic stresses and strains, they cannot capture the effect of local inhomogeneities on damage and failure. The state of the art in analytical modeling for ductile materials is not as mature. Important contributions have been made by Tandon and Weng [8] for small strain, deformation theory of elasto-plasticity of metals with elastic particles, and by Dvorak and Bahei-El-Din [9, 10] for rate-independent plastic matrix and elastic fibers using a 'vanishing fiber diameter' model, and more recently, the bimodal plasticity theory. Paley and Aboudi [11] have developed a semi-analytical generalized method of cells for elastic-plastic and viscoplastic materials, while Nemat-Nasser and coworkers [12] have used Fourier series expansions to develop elastic-plastic and creep models. The applications of these non-linear models to complex microstructures in many real materials are even less effective than the linear models. This is substantiated by the fact that when plastic flow occurs, the deformation is no longer homogeneous. Local properties become stress dependent and the overall constitutive response is influenced by the distributions and shapes of second phase.

Intractability of analytical models in situations of arbitrary phase dispersions have necessitated the introduction of *Unit Cell* formulations [1, 13, 14] using computational methods. These models generate overall material response through detailed discretization of a representative volume element (RVE) of the composite microstructure. In unit cell models, global properties are ascertained by assuming macroscopic periodicity conditions on the RVEs. Despite their widespread success, the unit cell models are faced with some shortcomings in modeling real materials, stemming from global and local periodicity assumptions. Global periodicity assumes that the same RVE is valid for all points of a structure, which is not realistic for many commercial materials. A majority of these models also make assumptions of 'perfect' local periodicity and uniform distribution of the second phase. Effectively, this local periodicity assumption can reduce the representative volume element (RVE) to a basic structural element (BSE), thereby making the unit cells very simple. A basic structural element is defined as the smallest element of the microstructure reflecting basic geometrical features (see Fig. 1(c)). Micrographs of many real materials often show arbitrariness in distribution (Fig. 1(b)) thereby making this assumption too restrictive. Another limitation is that unit cell models typically formulate constitutive relations based on a single RVE subjected to a given load history. This makes them amenable to misrepresentation of the actual interaction between macro- and micro-scale deformations. This calls for simultaneous computations at *multiple levels* for concurrent evolution of macroscopic and microscopic variables.

In the 1970s a mathematical theory called **Asymptotic Homogenization Theory** [15, 16], originated for analyzing physical systems containing two or more length scales. It is suitable for multi-phase materials in which the natural scales are the microscopic scale characterized by inter-heterogeneity/local discontinuity spacing and the macroscopic scale characterizing overall dimensions of the structure. This method is based on asymptotic expansions of displacement and stress fields about their respective macroscopic values and uses variational principles for creating a link between scales. Resulting boundary value problems at the macroscopic and microscopic levels are solved by invoking numerical methods at both levels. Fig. 1 shows the various levels in a structure and its corresponding computational model. Computer

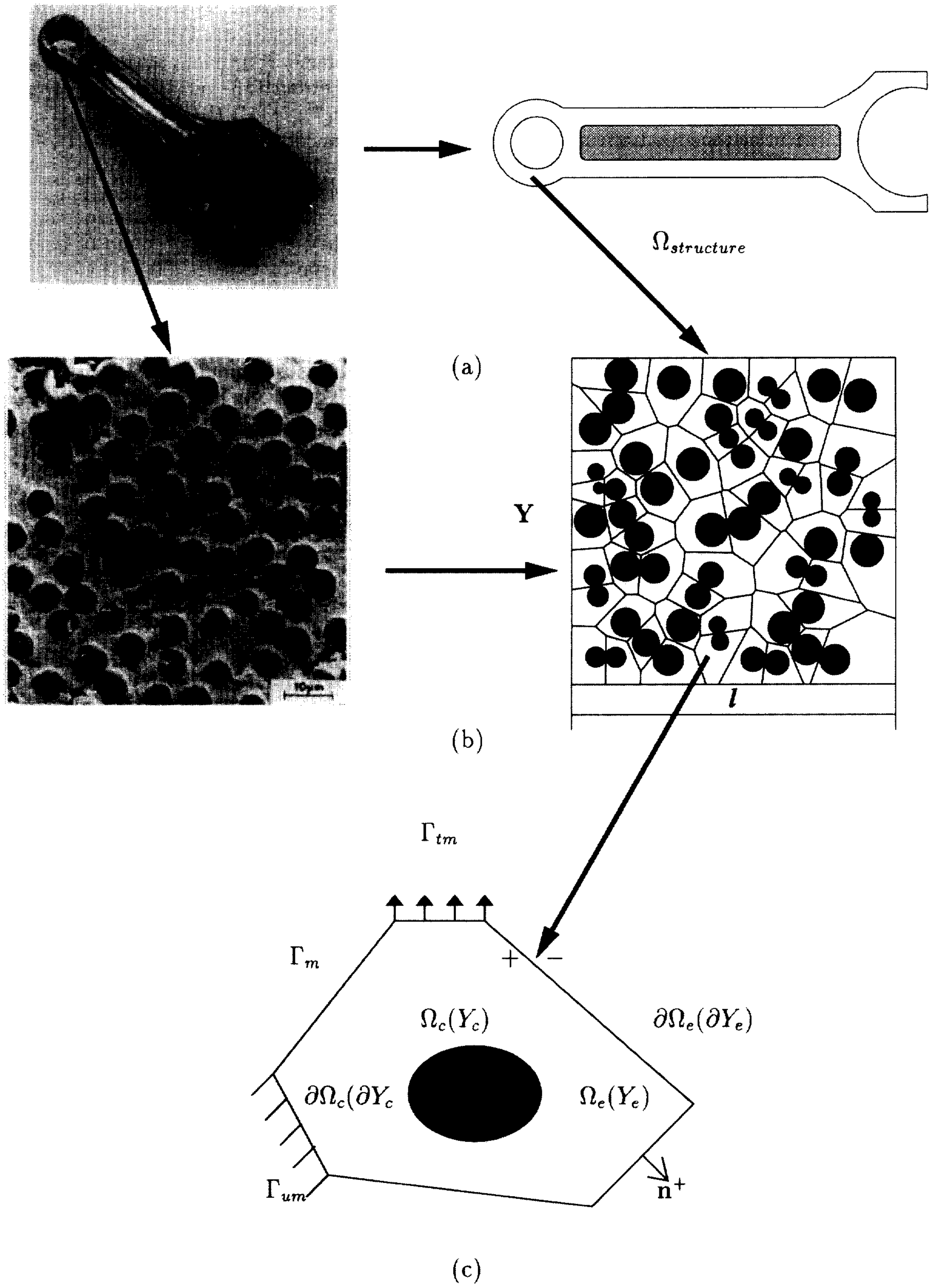
Ωstructure
(a)
Y
10μm
l
(b)
Γtm
Γm
+
−
Ωc(Yc)
∂Ωe(∂Ye)
∂Ωc(∂Yc
Ωe(Ye)
Γum
n+
(c)

Fig. 1. A heterogeneous structure with various levels. (a) The global structure and the computational geometry; (b) representative material elements (RME) at a point and the corresponding VCFE model; (c) a basic structural element represented by a Voronoi Cell.

simulations simultaneously provide global response through homogenized material parameters and averaged stress/strain fields, and microstructural behavior through a depiction of local stress/strain fields. This method can overcome shortcomings inflicted by global periodicity restrictions in unit cell models. The analysis however, makes the assumption of local periodicity through the introduction of spatially repeated microscopic cells.

The finite element method has been successfully applied in conjunction with the homogenization theory for analysis of linear elastic, particulate and fiber reinforced composites by Toledano and Murakami [17] and by Guedes and Kikuchi [18, 23]. These models are constructed by considering very simple unit cells that represent uniform distributions in the microstructure. For non-linear regimes, homogenization theories have been established by Suquet [19]. Important contributions to the application of homogenization method in finite deformation elasto-plasticity has been made by Guedes [20] and Cheng [21]. The method has been extended to model damage evolution by fiber rupture for linear elastic materials in [25]. A comprehensive review of this method for various problems is presented in [22]. In spite of its promise, the homogenization theory has not enjoyed a wide acceptance thus far. A prime reason is the assumptions of over-simplified microscopic RVEs for reducing enormous computing costs.

The material based *Voronoi Cell Finite Element Model* (VCFEM) [26–30], developed by Ghosh and coworkers, attempts to overcome difficulties in modeling arbitrary microstructures by conventional finite element methods. The VCFEM mesh evolves naturally from a heterogeneous microstructural material element (RME) by *Dirichlet tessellation* into a network of multi-sided 'Voronoi' polygons. The polygons contain one second phase inclusion each, at most as shown in Fig. 1(b). A robust mesh generator to create these polygons based on shape, size and location of the heterogeneities is developed in [30]. The multi-phase Voronoi polygons, identified with the basic structural elements as depicted in Fig. (1c), constitute elements in VCFEM. Element formulations have been developed for micropolar thermo-elasticity problems in [29], and for elastic-plastic problems in [26, 27]. VCFEM with asymptotic homogenization for elastic problems have been presented in [28].

This paper presents a coupled multiple scale computational model for heterogeneous elastic-plastic structures. Only two-dimensional problems are considered. Microstructural analysis for various different representative material element arrangements, is done with the Voronoi Cell finite element model. The commercial general purpose code ABAQUS [31] is used for global analysis at the level of overall structural geometry and applied loads. The interfacing between macro- and micro-calculations are done through the user subroutine window UMAT in ABAQUS. Numerical examples are conducted to investigate the advantages of coupled multiple scale analysis over other unit cell and continuum based theories. Effect of shapes, sizes and locations of microscopic inclusions on the structural performance and the evolution of microstructural stresses and strains are also studied.

2. Asymptotic homogenization for multiple scale analysis

Consider a heterogeneous body occupying a region $\Omega_{\text{structure}}$ in Fig. 1(a), for which the microstructure constitutes of spatially periodic representative material elements (RMEs) as shown in Fig. 1(b). Only small deformation elastic-plastic deformation of the body is considered in the absence of inertia. The body is subjected to a system of time/load dependent body forces $\boldsymbol{f}(t)$, surface tractions $\boldsymbol{t}(t)$ on the boundary Γ_t and prescribed displacement fields on the boundary Γ_u. In real heterogeneous materials, dimensions of the RME of characteristic length l are typically very small in comparison with the dimensions of the body of characteristic length L. The ratio of these microscopic and macroscopic scales l/L is represented by a very small positive number ϵ. When subjected to structural level loads and displacements, the resulting evolutionary variables, e.g. deformation and stresses, vary from point to point at the macroscopic scale $\boldsymbol{x}$. Furthermore, a high level of heterogeneity in the microstructure causes a rapid variation of these variables in a small neighborhood ϵ of the macroscopic point $\boldsymbol{x}$. This corresponds to a microscopic scale $\boldsymbol{x}/\epsilon$ and consequently, all variables are assumed to exhibit dependence on both length scales, i.e. $\Phi^\epsilon = \Phi(i\boldsymbol{x}, \boldsymbol{x}/\epsilon)$. The superscript ϵ denotes association of the function with the two length scales. In this notation, Ω^ϵ corresponds to a connected domain that extends the structural domain to its microstructure. Mathematically speaking,

$$\Omega^\epsilon = \left\{ \boldsymbol{x} \in \Omega : \Theta\left(\frac{\boldsymbol{x}}{\epsilon}\right) = 1 \right\} \tag{1}$$

in which $\Theta(\boldsymbol{y}) = 1$ when $\boldsymbol{y}$ lies in the microscopic RME. In most of the work on homogenization theory [22, 18, 20, 25], a periodic repetition of the microstructure about a macroscopic point $\boldsymbol{x}$ has been assumed, thereby making the dependence of the function on $\boldsymbol{y} = (\boldsymbol{x}/\epsilon)$, periodic. This characteristic is often termed as $\boldsymbol{Y}$-periodicity, where $\boldsymbol{Y}$ corresponds to a RME. The instantaneous tangent modulus tensor E^ϵ_{ijkl}, relating the stress rate (increment) to the strain rate (increment), and the corresponding instantaneous compliance tensor S^ϵ_{ijkl} in the connected domain are expressed as

$$E^\epsilon_{ijkl}(\boldsymbol{x}) = E_{ijkl}(\boldsymbol{x}, \boldsymbol{y}) \quad \text{in } \Omega^\epsilon \tag{2}$$

$$S^\epsilon_{ijkl}(\boldsymbol{x}) = E^{-1}_{ijkl}(\boldsymbol{x}, \boldsymbol{y}) \quad \text{in } \Omega^\epsilon \tag{3}$$

It is assumed that the stress, strain and displacement fields satisfy the rate or incremental forms of the equilibrium equation, kinematic relation, and constitutive relations given as

$$\dot\sigma^\epsilon_{ij,j} = -\dot f_i \quad \text{in } \Omega^\epsilon \tag{4}$$

$$\dot e^\epsilon_{kl} = \frac{1}{2}\left(\frac{\partial \dot u^\epsilon_k}{\partial x^\epsilon_l} + \frac{\partial \dot u^\epsilon_l}{\partial x^\epsilon_k}\right) \quad \text{in } \Omega^\epsilon \tag{5}$$

$$\dot\sigma^\epsilon_{ij} = E^\epsilon_{ijkl}\dot e^\epsilon_{kl} \quad \text{in } \Omega^\epsilon \tag{6}$$

where $\dot u^\epsilon_i = \dot u^\epsilon_i(\boldsymbol{x}, \boldsymbol{y})$ is a $\boldsymbol{Y}$-periodic rate of displacement field in $\boldsymbol{y}$. Furthermore, the boundary conditions are assumed to satisfy the following equations on the prescribed traction and displacement boundaries, respectively.

$$\dot\sigma^\epsilon_{ij} n_j = \dot t_i \quad \text{on } \Gamma_t \tag{7}$$

$$\dot u^\epsilon_i = \dot{\bar u}_i \quad \text{on } \Gamma_u \tag{8}$$

where $\boldsymbol{n}$ is the unit normal to the boundary. Since small deformation is assumed in this analysis, the normal vector does not change significantly with load. In homogenization theory, the $\boldsymbol{Y}$-periodic displacement rate or increment field is approximated by an asymptotic expansion with respect to parameter ϵ:

$$\dot{\boldsymbol{u}}^\epsilon(\boldsymbol{x}) = \dot{\boldsymbol{u}}^0(\boldsymbol{x}, \boldsymbol{y}) + \epsilon\dot{\boldsymbol{u}}^1(\boldsymbol{x}, \boldsymbol{y}) + \epsilon^2\dot{\boldsymbol{u}}^2(\boldsymbol{x}, \boldsymbol{y}) + \cdots, \qquad \boldsymbol{y} = \frac{\boldsymbol{x}}{\epsilon} \tag{9}$$

Noting that the spatial $\boldsymbol{x}^\epsilon$ derivative of any function depends on the two length scales and is given as

$$\frac{\partial}{\partial x^\epsilon_i}\left(\Phi\left(\boldsymbol{x}, \boldsymbol{y} = \frac{\boldsymbol{x}}{\epsilon}\right)\right) = \frac{\partial \Phi}{\partial x_i} + \frac{1}{\epsilon}\frac{\partial \Phi}{\partial y_i} \tag{10}$$

the strain rate tensor may be expressed as

$$\dot e^\epsilon_{kl} = \frac{\partial \dot u^\epsilon_k}{\partial x^\epsilon_l} = \frac{1}{\epsilon}\frac{\partial \dot u^0_k}{\partial y_l} + \left(\frac{\partial \dot u^0_k}{\partial x_l} + \frac{\partial \dot u^1_k}{\partial y_l}\right) + \epsilon\left(\frac{\partial \dot u^1_k}{\partial x_l} + \frac{\partial \dot u^2_k}{\partial y_l}\right) + \cdots \tag{11}$$

Substituting this in the constitutive relation (6), the stress rate $\dot\sigma^\epsilon_{ij}$ can be expanded as

$$\dot\sigma^\epsilon_{ij} = \frac{1}{\epsilon}\dot\sigma^0_{ij} + \dot\sigma^1_{ij} + \epsilon\dot\sigma^2_{ij} + \epsilon^2\dot\sigma^3_{ij}\cdots \tag{12}$$

where

$$\dot\sigma^0_{ij} = E^\epsilon_{ijkl}\frac{\partial \dot u^0_k}{\partial y_l}$$

$$\dot{\sigma}^1_{ij} = E^{\epsilon}_{ijkl}\left(\frac{\partial \dot{u}^0_k}{\partial x_l} + \frac{\partial \dot{u}^1_k}{\partial y_l}\right) \qquad (13)$$
$$\dot{\sigma}^2_{ij} = E^{\epsilon}_{ijkl}\left(\frac{\partial \dot{u}^1_k}{\partial x_l} + \frac{\partial \dot{u}^2_k}{\partial y_l}\right)$$

Putting the expansion of $\dot{\sigma}^{\epsilon}_{ij}$ (12) in the rate form of equilibrium equation (4), and setting each coefficient of ϵ^i $(i = -1, 0, 1, 2, ...)$ to zero, results in the following set of equations.

$$\frac{\partial \dot{\sigma}^0_{ij}}{\partial y_j} = 0$$
$$\frac{\partial \dot{\sigma}^1_{ij}}{\partial y_j} + \frac{\partial \dot{\sigma}^0_{ij}}{\partial x_j} = 0 \qquad (14)$$
$$\frac{\partial \dot{\sigma}^2_{ij}}{\partial y_j} + \frac{\partial \dot{\sigma}^1_{ij}}{\partial x_j} + \dot{f}_i = 0$$

If $\boldsymbol{x}$ and $\boldsymbol{y}$ are considered as independent variables, Eqs. (14) form a recursive system of differential equations for the functions $\dot{u}^0_i, \dot{u}^1_i, \dot{u}^2_i \ldots$ parameterized by $\boldsymbol{x}$. An important result that is used to solve the system of equations (14) is given as follows [24]. The equation

$$-\frac{\partial}{\partial y_i}\left(a_{ij}(y)\frac{\partial \Phi}{\partial y_j}\right) = F \quad \text{in } \boldsymbol{Y} \qquad (15)$$

for a $\boldsymbol{Y}$-periodic function $\Phi = \Phi(\boldsymbol{x}, \boldsymbol{y})$ has a unique solution if the mean value of F, defined by

$$\langle F \rangle = \frac{1}{|\boldsymbol{Y}|}\int_Y F \, \mathrm{d}y = 0 \qquad (16)$$

where $|\boldsymbol{Y}|$ denotes the volume of the RME. Eqs. (14) and (13) together with results (16) leads to the trivial value for $\dot{\sigma}^0_{ij}$, and therefore establishes that $\dot{\boldsymbol{u}}^0$ is only a function of $\boldsymbol{x}$ as shown in [25], i.e.

$$\dot{\sigma}^0_{ij} = 0, \quad \text{and} \quad \dot{u}^0_i = \dot{u}^0_i(\boldsymbol{x}) \qquad (17)$$

2.1. Microscopic equilibrium equation and homogenized constitutive relation

Substituting (17) into the second of Eq. (14) leads to the $\boldsymbol{Y}$-domain equilibrium equation

$$\frac{\partial \dot{\sigma}^1_{ij}}{\partial y_j} = 0 \qquad (18)$$

From Eqs. (6), (11) and (12), by neglecting the terms associated with ϵ or higher, the constitutive relation in $\boldsymbol{Y}$ is expressed as

$$\dot{\sigma}^{\epsilon}_{ij} = \dot{\sigma}^1_{ij} = E^{\epsilon}_{ijkl}\dot{e}^{\epsilon}_{kl} \qquad (19)$$

where

$$\dot{e}^{\epsilon}_{kl} = \dot{\bar{e}}_{kl} + \dot{e}^*_{kl} = \frac{\partial \dot{u}^0_k}{\partial x_l} + \frac{\partial \dot{u}^1_k}{\partial y_l} \qquad (20)$$

Here, $\dot{e}^{\epsilon}_{kl}$ is the local or microstructural strain rate tensor, for which $\dot{\bar{e}}_{kl} = \partial \dot{u}^0_k / \partial x_l$ is an averaged macroscopic part, and $\dot{e}^*_{kl} = \partial \dot{u}^1_k / \partial y_l$ is denoted as a fluctuating strain rate tensor [32]. With the equilibriated microscopic stress rate $\dot{\sigma}^1_{ij}$ and displacement rate $\dot{u}^1_k$ fields completely determined by Eqs. (18)–(20), a local structure tensor denoted by M^{kl}_{pm} is calculated by applying a unit components of a macroscopic strain rate tensor. The local structure tensor M^{kl}_{pm} is used to establish a relation between the local microscopic strain rate $\dot{e}^{\epsilon}_{kl}$, and the macroscopic strain rate $\dot{\bar{e}}_{kl}$ as

$$\dot{e}^{\epsilon}_{kl} = M^{kl}_{pm}\dot{\bar{e}}_{pm} \tag{21}$$

Due to linearity of the rate(incremental) problem, $\dot{\sigma}^1_{ij}$ and $\dot{u}^1_i$ can be expressed in the forms

$$\dot{\sigma}^1_{ij} = \hat{\sigma}^{kl}_{ij}(\boldsymbol{y})\frac{\partial \dot{u}^0_k}{\partial x_l}, \qquad \dot{u}^1_i = \chi(\boldsymbol{y})^{kl}_i \frac{\partial \dot{u}^0_k}{\partial x_l} \tag{22}$$

where

$$\frac{\partial \hat{\sigma}^{kl}_{ij}(\boldsymbol{y})}{\partial y_j} = 0 \quad \text{(microscopic equilibrium)} \tag{23}$$

In Eq. (22), $\hat{\sigma}^{kl}_{ij}$ is a $\boldsymbol{Y}$-antiperiodic function and χ^{kl}_i is a $\boldsymbol{Y}$-periodic function representing characteristic modes of the RME. Substituting Eqs. (22) and (21) in Eq. (13) yields the microscopic constitutive relations as

$$\hat{\sigma}^{kl}_{ij}(\boldsymbol{y}) = E^{\epsilon}_{ijpm}M^{kl}_{pm} \tag{24}$$

The local structure tensor is related to the $\boldsymbol{Y}$-periodic function χ^{kl}_i as

$$M^{kl}_{pm} = \left[T^{kl}_{pm} + \frac{\partial \chi^{kl}_p}{\partial y_m}\right] \tag{25}$$

where T^{kl}_{ij} is a fourth-order identity tensor expressed as

$$T^{kl}_{ij} = \frac{1}{2}(\delta_{ik}\delta_{jl} + \delta_{il}\delta_{jk}) \tag{26}$$

The set of equations (22) and (25) determine the vector $\chi(\boldsymbol{y})^{ij}_k$ to within an additive constant. The mean of Eq. (24) yields the homogenized elastic-plastic tangent modulus, for use in the macroscopic analysis, in the form

$$E^H_{ijkl} = \langle \hat{\sigma}^{kl}_{ij} \rangle = \frac{1}{|\boldsymbol{Y}|}\int_Y \hat{\sigma}^{kl}_{ij}\,\mathrm{d}Y = \frac{1}{|\boldsymbol{Y}|}\int_Y E^{\epsilon}_{ijpm}\left(T^{kl}_{pm} + \frac{\partial \chi^{kl}_p}{\partial y_m}\right)\mathrm{d}Y \tag{27}$$

2.2. Macroscopic equations

Taking the mean of the third equation in (14) on $\boldsymbol{Y}$ and applying the condition (16) to the first term $\partial\dot{\sigma}^2_{ij}/\partial y_j$ leads to an averaged form of the global equilibrium equation as

$$\frac{\partial\langle\dot{\sigma}^1_{ij}\rangle}{\partial x_j} + \dot{f}_i = 0 \quad \text{in } \Omega_{\text{structure}} \tag{28}$$

Note that the above equation (28) is now valid for the macroscopic domain $\Omega_{\text{structure}}$. Thus, in the macroscopic domain, the averaged stress rate $\dot{\boldsymbol{\Sigma}} = \langle\dot{\sigma}^1\rangle$ and displacement rate $\dot{\boldsymbol{u}}^0$ fields are the solutions to the elastic-plastic problem delineated by the equations:

$$\begin{aligned} &\frac{\partial\dot{\Sigma}_{ij}}{\partial x_j} = -\dot{f}_i \quad \text{in } \Omega_{\text{structure}} \\ &\dot{\Sigma}_{ij} = E^H_{ijkl}\dot{\bar{e}}_{kl} \\ &\dot{\Sigma}_{ij}n_j = \dot{t}_i \quad \text{on } \Gamma_t \\ &\dot{u}^0_i = \dot{\bar{u}}_i \quad \text{on } \Gamma_u \end{aligned} \tag{29}$$

An incremental small deformation analysis is pursued with Eq. (29) at the macroscopic level, and by using the Voronoi cell finite element model (VCFEM) for solving the microscopic problem. Developments of the incremental VCFEM model for heterogeneous microstructures are presented in the next section.

3. Microstructural analysis with VCFEM

Voronoi cells, resulting from Dirichlet tessellation of a heterogeneous microstructure, make rather unconventional elements, due to the arbitrariness in the number of edges. The Voronoi Cell finite element model developed by Ghosh and coworkers [26–29] avoids difficulties of conventional displacement based FEM formulations by invoking the assumed stress hybrid method introduced by Pian [33]. In this formulation, independent assumptions are made on an equilibriated stress field in the interior of each element and a compatible displacement field on the element boundary. Small deformation elastic-plastic analysis of materials with embedded second phase has shown significant promise with respect to efficiency and accuracy [26, 27]. Details of this development based on the hybrid formulation, originally proposed by Atluri and coworkers [34, 35], are presented in [26, 27]. In this section, a brief account of this formulation is presented for completeness.

3.1. Variational principles in VCFEM

Consider a typical representative material element (RME) Y tessellated into N Voronoi cells, as shown in Fig. 1(b). This is based on the location, shape and size of N heterogeneities as explained in [30]. The matrix phase in each Voronoi cell Y_e is denoted by Y_m and the heterogeneity (void or inclusion) is denoted by Y_c. The matrix-heterogeneity interface ∂Y_c has an outward normal $\boldsymbol{n}^c$, while $\boldsymbol{n}^e$ is the outward normal to the element boundary ∂Y_e. In this presentation, n incremental finite element formulation is invoked to account for rate independent plasticity. At the beginning of the pth increment, let $\boldsymbol{\sigma}$ be an equilibriated stress field with a strain field $\boldsymbol{e}(\boldsymbol{\sigma}$, load history), and $\boldsymbol{u}$ be a compatible displacement field on the element boundary. Also, let $\Delta\boldsymbol{\sigma}$ correspond to an equilibriated stress increment in Y_e, $\Delta\boldsymbol{u}$ to a compatible displacement increment on ∂Y_e, and $\Delta\bar{\boldsymbol{t}}$ to a traction increment on the traction boundary Γ_{tm}. The incremental problem is solved by using a two field assumed stress hybrid variational principle, derived from an element energy functional as

$$\begin{aligned}\Pi_e(\Delta\boldsymbol{\sigma},\Delta\boldsymbol{u}) = &-\int_{Y_e} \Delta B(\boldsymbol{\sigma},\Delta\boldsymbol{\sigma})\ \mathrm{d}Y - \int_{Y_e} \boldsymbol{e} : \Delta\boldsymbol{\sigma}\,\mathrm{d}Y \\ &+\int_{\partial Y_e} (\boldsymbol{\sigma}+\Delta\boldsymbol{\sigma})\cdot\boldsymbol{n}^e\cdot(\boldsymbol{u}+\Delta\boldsymbol{u})\ \partial Y - \int_{\Gamma_{tm}} (\bar{\boldsymbol{t}}+\Delta\bar{\boldsymbol{t}})\cdot(\boldsymbol{u}+\Delta\boldsymbol{u})\ \mathrm{d}\Gamma \\ &-\int_{\partial Y_c} (\boldsymbol{\sigma}^m+\Delta\boldsymbol{\sigma}^m-\boldsymbol{\sigma}^c-\Delta\boldsymbol{\sigma}^c)\cdot\boldsymbol{n}^c\cdot(\boldsymbol{u}'+\Delta\boldsymbol{u}')\ \partial Y \end{aligned} \tag{30}$$

where $\Delta\boldsymbol{u}'$ is the displacement of the interface and $\Delta\boldsymbol{B}$ is the increment in element complimentary energy. Superscripts m and c represent, respectively, the matrix and second phase parts of the Voronoi cell element. The energy functional for the entire domain is obtained by adding each element functional as

$$\Pi = \sum_{e=1}^{N} \Pi_e \tag{31}$$

The first variation of Π_e with respect to the stress increments $\Delta\boldsymbol{\sigma}$, results in the kinematic relations as the Euler equation,

$$\nabla\ \Delta\boldsymbol{u} = \Delta\boldsymbol{e} \quad \text{in } Y_e \tag{32}$$

while the first variation of Π with respect to boundary displacement increments $\Delta\boldsymbol{u}$ yields traction conditions as Euler equations,

$$\begin{aligned}
&(\boldsymbol{\sigma}+\Delta\boldsymbol{\sigma})\cdot\boldsymbol{n}^{e+} = -(\boldsymbol{\sigma}+\Delta\boldsymbol{\sigma})\cdot\boldsymbol{n}^{e-} && \text{on cell boundary } \Gamma_m \text{ (Interelement traction reciprocity)}\\
&(\boldsymbol{\sigma}+\Delta\boldsymbol{\sigma})\cdot\boldsymbol{n}^{e} = \bar{\boldsymbol{t}}+\Delta\bar{\boldsymbol{t}} && \text{on traction boundary } \Gamma_{tm}\\
&(\boldsymbol{\sigma}^c+\Delta\boldsymbol{\sigma}^c)\cdot\boldsymbol{n}^{c} = (\boldsymbol{\sigma}^m+\Delta\boldsymbol{\sigma}^m)\cdot\boldsymbol{n}^{c} && \text{on interface } \partial Y_c \text{ (Interface traction reciprocity)}
\end{aligned} \tag{33}$$

Equilibriated stress increments $\Delta\boldsymbol{\sigma}$, constitutive relations, along with the incremented form of the energy functional completely define the microstructural problem in the pth increment.

3.1.1. Element formulations and assumptions

In the Voronoi cell finite element model (VCFEM) formulation, independent assumptions on stress increments $\Delta\boldsymbol{\sigma}$ are made in the matrix and heterogeneity phases to accommodate stress jumps across the interface. Use of stress functions $\Phi(x,y)$ is a convenient way of deriving stress increments in two-dimensional analysis. Different expressions may be assumed for Φ in the matrix and inclusion phases. In general, these can be arbitrary functions of location, yielding stress increments in the form

$$\begin{aligned}
\{\Delta\boldsymbol{\sigma}^m\} &= [\boldsymbol{P}^m(x,y)]\{\Delta\boldsymbol{\beta}^m\}\\
\{\Delta\boldsymbol{\sigma}^c\} &= [\boldsymbol{P}^c(x,y)]\{\Delta\boldsymbol{\beta}^c\}
\end{aligned} \tag{34}$$

where $\{\Delta\boldsymbol{\beta}\}$s correspond to a set of yet undetermined stress coefficients and $[\boldsymbol{P}]$ is a matrix of interpolation functions. Compatible displacement increments on the element boundary ∂Y_e as well as on the interface ∂Y_c, are generated by interpolation in terms of generalized nodal values. The displacement increments on the element boundary and interface may then be written as

$$\begin{aligned}
\{\Delta\boldsymbol{u}\} &= [\boldsymbol{L}^e]\{\Delta\boldsymbol{q}\}\\
\{\Delta\boldsymbol{u}'\} &= [\boldsymbol{L}^c]\{\Delta\boldsymbol{q}'\}
\end{aligned} \tag{35}$$

where $\{\Delta\boldsymbol{q}\}$ and $\{\Delta\boldsymbol{q}'\}$ are generalized displacement increment vectors and $[\boldsymbol{L}]$ is an interpolation matrix. Substituting element approximations for stresses (34) and displacements (35), in the energy functional (30), and setting the first variations with respect to the stress coefficients $\Delta\boldsymbol{\beta}^m$ and $\Delta\boldsymbol{\beta}^c$, respectively, to zero, results in the following two weak forms of the kinematic relations (32),

$$\begin{aligned}
&\int_{Y_m}[\boldsymbol{P}^m]^{\mathrm{T}}\{\boldsymbol{e}+\Delta\boldsymbol{e}\}\,\mathrm{d}Y = \int_{\partial Y_e}[\boldsymbol{P}^m]^{\mathrm{T}}[\boldsymbol{n}^e][\boldsymbol{L}^e]\,\mathrm{d}Y\{\Delta\boldsymbol{q}\} - \int_{\partial Y_c}[\boldsymbol{P}^m]^{\mathrm{T}}[\boldsymbol{n}^c][\boldsymbol{L}^c]\,\mathrm{d}Y\{\Delta\boldsymbol{q}'\}\\
&\int_{Y_c}[\boldsymbol{P}^c]^{\mathrm{T}}\{\boldsymbol{e}+\Delta\boldsymbol{e}\}\,\mathrm{d}Y = \int_{\partial Y_c}[\boldsymbol{P}^c]^{\mathrm{T}}[\boldsymbol{n}^c][\boldsymbol{L}^c]\,\mathrm{d}Y\{\Delta\boldsymbol{q}'\}
\end{aligned} \tag{36}$$

Setting the first variation of the total energy functional (31) with respect to $\Delta\boldsymbol{q}$ and $\Delta\boldsymbol{q}'$ to zero, results in the weak form of the traction reciprocity conditions as

$$\begin{aligned}
&\sum_{e=1}^{N}\begin{bmatrix} \int_{\partial Y_e}[\boldsymbol{L}^e]^{\mathrm{T}}[\boldsymbol{n}^e]^{\mathrm{T}}[\boldsymbol{P}^m]\,\mathrm{d}Y & \boldsymbol{0}\\ -\int_{\partial Y_c}[\boldsymbol{L}^c]^{\mathrm{T}}[\boldsymbol{n}^c]^{\mathrm{T}}[\boldsymbol{P}^m]\,\mathrm{d}Y & \int_{\partial Y_c}[\boldsymbol{L}^c]^{\mathrm{T}}[\boldsymbol{n}^c]^{\mathrm{T}}[\boldsymbol{P}^c]\,\mathrm{d}Y \end{bmatrix}\begin{Bmatrix}\boldsymbol{\beta}^m+\Delta\boldsymbol{\beta}^m\\ \boldsymbol{\beta}^c+\Delta\boldsymbol{\beta}^c\end{Bmatrix}\\
&\quad=\sum_{e=1}^{N}\begin{Bmatrix}\int_{\Gamma_{tm}}[\boldsymbol{L}^e]^{\mathrm{T}}\{\bar{\boldsymbol{t}}+\Delta\bar{\boldsymbol{t}}\}\,\mathrm{d}Y\\ \{\boldsymbol{0}\}\end{Bmatrix}
\end{aligned} \tag{37}$$

For an elastic-plastic material, the strain increments $\Delta\boldsymbol{e}$ in Eq. (36) are non-linear functions of the current state of stress $\boldsymbol{\sigma}$ as well as of their increments $\Delta\boldsymbol{\sigma}$. The non-linear finite element equations (36) and

(37) are solved for the stress parameters ($\Delta\boldsymbol{\beta}^m$, $\Delta\boldsymbol{\beta}^c$) and the nodal displacement increments ($\Delta\boldsymbol{q}$, $\Delta\boldsymbol{q}'$) at the pth increment.

3.1.2. Shape based stress representations

An important criterion, affecting the convergence of multiple phase Voronoi cell elements, is the proper choice of stress fields in each of the constituent phases. Choosing stress functions from micromechanics considerations, adds considerably to the element efficiency. Three different conditions that are indispensable in this regard are:

(1) Stress functions should, in some way, account for the shape of the heterogeneity.
(2) Effects of the heterogeneity shape should vanish at large distances from the interface for matrix stress functions.
(3) Shape effects in matrix stress functions should facilitate traction reciprocity at the interface.

For heterogeneous materials, the first two considerations imply that the shape effect should be dominant near the interface, but vanish in the far-field. The third condition is intended to counteract interface tractions caused by the inclusion for composites, while reduce to zero interface tractions for porous materials. Pure polynomial forms Airy's stress functions do not explicitly account for the shape of the heterogeneity and requires very high order terms for convergence. This problem of stress concentrations around voids has been solved by Tong et al. [36] and Piltner [37] for elastic problems with cracks and holes. They have used complex functions and conformal mapping techniques to construct trial stress functions. A similar approach is pursued in VCFEM to deal with arbitrary shaped interfaces for nonlinear materials. Suppose that equation of the interface ∂Y_c in Fig. 1(c) can be expressed in polar coordinates as $g(r, \theta) = 0$, where the r coordinate is measured from the centroid of the heterogeneity. A Fourier series expansion for r in terms of the polar angle θ may be expressed as:

$$r = a_o + \sum_n a_n \cos(n\theta) + \sum_n b_n \sin(n\theta) \quad \text{on } \partial Y_c \tag{38}$$

where a_n and b_n are the Fourier coefficients. The interface equation may then be expressed from (38) as

$$g(r, \theta) = f - \frac{r}{a_0} - \sum_n \frac{a_n}{a_0} \cos(n\theta) - \sum_n \frac{b_n}{a_0} \sin(n\theta) = 0 \tag{39}$$

Here, f corresponds to a function that transforms any arbitrary shaped interface to an approximate unit circle, since $f(x, y) = 1$ on ∂Y_c. The mapped function $f(r, \theta)$ may be thought of as a special radial coordinate with the property that $1/f \to 0$ as $(x, y) \to \infty$. This function is now used to construct stress functions in the matrix region Y_m from the two part expression

$$\Phi^m = \Phi^m_{\text{poly}} + \Phi^m_{\text{rec}} \tag{40}$$

with Φ^m_{poly} expressed in terms of a polynomial expansion of coordinates, i.e. $\Phi^m_{\text{poly}} = \sum_{p,q} \beta_{pq} x^p y^q$. For each polynomial term in Φ^m_{poly} there exist shape based reciprocal terms Φ^m_{rec}, that give rise to stresses equilibriating the traction field on ∂Y_c. This is written as

$$\Phi^m_{\text{rec}} = \sum_{p,q} \xi^p \eta^q \left(\frac{\Delta\beta_{pq1}}{f^{p+q}} + \frac{\Delta\beta_{pq2}}{f^{p+q+1}} + \cdots \right) = \sum_{p,q,i} x^p y^q \frac{\Delta\beta_{pqi}}{f^{p+q+i-1}}$$

The inclusion is modeled using polynomial stress functions only. The matrix phase stress increments in two dimensions are obtained from the conventional stress function-stress relations to yield:

$$\begin{Bmatrix} \Delta\sigma^m_{xx} \\ \Delta\sigma^m_{yy} \\ \Delta\sigma^m_{xy} \end{Bmatrix} = \begin{Bmatrix} \sum\limits_{p,q} \dfrac{\partial^2(x^p y^q)}{\partial y^2}\Delta\beta_{pq} + \sum\limits_{p,q,i} \dfrac{\partial^2(x^p y^q/f^i)}{\partial y^2}\Delta\beta_{pqi} \\ \sum\limits_{p,q} \dfrac{\partial^2(x^p y^q)}{\partial x^2}\Delta\beta_{pq} + \sum\limits_{p,q,i} \dfrac{\partial^2(x^p y^q/f^i)}{\partial x^2}\Delta\beta_{pqi} \\ -\sum\limits_{p,q} \dfrac{\partial^2(x^p y^q)}{\partial x\partial y}\Delta\beta_{pq} - \sum\limits_{p,q,i} \dfrac{\partial^2(x^p y^q/f^i)}{\partial x\partial y}\Delta\beta_{pqi} \end{Bmatrix}$$
$$= [\boldsymbol{P}_{\text{poly}}]\begin{Bmatrix} \Delta\beta_{11} \\ \vdots \\ \Delta\beta_{pq} \\ \vdots \end{Bmatrix} + [\boldsymbol{P}_{\text{rec}}]\begin{Bmatrix} \Delta\beta_{111} \\ \vdots \\ \Delta\beta_{pqi} \\ \vdots \end{Bmatrix}$$
$$= [\boldsymbol{P}^m]\{\Delta\boldsymbol{\beta}^m\} \tag{41}$$

A detailed treatment of stress function selection and convergence issues are presented in [27].

3.2. *Constitutive relations*

A rate independent small deformation elastio-plastic constitutive relation, following J_2 flow theory with isotropic hardening is considered in this paper. A brief account of the numerical integration of the constitutive relations is presented here. More details are provided in [26, 27]. An additive decomposition of the strain increments $\Delta\boldsymbol{e}$ into an elastic part $\Delta\boldsymbol{e}^{\text{e}}$ and a plastic part $\Delta\boldsymbol{e}^{\text{pl}}$ is assumed, i.e.

$$\Delta\boldsymbol{e} = \Delta\boldsymbol{e}^{\text{e}} + \Delta\boldsymbol{e}^{\text{pl}} \tag{42}$$

The yield surface in stress–space at the beginning of the pth increment is expressed as

$$Y^p(\boldsymbol{e}, \Delta\boldsymbol{e}) = \sqrt{\frac{3}{2}\boldsymbol{\sigma}' : \boldsymbol{\sigma}'} \tag{43}$$

where $\boldsymbol{\sigma}'$ is the deviatoric stress and $Y(\boldsymbol{e}, \Delta\boldsymbol{e})$ is the radius of the flow surface. The plastic strain increment $\Delta\boldsymbol{e}^{\text{pl}}$ is obtained by numerically integrating the flow rule by the backward Euler method to yield:

$$\Delta\boldsymbol{e}^{\text{pl}} = \Delta\lambda(\boldsymbol{\sigma} + \Delta\boldsymbol{\sigma})' \tag{44}$$

where $\Delta\lambda$ is a non-negative incremental flow parameter. Since $\Delta\boldsymbol{e}$ is in general a function of $\Delta\lambda$, $\boldsymbol{\sigma}$ and $\Delta\boldsymbol{\sigma}$, the flow surface radius can be expressed in the form,

$$Y^{p+1} = Y^{p+1}(\Delta\lambda, \boldsymbol{\sigma}, \Delta\boldsymbol{\sigma})$$

and the flow parameter $\Delta\lambda$ can be evaluated from the following relations.

$$\Delta\lambda = 0 \quad \text{if } \sigma^{p+1}_{\text{eff}} < Y^p \quad \text{(elastic unloading)} \tag{45}$$

$$\sigma^{p+1}_{\text{eff}} = Y^{p+1} \quad \text{if } \sigma^{p+1}_{\text{eff}} \geqslant Y^p \quad \text{(neutral and plastic loading)} \tag{46}$$

Numerical implementation requires computation of tangent operators through linearized forms of the constitutive relations. If $\mathrm{d}\boldsymbol{e}$ is the first-order correction to the current strain increment $\Delta\boldsymbol{e}$, and $\mathrm{d}\boldsymbol{\sigma}$ is the corresponding stress increment $\Delta\boldsymbol{\sigma}$ correction, the fourth-order elastic-plastic compliance tensor (or tangent operator) $\boldsymbol{S}$ is given by the relation

$$\mathrm{d}\boldsymbol{e} = \boldsymbol{S} : \mathrm{d}\boldsymbol{\sigma}$$

The elastic part of this equation expressed as

$$\mathrm{d}\boldsymbol{e}^{\text{e}} = \boldsymbol{S}_e : \mathrm{d}\boldsymbol{\sigma} \tag{47}$$

The plastic part of the strain correction $\mathrm{d}\boldsymbol{e}^{\mathrm{pl}}$ however requires a first-order correction $\mathrm{d}\lambda$ to the current flow parameter $\Delta\lambda$, which by the J_2 flow theory, takes the form

$$\mathrm{d}\boldsymbol{e}^{\mathrm{pl}} = \frac{9}{4H} \frac{(\boldsymbol{\sigma} + \Delta\boldsymbol{\sigma})' \otimes (\boldsymbol{\sigma} + \Delta\boldsymbol{\sigma})'}{(\sigma_{\mathrm{eff}}^{p+1})^2} : \mathrm{d}\boldsymbol{\sigma} = \boldsymbol{S}_{\mathrm{pl}} : \mathrm{d}\boldsymbol{\sigma} \tag{48}$$

where H is a linearized hardening modulus. The elasto-plastic tangent operator $\boldsymbol{S}$ is obtained by adding Eqs. (47) and (48) as

$$\boldsymbol{S} = \boldsymbol{S}_{\mathrm{e}} + \boldsymbol{S}_{\mathrm{pl}} \tag{49}$$

A linearized form of the incremental complementary energy functional ΔB in Eq. (30) can now be expressed in terms of the tangent operator as

$$\mathrm{d}B(\boldsymbol{\sigma}, \mathrm{d}\boldsymbol{\sigma}) = \frac{1}{2} \mathrm{d}\boldsymbol{\sigma} : \boldsymbol{S} : \mathrm{d}\boldsymbol{\sigma} \tag{50}$$

Note that the elastic-plastic tangent operator $\boldsymbol{S}$ in Eq. (49) is positive definite since its components are individually positive definite.

3.3. Solution method

For rate independent plasticity, the strain increments $\Delta\boldsymbol{e}(\Delta\boldsymbol{\sigma}, \boldsymbol{\sigma})$ are non-linear functions of the stress parameters $\Delta\boldsymbol{\beta}^m$ and $\Delta\boldsymbol{\beta}^c$. An iterative solution process is invoked to evaluate the stresses, given the nodal displacement increments $\{\Delta\boldsymbol{q}\}$ and $\{\Delta\boldsymbol{q}'\}$ in Eq. (35). Let $\{\mathrm{d}\boldsymbol{\beta}\}^i$ correspond to the correction to the value of $\Delta\boldsymbol{\beta}$ in the ith iteration, i.e.

$$\{\Delta\boldsymbol{\beta}^m\} = \{\Delta\boldsymbol{\beta}^m\}^i + \{\mathrm{d}\boldsymbol{\beta}^m\}^i$$
$$\{\Delta\boldsymbol{\beta}^c\} = \{\Delta\boldsymbol{\beta}^c\}^i + \{\mathrm{d}\boldsymbol{\beta}^c\}^i$$

The kinematic equation (36) may then be linearized with respect to $\Delta\boldsymbol{\beta}$ to yield:

$$\begin{bmatrix} \boldsymbol{H}_m & \boldsymbol{0} \\ \boldsymbol{0} & \boldsymbol{H}_c \end{bmatrix} \begin{Bmatrix} \mathrm{d}\boldsymbol{\beta}^m \\ \mathrm{d}\boldsymbol{\beta}^c \end{Bmatrix}^i = \begin{bmatrix} \boldsymbol{G}_e & -\boldsymbol{G}_{cm} \\ \boldsymbol{0} & \boldsymbol{G}_{cc} \end{bmatrix} \begin{Bmatrix} \boldsymbol{q} + \Delta\boldsymbol{q} \\ \boldsymbol{q}' + \Delta\boldsymbol{q}' \end{Bmatrix} - \begin{Bmatrix} \int_{Y_m} [\boldsymbol{P}^m]^{\mathrm{T}} \{\boldsymbol{e} + \Delta\boldsymbol{e}\}^i \, \mathrm{d}Y \\ \int_{Y_c} [\boldsymbol{P}^c]^{\mathrm{T}} \{\boldsymbol{e} + \Delta\boldsymbol{e}\}^i \, \mathrm{d}Y \end{Bmatrix} \tag{51}$$

or in a condensed form as

$$[\boldsymbol{H}]\{\mathrm{d}\boldsymbol{\beta}\}^i = [\boldsymbol{G}]\{\boldsymbol{q}\} - \left\{ \int_Y [\boldsymbol{P}]^{\mathrm{T}} \{\boldsymbol{e} + \Delta\boldsymbol{e}\}^i \, \mathrm{d}Y \right\} \tag{52}$$

where

$$[\boldsymbol{H}_m] = \int_{Y_m} [\boldsymbol{P}^m]^{\mathrm{T}} [\boldsymbol{S}] [\boldsymbol{P}^m] \, \mathrm{d}Y \,, \qquad [\boldsymbol{H}_c] = \int_{Y_c} [\boldsymbol{P}^c]^{\mathrm{T}} [\boldsymbol{S}] [\boldsymbol{P}^c] \, \mathrm{d}Y$$
$$[\boldsymbol{G}_e] = \int_{\partial Y_e} [\boldsymbol{P}^m]^{\mathrm{T}} [\boldsymbol{n}^e] [\boldsymbol{L}^e] \, \mathrm{d}Y \,, \qquad [\boldsymbol{G}_{cm}] = \int_{\partial Y_c} [\boldsymbol{P}^m]^{\mathrm{T}} [\boldsymbol{n}^c] [\boldsymbol{L}^c] \, \mathrm{d}Y \,, \qquad [\boldsymbol{G}_{cc}] = \int_{\partial Y_c} [\boldsymbol{P}^c]^{\mathrm{T}} [\boldsymbol{n}^c] [\boldsymbol{L}^c] \, \mathrm{d}Y$$

$[\boldsymbol{S}(x, y)]$ is the instantaneous elastic-plastic tangent compliance tensor as derived in Eq. (49) and $[\boldsymbol{n}]$ is a matrix consisting of the components of the normal. A quasi-Newton iterative solution procedure is used to solve Eq. (51).

The above procedure of solving for the stresses takes place within an iterative loop, in which the traction reciprocity conditions (37) are solved for the nodal displacement increments $\{\Delta\boldsymbol{q}\}$ and $\{\Delta\boldsymbol{q}'\}$.

Proceeding in the same way as for stresses, let $\{\mathrm{d}\boldsymbol{q}\}^j$ correspond to the correction in $\{\Delta\boldsymbol{q}\}$ in the jth iteration of (37), i.e.

$$\{\Delta\boldsymbol{q}\} = \{\Delta\boldsymbol{q}\}^j + \{\mathrm{d}\boldsymbol{q}\}^j$$

$$\{\Delta\boldsymbol{q}'\} = \{\Delta\boldsymbol{q}'\}^j + \{\mathrm{d}\boldsymbol{q}'\}^j$$

Substituting Eq. (51) in the linearized global traction reciprocity equation (37), with respect to $\{\Delta\boldsymbol{q}\}$, yields the matrix equation:

$$\begin{aligned}\sum_{e=1}^{N}[\boldsymbol{G}]^{\mathrm{T}}[\boldsymbol{H}]^{-1}[\boldsymbol{G}]\left\{\begin{array}{c}\mathrm{d}\boldsymbol{q}\\ \mathrm{d}\boldsymbol{q}'\end{array}\right\}^{j} &= \sum_{e=1}^{N}\left\{\begin{array}{c}\displaystyle\int_{\Gamma_{tm}}[\boldsymbol{L}^m]^{\mathrm{T}}\{\bar{\boldsymbol{t}}+\bar{\Delta\boldsymbol{t}}\}\,\mathrm{d}Y\\ \boldsymbol{0}\end{array}\right\}\\ &-\sum_{e=1}^{N}\left[\begin{array}{cc}\displaystyle\int_{\partial Y_e}[\boldsymbol{L}^e]^{\mathrm{T}}[\boldsymbol{n}^e]^{\mathrm{T}}[\boldsymbol{P}^m]\,\mathrm{d}Y & \boldsymbol{0}\\ \displaystyle-\int_{\partial Y_c}[\boldsymbol{L}^c]^{\mathrm{T}}[\boldsymbol{n}^c]^{\mathrm{T}}[\boldsymbol{P}^m]\,\mathrm{d}Y & \displaystyle\int_{\partial Y_c}[\boldsymbol{L}^c]^{\mathrm{T}}[\boldsymbol{n}^c]^{\mathrm{T}}[\boldsymbol{P}^c]\,\mathrm{d}Y\end{array}\right]\left\{\begin{array}{c}\boldsymbol{\beta}^m+\Delta\boldsymbol{\beta}^m\\ \boldsymbol{\beta}^c+\Delta\boldsymbol{\beta}^c\end{array}\right\}^{j}\end{aligned} \tag{53}$$

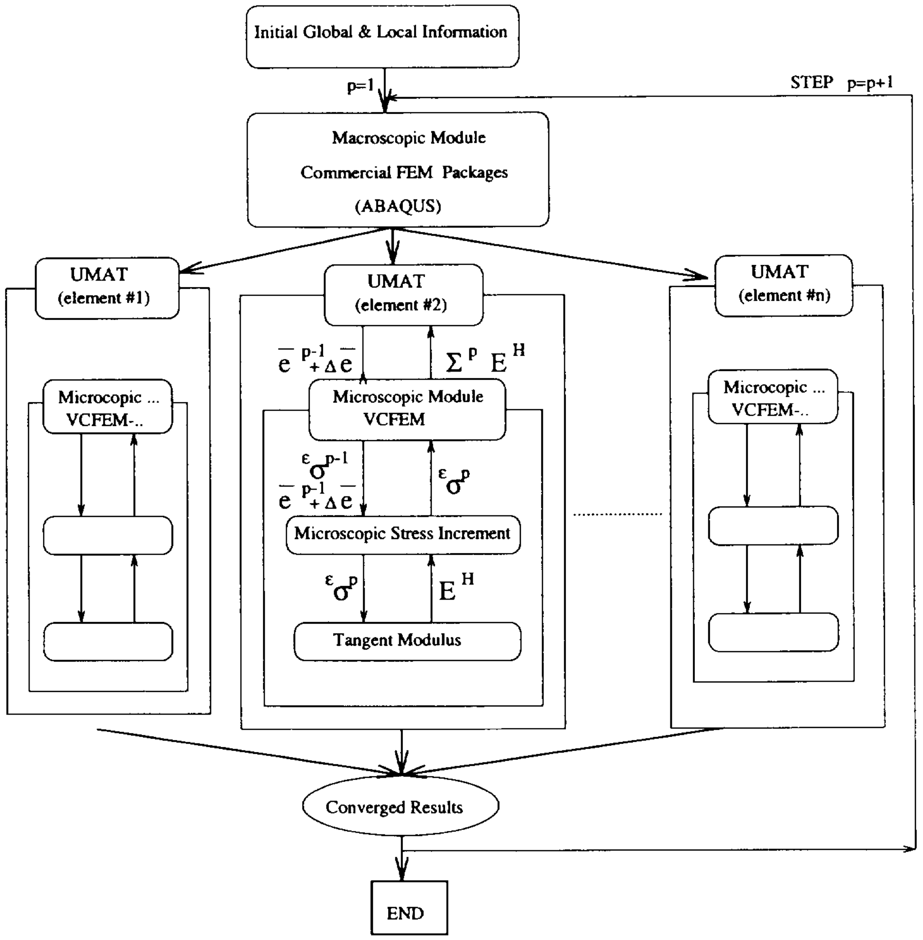
Initial Global & Local Information
p=1
STEP p=p+1
Macroscopic Module
Commercial FEM Packages
(ABAQUS)
UMAT
(element #1)
UMAT
(element #2)
UMAT
(element #n)
Microcopic ...
VCFEM-..
$\bar{e}^{p-1}+\Delta\bar{e}$
Σ^{p} E^{H}
Microscopic Module
VCFEM
ϵ^{p-1} σ^{p-1}
$\bar{e}^{p-1}+\Delta\bar{e}$
ϵ^{p} σ^{p}
Microscopic Stress Increment
ϵ^{p} σ^{p}
E^{H}
Tangent Modulus
Microcopic ...
VCFEM-..
Converged Results
END

Fig. 2. Flow chart of two scale analysis.

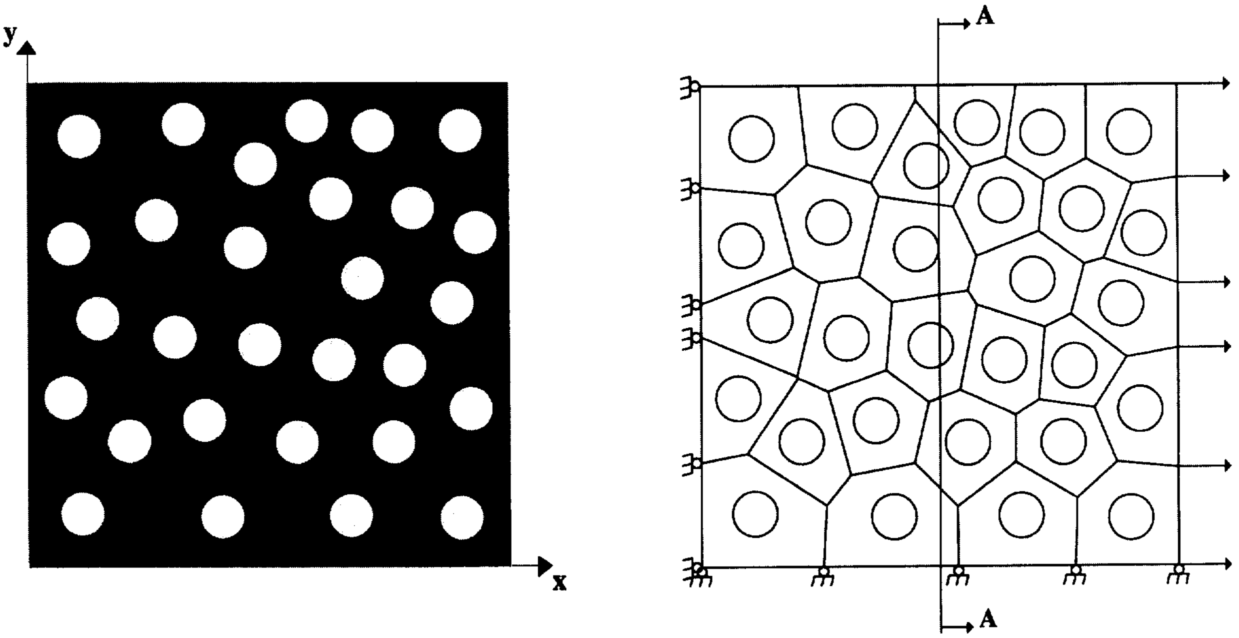

(a) (b)

Fig. 3. (a) ANSYS and (b) VCFEM meshes for randomly packed RME with circular voids ($V_f = 20\%$).

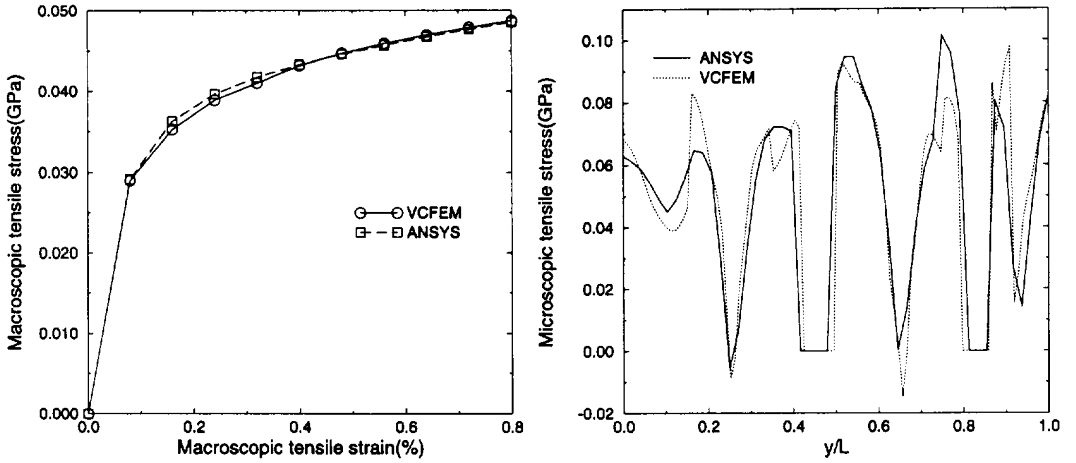

(a) (b)

Fig. 4. (a) Macroscopic stress–strain response; (b) microscopic stress distribution at 0.8% strain for random packed RME along $x/L = 0.5$.

With known traction increments on Γ_{tm} and displacement increments on Γ_{um}, the linearized global traction reciprocity condition (53) is solved iteratively using the quasi-Newton method for nodal displacement increments.

3.4. A numerical test example

The effectiveness of the elastic-plastic Voronoi cell finite element model in analyzing heterogeneous microstructures is established by several numerical examples in [26, 27]. In this section, a representative example is presented to illustrate its competence. The representative material element (RME) analyzed,

consists of 29 randomly located circular voids with volume fraction $V_f = 20\%$. Results generated by VCFEM are compared with those of a displacement based commercial finite element code ANSYS with a very high resolution mesh, necessary for convergence. Figs. 3(b) and (a) show the VCFEM mesh with 29 elements and the ANSYS mesh with 5282 QUAD4 elements, respectively. Plane strain uniaxial tension loading is considered to a maximum of 0.8% macroscopic strain. Periodic construct of the RME is achieved through repeatability conditions on the traction free face. The matrix material is Aluminum with the following properties:
$E = 69$ GPa (Young's Modulus), $\nu = 0.33$ (Poisson's Ratio)
$Y_0 = 43$ MPa (Initial Yield Stress), $\sigma_{\mathrm{eqv}} = Y_0 + e_{\mathrm{eqv}}^{0.125}$ (Post Yield Hardening Law)

The VCFEM analysis uses a 48 term stress function (p+q = 2...4 and i = 1...3) in the matrix in Eq. (41). Comparison of macroscopic response in Fig. 4(a) clearly establishes VCFEM as an accurate method for modeling overall behavior of random microstructures at a significant advantage in computing efficiency. The microscopic stress distribution through the section A-A in Fig. 3(b) at 0.8% strain is depicted in Fig. 4(b). Once again the comparison is very satisfactory, with VCFEM producing similar patterns and peak stresses with the highly refined ANSYS model.

4. Elastic-plastic homogenization with VCFEM

In this section, the Voronoi Cell finite element model is formulated to be applied in conjunction with the homogenization method for coupling global and local analyses. VCFEM is used to model an arbitrary microstructural RME, and consequently, $\boldsymbol{Y}$ represents a RME with a boundary $\partial \boldsymbol{Y}$. In an incremental formulation, the equilibriated microscopic stress increment corresponds to $\Delta\boldsymbol{\sigma}^1 (= \Delta\boldsymbol{\sigma}^\epsilon)$ in Eq. (22) and the microstructural strain increments are designated as $\Delta\boldsymbol{e}^\epsilon$ in Eq. (20). Similarly, the increments in microscopic displacements on the cell boundaries ∂Y_e are identified with $\Delta\boldsymbol{u}^1$ in Eq. (22) and those on the interface are denoted by $\Delta\boldsymbol{u}^{1'}$. In the absence of traction boundaries due to periodicity conditions, the incremental energy functional for each Voronoi cell element in Eq. (30) is modified for the homogenization process as:

$$\begin{aligned}\Pi_e = &-\int_{Y_e} \frac{1}{2} S^\epsilon_{ijkl}\, \Delta\sigma^\epsilon_{ij}\, \Delta\sigma^\epsilon_{kl}\, \mathrm{d}Y - \int_{Y_e} e^\epsilon_{ij}\, \Delta\sigma^\epsilon_{ij}\, \mathrm{d}Y + \int_{\partial Y_e} (\sigma^\epsilon_{ij} + \Delta\sigma^\epsilon_{ij})\, (u^1_i + \Delta u^1_i)\, n^e_j\, \mathrm{d}\partial Y \\ &- \int_{\partial Y_c} (\sigma^{\epsilon m}_{ij} + \Delta\sigma^{\epsilon m}_{ij} - \sigma^{\epsilon c}_{ij} - \Delta\sigma^{\epsilon c}_{ij})\, (u^{1'}_i + \Delta u^{1'}_i)\, n^c_j\, \mathrm{d}\partial Y + \int_{Y_e} (\bar{e}_{ij} + \Delta\bar{e}_{ij}) \Delta\sigma^\epsilon_{ij}\, \mathrm{d}Y \end{aligned} \tag{54}$$

where S^ϵ_{ijkl} is an instantaneous elatic-plastic compliance tensor. The last term in Eq. (54) incorporates the effect of macroscopic strains in the microstructure. The stationary condition of Π_e with respect to stress increment $\Delta\sigma^\epsilon_{ij}$ yields, as Euler's equations, the incremental form of kinematic relations (20)

$$e^\epsilon_{ij} + \Delta e^\epsilon_{ij} = \bar{e}_{ij} + \Delta\bar{e}_{ij} + \frac{\partial(u^1_i + \Delta u^1_i)}{\partial y_j} \tag{55}$$

Furthermore, stationarity of the total energy functional $\Pi = \sum_{e=1}^{N} \Pi_e$ with respect to displacement increments Δu^1_i and $u^{1'}_i$, respectively, result in the inter-element and interface traction reciprocity conditions:

$$(\sigma^\epsilon_{ij} + \Delta\sigma^\epsilon_{ij}) \cdot n^{e+}_j = -(\sigma^\epsilon_{ij} + \Delta\sigma^\epsilon_{ij}) \cdot n^{e-}_j \quad \text{on } \partial Y_e \tag{56}$$

$$(\sigma^{\epsilon c}_{ij} + \Delta\sigma^{\epsilon c}_{ij}) \cdot n^c_j = (\sigma^{\epsilon m}_{ij} + \Delta\sigma^{\epsilon m}_{ij}) \cdot n^c_j \quad \text{on } \partial Y_c \tag{57}$$

where superscript + and − denote values on opposite sides of the inter element boundary ∂Y_e. The three Euler's equations together with (a) the assumed equilibriated stress fields satisfying $\Delta\sigma^\epsilon_{ij,j} = 0$ in Y_e, (b) assumed compatible displacement increment fields in ∂Y_e and ∂Y_c, and the instantaneous constitutive relation $\Delta e^\epsilon_{ij} = S^\epsilon_{ijkl}\, \Delta\sigma^\epsilon_{kl}$ describe the incremental boundary value problem for the microstructure.

The microscopic VCFEM module is executed for two purposes in each increment of the macroscopic module. The first is to evaluate the microscopic stress increments $\Delta\boldsymbol{\sigma}^\epsilon$ from given values of the macroscopic strain $\bar{e}$ at the beginning of the step, and its increment $\Delta\bar{e}$. The second is to calculate the instantaneous homogenized tangent modulus E^H_{ijkl} at the end of the increment in the macroscopic module.

4.1. Calculation of microscopic stresses

This step involves the iterative solution of modified forms of the kinematic relations (36) and the traction reciprocity conditions (37) to yield the incremental stress parameters $\Delta\boldsymbol{\beta}$ and the nodal displacement increments $\Delta\boldsymbol{q}$ and $\Delta\boldsymbol{q}'$. The weak form of the element kinematic relation (55) is obtained by modifying (36) for homogenization in the multiple scale model as

$$\begin{aligned}\int_{Y_e - Y_c} [\boldsymbol{P}^m]^{\mathrm{T}}\{\boldsymbol{e}^\epsilon + \Delta\boldsymbol{e}^\epsilon - \bar{\boldsymbol{e}} - \Delta\bar{\boldsymbol{e}}\}\,\mathrm{d}Y &= \int_{\partial Y_e} [\boldsymbol{P}^m]^{\mathrm{T}}[\boldsymbol{n}^e][\boldsymbol{L}^e]\,\mathrm{d}Y\ \{\boldsymbol{q} + \Delta\boldsymbol{q}\}_e \\ &\quad - \int_{\partial Y_c} [\boldsymbol{P}^m]^{\mathrm{T}}[\boldsymbol{n}^c][\boldsymbol{L}^c]\,\mathrm{d}Y\ \{\boldsymbol{q}' + \Delta\boldsymbol{q}'\}_e\end{aligned} \tag{58}$$

$$\int_{Y_c} [\boldsymbol{P}^c]^{\mathrm{T}}\{\boldsymbol{e}^\epsilon + \Delta\boldsymbol{e}^\epsilon - \bar{\boldsymbol{e}} - \Delta\bar{\boldsymbol{e}}\}\,\mathrm{d}Y = \int_{\partial Y_c} [\boldsymbol{P}^c]^{\mathrm{T}}[\boldsymbol{n}^c][\boldsymbol{L}^e]\,\mathrm{d}Y\ \{\boldsymbol{q}' + \Delta\boldsymbol{q}'\}_e \tag{59}$$

As mentioned in Section 3.2, an iterative solution process is implemented for evaluating stresses from given values of the nodal displacements. In the ith iteration, the total strain increment $\{\Delta\boldsymbol{e}^\epsilon\}$ is linearized with respect to stress increment $\{\Delta\boldsymbol{\sigma}^\epsilon\}$ in the form:

$$\{\Delta\boldsymbol{e}^\epsilon\} = \{\Delta\boldsymbol{e}^\epsilon(\boldsymbol{\sigma}^\epsilon, \Delta\boldsymbol{\sigma}^\epsilon)\}^i + [\boldsymbol{S}^\epsilon] : \{\mathrm{d}\boldsymbol{\sigma}^\epsilon\}^i \tag{60}$$

where the correction $\{\mathrm{d}\boldsymbol{\sigma}^\epsilon\}^i$ to stress increment is expressed as,

$$\{\mathrm{d}\boldsymbol{\sigma}^\epsilon\}^i = [\boldsymbol{P}]\{\mathrm{d}\boldsymbol{\beta}\}^i \quad \text{in } Y_e \tag{61}$$

Substitution in (58) and (59) leads to the linearized kinematic equations (51) in conjunction with the homogenization procedure as

$$\begin{bmatrix} \boldsymbol{H}_m & 0 \\ 0 & \boldsymbol{H}_c \end{bmatrix} \begin{Bmatrix} \mathrm{d}\boldsymbol{\beta}^m \\ \mathrm{d}\boldsymbol{\beta}^c \end{Bmatrix}^i = \begin{bmatrix} \boldsymbol{G}_e & -\boldsymbol{G}_{cm} \\ 0 & \boldsymbol{G}_{cc} \end{bmatrix} \begin{Bmatrix} \boldsymbol{q} + \Delta\boldsymbol{q} \\ \boldsymbol{q}' + \Delta\boldsymbol{q}' \end{Bmatrix} - \begin{Bmatrix} \displaystyle\int_{Y_e - Y_c} [\boldsymbol{P}^m]^{\mathrm{T}}\{\boldsymbol{e}^\epsilon + \Delta\boldsymbol{e}^{\epsilon i} - \bar{\boldsymbol{e}} - \Delta\bar{\boldsymbol{e}}\}\,\mathrm{d}Y \\ \displaystyle\int_{Y_c} [\boldsymbol{P}^c]^{\mathrm{T}}\{\boldsymbol{e}^\epsilon + \Delta\boldsymbol{e}^{\epsilon i} - \bar{\boldsymbol{e}} - \Delta\bar{\boldsymbol{e}}\}\mathrm{d}Y \end{Bmatrix} \tag{62}$$

where components of the matrices are explained in Eq. (51). The traction reciprocity equations (53) are iteratively solved for nodal displacements in the same way as mentioned in Section 3.3. In the jth iteration, this corresponds to the solution of the linearized global traction reciprocity equation:

$$\begin{aligned}&\sum_{e=1}^{N} [\boldsymbol{G}]^{\mathrm{T}}[\boldsymbol{H}]^{-1}[\boldsymbol{G}] \begin{Bmatrix} \mathrm{d}\boldsymbol{q} \\ \mathrm{d}\boldsymbol{q}' \end{Bmatrix}^j \\ &\quad = -\sum_{e=1}^{N} \begin{bmatrix} \displaystyle\int_{\partial Y_e} [\boldsymbol{L}^e]^{\mathrm{T}}[\boldsymbol{n}^e]^{\mathrm{T}}[\boldsymbol{P}^m]^{\mathrm{T}}\,\mathrm{d}Y & 0 \\ \displaystyle -\int_{\partial Y_c} [\boldsymbol{L}^c]^{\mathrm{T}}[\boldsymbol{n}^c]^{\mathrm{T}}[\boldsymbol{P}^m]^{\mathrm{T}}\,\mathrm{d}Y & \displaystyle\int_{\partial Y_c} [\boldsymbol{L}^c]^{\mathrm{T}}[\boldsymbol{n}^c][\boldsymbol{P}^c]^{\mathrm{T}}\,\mathrm{d}Y \end{bmatrix} \begin{Bmatrix} \boldsymbol{\beta}^m + \Delta\boldsymbol{\beta}^m \\ \boldsymbol{\beta}^c + \Delta\boldsymbol{\beta}^c \end{Bmatrix}^j\end{aligned} \tag{63}$$

4.2. Calculation of homogenized tangent modulus

Evaluation of the homogenized tangent modulus tensor E^H_{ijkl} is performed at the end of an increment in the global analysis (ABAQUS) after converged values of microscopic variables have been obtained.

From the basic definition in Eq. (27), components of E^H_{ijkl} are obtained by averaging the true stress increments in response to unit increments in components of the strain tensor $\bar{\boldsymbol{e}}$. In two-dimensional analysis the individual components correspond to $\bar{\boldsymbol{e}}_{11}, \bar{\boldsymbol{e}}_{22}$ and $\bar{\boldsymbol{e}}_{12}$, or in contracted notations $\bar{\boldsymbol{e}}_1, \bar{\boldsymbol{e}}_2$ and $\bar{\boldsymbol{e}}_3$, i.e. $\bar{\boldsymbol{e}}_i$, $i = 1, 2, 3$. This is obtained first by consistent linearization of the element kinematic relation in Eq. (51) with respect to each component of the macroscopic strain increment $\bar{\boldsymbol{e}}_i$ to yield:

$$\begin{bmatrix} \boldsymbol{H}_m & \mathbf{0} \\ \mathbf{0} & \boldsymbol{H}_c \end{bmatrix} \begin{Bmatrix} \delta\boldsymbol{\beta}^m \\ \delta\boldsymbol{\beta}^c \end{Bmatrix}_i = \begin{bmatrix} \boldsymbol{G}_e & -\boldsymbol{G}_{cm} \\ \mathbf{0} & \boldsymbol{G}_{cc} \end{bmatrix} \begin{Bmatrix} \delta\boldsymbol{q} \\ \delta\boldsymbol{q}' \end{Bmatrix}_i - \begin{Bmatrix} \int_{Y_e - Y_c} [\boldsymbol{P}^m]^{\mathrm{T}} \{\delta\bar{\boldsymbol{e}}_i\} \,\mathrm{d}Y \\ \int_{Y_c} [\boldsymbol{P}^c]^{\mathrm{T}} \{\delta\bar{\boldsymbol{e}}_i\} \,\mathrm{d}Y \end{Bmatrix} \tag{64}$$

In Eq. (64), it is assumed that the stress coefficients $\boldsymbol{\beta}$ and generalized nodal displacements $\boldsymbol{q}$ are perturbed about their respective equilibriated and compatible values, corresponding to a prescribed perturbation in $\bar{\boldsymbol{e}}_i$. The nodal displacements $\delta\boldsymbol{q}$ in Eq. (64) are solved by linearization of the global traction reciprocity condition (37) with respect to $\bar{\boldsymbol{e}}_i$, given as

$$\sum_{e=1}^{N} [\boldsymbol{G}]^{\mathrm{T}} \left([\boldsymbol{H}]^{-1} [\boldsymbol{G}] \begin{Bmatrix} \delta\boldsymbol{q} \\ \delta\boldsymbol{q}' \end{Bmatrix}_i - [\boldsymbol{H}]^{-1} \begin{Bmatrix} \int_{Y_e - Y_c} [\boldsymbol{P}^m]^{\mathrm{T}} \{\delta\bar{\boldsymbol{e}}_i\} \,\mathrm{d}Y \\ \int_{Y_c} [\boldsymbol{P}^c]^{\mathrm{T}} \{\delta\bar{\boldsymbol{e}}_i\} \,\mathrm{d}Y \end{Bmatrix} \right) = 0 \tag{65}$$

The solved values of $\{\delta\boldsymbol{q}\}_i$ yield the characteristic modes of deformation as plotted in Figs. 16–18. These are subsequently substituted in the local compatibility equation (64) to solve for element stress coefficients $\{\delta\boldsymbol{\beta}\}_i$. It should be noted the tangent modulus is evaluated from unit values of $\{\delta\bar{\boldsymbol{e}}_i\}$, i.e.

$$\{\delta\bar{\boldsymbol{e}}_1\} = \begin{Bmatrix} 1 \\ 0 \\ 0 \end{Bmatrix}, \quad \{\delta\bar{\boldsymbol{e}}_2\} = \begin{Bmatrix} 0 \\ 1 \\ 0 \end{Bmatrix}, \quad \{\delta\bar{\boldsymbol{e}}_3\} = \begin{Bmatrix} 0 \\ 0 \\ 1 \end{Bmatrix}.$$

Components of the elatic-plastic homogenized tangent modulus tensor E^H_{ijkl} are then obtained from Eq. (27), by averaging $[\boldsymbol{P}]\{\mathrm{d}\boldsymbol{\beta}\}_i$ for each component of the macroscopic strain, as

$$[\boldsymbol{E}^H] = \frac{1}{|\boldsymbol{Y}|} \left[\sum_{e=1}^{N} \int_{Y_e} [\boldsymbol{P}]\{\mathrm{d}\boldsymbol{\beta}\}_1 \ \sum_{e=1}^{N} \int_{Y_e} [\boldsymbol{P}]\{\mathrm{d}\boldsymbol{\beta}\}_2 \ \sum_{e-1}^{N} \int_{Y_e} [\boldsymbol{P}]\{\mathrm{d}\boldsymbol{\beta}\}_3 \right] \tag{66}$$

5. Numerical implementation

A number of numerical details have to be considered in the construction of a multiple scale computational model using the microstructural VCFEM model. In this section, a few salient features are discussed.

5.1. Incorporation in the macroscopic analysis module

The Voronoi cell finite element module is incorporated in a macroscopic analysis module with the interface being created by the homogenization procedure. In this work, the general purpose commercial code ABAQUS has been chosen to serve as the macroscopic analysis program. Macroscopic ABAQUS models are developed with two-dimensional elements. The material constitutive relation at each integration point of ABAQUS elements is input through the homogenization process by using results from the microscopic VCFEM analysis. This interface between ABAQUS and VCFEM is created through UMAT, intended to incorporate user specified constitutive models in ABAQUS. The analysis code resulting from this macro–micro coupling is termed as VCFEM-HOMO. QUAD4 elements with one-point reduced integration and hourglass control are selected in ABAQUS analysis. ABAQUS and VCFEM codes used in this analysis implement implicit time integration schemes, and hence require iterations at both levels for convergence.

Within each iteration loop of macroscopic analysis in the pth increment, microscopic state variables are computed in VCFEM using given values of the macroscopic strains at the beginning of the increment and its increment, as shown in the flow chart of Fig. 2. The microscopic stresses are averaged to yield macroscopic stresses. Upon convergence in global and local iterations, the microscopic VCFEM is invoked again to evaluate the homogenized elastic-plastic tangent modulus $\boldsymbol{E}^H$ by applying unit components of macroscopic strain. All the history dependent microstructural variables, e.g. stresses, strains and plastic strains are retained and updated during the incremental process.

5.2. *Implementing periodicity boundary condition*

An essential step in computing the homogenized material properties is to ensure repeatability boundary conditions on the RME. For a square or rectangular RME, identical displacement functions must be specified for corresponding nodes (equidistant from a coordinate axis) on opposite edges. Implementing the repeatability boundary condition for a regular finite element mesh is straightforward, since a uniform mesh can be generated to have the correspondence between boundary nodes on opposite faces. However, boundary nodes of the Voronoi mesh generated by Dirichlet tessellation, are in general quite arbitrary and such a correspondence cannot be easily established. A method which involves representation of nodal boundary displacements by a suitable polynomial function is implemented for enacting the repeatability conditions. In this method, a $(q-1)$th order polynomial is chosen for the displacements, where q corresponds to the highest number of boundary nodes between the two opposite faces. That is, if one face has 5 nodes while the opposite side consists of 6 nodes, a 5th order polynomial function is chosen. The edge nodal displacements are then written as

$$\begin{aligned}
u_1 &= a_0 + a_1x_1 + a_2x_1^2 + a_3x_1^3 + a_4x_1^4 + a_5x_1^5 \\
v_1 &= b_0 + b_1y_1 + b_2y_1^2 + b_3y_1^3 + b_4y_1^4 + b_5y_1^5 \\
u_2 &= a_0 + a_1x_2 + a_2x_2^2 + a_3x_2^3 + a_4x_2^4 + a_5x_2^5 \\
v_2 &= b_0 + b_1y_2 + b_2y_2^2 + b_3y_2^3 + b_4y_2^4 + b_5y_2^5 \\
&\vdots
\end{aligned} \tag{67}$$

where $u_1, v_1, u_2, v_2 \ldots$ are nodal displacements and $x_1, y_1, x_2, y_2 \ldots$ are boundary coordinates. These lead to displacement constraints in the matrix equations prior to solving.

6. Numerical examples

Numerical examples conducted with the multiple scale homogenization module VCFEM-HOMO, are divided into two categories. The first set of examples are intended to validate the effectiveness of the asymptotic homogenization in conjunction with Voronoi cell FEM formulation for heterogeneous materials with both inclusions and voids. This is accomplished through comparison of VCFEM-HOMO results in simple tests, with (a) those generated by Unit cell models using conventional finite element codes such as ABAQUS, (b) experimental/analytical results, and (c) effective continuum models. The comparisons also help in identifying some of the shortcomings of alternative approaches, and where coupled multiple scale analyses is desirable. In the second set of examples, the VCFEM-HOMO code is used to solve more complex multiple scale problems with various microstructural morphologies. Effects of the microsctructure in the evolution of macroscopic and microscopic variables are investigated. The material in all the ensuing examples is assumed to be a FT/Al composite or aluminum with voids, unless otherwise mentioned. The FT fiber is assumed to be elastic while the aluminum matrix is an elastic-plastic material with the following properties.

Material Properties:
FT fiber (99% crystalline α-alumina (Al_2O_3) coated with silica)
Young's Modulus (E_c): 344.5GPa Poisson Ratio (ν_c): 0.26

2 wt% Li-Al binary alloy matrix
Young's Modulus (E_m): 68.9 GPa Poisson Ratio (ν_m): 0.32
Initial Yield Stress (Y_0): 94 MPa Post Yield flow rule: $\epsilon_{\text{eqv}} = Y_0/E_m\{\sigma_{\text{eqv}}/Y_0\}^5$

The microstructural VCFEM analysis uses a 48 term stress function in Eq. (41) ($p + q = 2...4$ and $i = 1...3$) for the matrix of porous materials, and a 34 term stress function ($p + q = 2$ and $i = 1...3$) in the matrix of composite materials. The stress field in the inclusion for composite materials is generated with a 25 term polynomial stress function (i.e. Φ^c_{poly}: $p + q = 2...6$)). It should be noted that elastic problems with homogenization and VCFEM have been successfully solved in [28].

6.1. Validation of the homogenization model

6.1.1. Numerical unit cell models

In this example, results of VCFEM-HOMO are compared with predictions of numerical unit cell models for plane strain elastic-plastic analysis. Two microstructural arrangements, viz. square edge distribution (SED) and hexagonal distribution (HD) as shown in Fig. 5, are considered. For VCFEM-HOMO

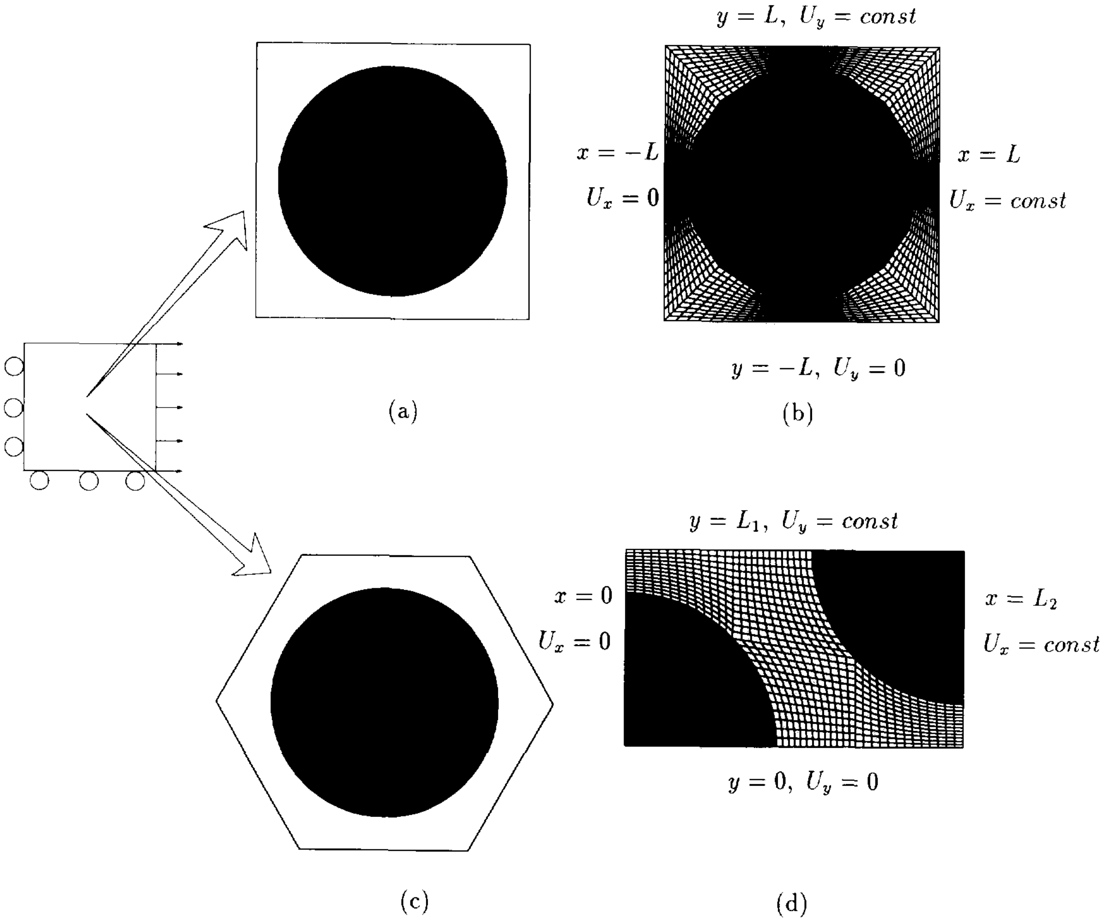

Fig. 5. Computational model of a composite material with a circular inclusion of volume fraction 55%. (a) Macroscopic and microscopic models for square edge distribution by VCFEM-HOMO; (b) microstructural ABAQUS Unit Cell model for Square edge distribution; (c) macroscopic and microscopic models for Hexagonal distribution by VCFEM-HOMO; (d) microstructural ABAQUS Unit Cell model for Hexagonal distribution.

analysis, the macroscopic ABAQUS mesh consists of a single QUAD4 element, and a single Voronoi cell element is required for microstructural analysis as shown in Fig. 5(a) and (c). Unit cell analyses are conducted at the microstructural level only, with the representative material element (RME) modeled by QUAD4 elements in ABAQUS, illustrated in Fig. 5(b) and (d). The inclusion volume fraction is 55%. The periodic construct of unit cell is achieved through restrictive repeatability conditions enforced on edges $x = L$ and $y = L$. This constraint condition requires rectangular cells to deform into rectangular shapes, i.e. straight line edges ($x = L, y = L$) move uniformly as straight lines. For the SED and HD arrangements, the ABAQUS mesh consists of 1440 and 1482 QUAD4 elements, respectively.

Comparisons are made for macroscopic as well as microscopic response by the two approaches. For the unit cell model, macroscopic variables denoted with an overbar, are obtained by volume averaging the microscopic response. For example, macroscopic stresses $\bar{\boldsymbol{\sigma}}$ are evaluated as:

$$\bar{\boldsymbol{\sigma}} = \boldsymbol{\Sigma} = \frac{\int_{\Omega_{\mathrm{RME}}} \boldsymbol{\sigma}\, \mathrm{d}\Omega}{\int_{\Omega_{\mathrm{RME}}} \mathrm{d}\Omega}$$

Figs. 6 and 7 show the macroscopic stress–strain relations and the microscopic stress distribution for the square edge and hexagonal packings, respectively, when subjected to uniform stretching. Figs. 6(a) and 7(a) show excellent agreement between VCFEM-HOMO and Unit Cell model in the macroscopic responses at all load stages. Figs. 6(b) and 7(b) show the microscopic stress distribution in the direction of applied strain along sections at $y = L/2$ and $y = 0$ in Figs. 5(b) and (d), respectively. Though the VCFEM-HOMO results for both packings compare well with unit cell predictions, better agreement is seen with HD packing due to the refined unit cell mesh along the section considered.

VCFEM-HOMO code is next utilized to investigate the effect of microstructural morphology on the material response. Four different arrangements are considered with circular inclusions of 55% volume fraction, viz. (a) square edge distribution (Fig. 5(a)), (b) hexagonal distribution (Fig. 5(c)), (c) square diagonal distribution (45° rotation of Fig. 5(a)) and (d) random distribution with 29 inclusions (Fig. 8) The ABAQUS macroscopic mesh consists of one plane strain element, subjected to simple tension and simple shear boundary conditions to maximum effective strains of 0.008. The effective macroscopic stress–strain behavior is depicted in Fig. 9. On account of the rotational equivalence of RMEs, the behavior of the square edge and square diagonal distributions are exactly reversed for the two loading conditions. The results indicate the strong anisotropy in overall behavior of these two RMEs. The random and hexagonal packings, on the other hand, exhibit similar response in tension and shear. This establishes the low directional dependency of these RMEs, implying near isotropic behavior. The stress–strain curves for the latter two distributions lie within the envelopes of the SE and SD distributions, and hence exhibit more overall ductility.

6.1.2. Effective continuum models

This set of examples examines some of the differences between effective continuum models and coupled macro–micro analysis for simple loadings. Furthermore, the VCFEM-HOMO code is also tested against experimental and analytical results.

In the first example, overall stress–strain plots are first generated by uniaxial stretching of VCFEM models in Figs. 5(a) and 8 under plane stress conditions. This is then input as the homogenized material law in ABAQUS with isotropic hardening and associated flow rule. The ABAQUS mesh with this effective continuum model consists of one QUAD4 element. Likewise, the macroscopic ABAQUS mesh for VCFEM-HOMO consists of one QUAD4 element and the microscopic models are illustrated in Figs. 5(a) and 8. Macroscopic longitudinal stress–strain relations, and transverse-longitudinal strain relations by the two approaches are plotted in Figs. 10 and 11. Comparisons are made for three different microstructures, viz. (a) square edge packing with 10% inclusion volume fraction, (b) square edge packing with 55% inclusion volume fraction, and (c) random packing with 55% inclusion volume fraction. The stress and strain plot in the loading direction (Fig. 10) shows excellent agreement between the continuum model and VCFEM-HOMO results. An increase in the inclusion volume fraction leads to a considerable reduction in the ductility due to the higher stiffness of the elastic inclusion. Though the

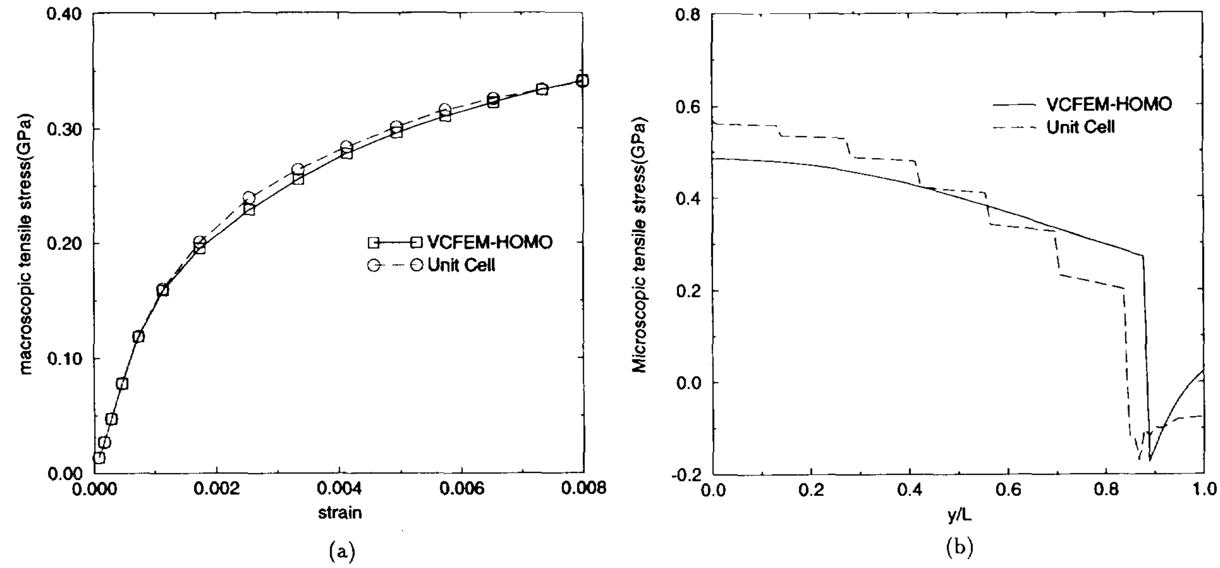

(a) (b)

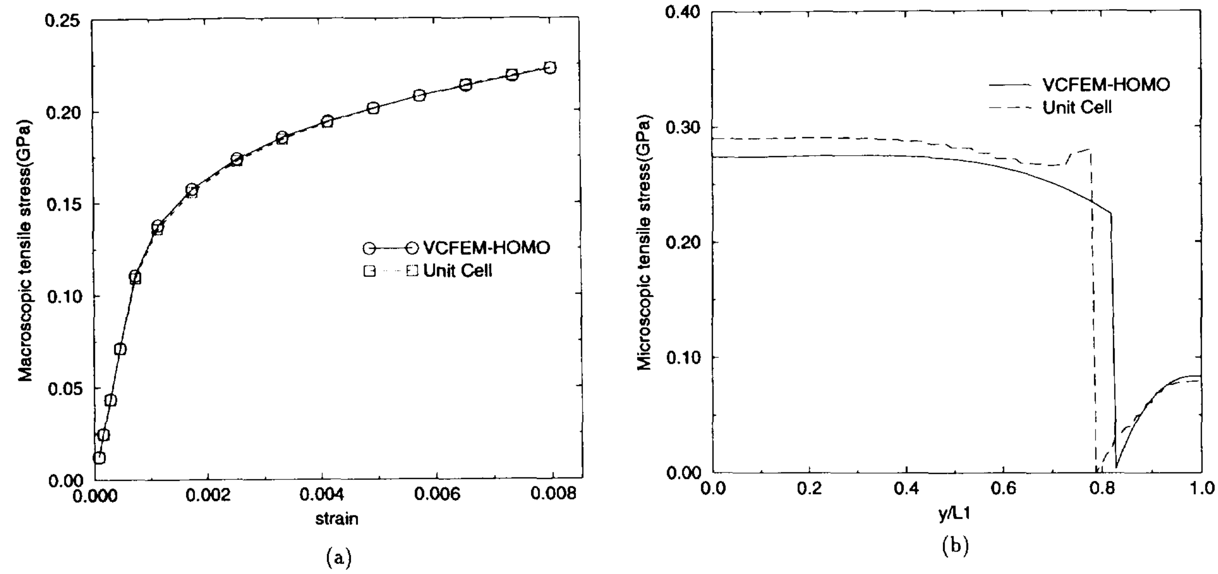

(a) (b)

Fig. 6. Comparison of macroscopic and microscopic response for Square edge packing composite between VCFEM-HOMO and Unit Cell models. (a) Macroscopic stress–strain response along the load direction; (b) microstructural stress distribution along a section through the inclusion $y = L/2$.

Fig. 7. Comparison of macroscopic and microscopic response for Hexagon packing composite between VCFEM-HOMO and Unit Cell models. (a) Macroscopic stress–strain response along the load direction; (b) microstructural stress distribution along a section through the inclusion $y = 0$.

random distribution shows a less stiff response than the square edge distribution for the same volume fraction (55%), this plot confirms that the effect of volume fraction is much more pronounced that that of distribution. The two approaches are at considerable variance in the transverse-longitudinal strain plot (Fig. 11). The continuum model shows nearly identical strain responses for all inclusion volume fractions and distributions. This can be explained by the fact that the continuum models assume total yielding of the microstructure after initial yield, and consequently enforces the constraint that macroscopic plastic

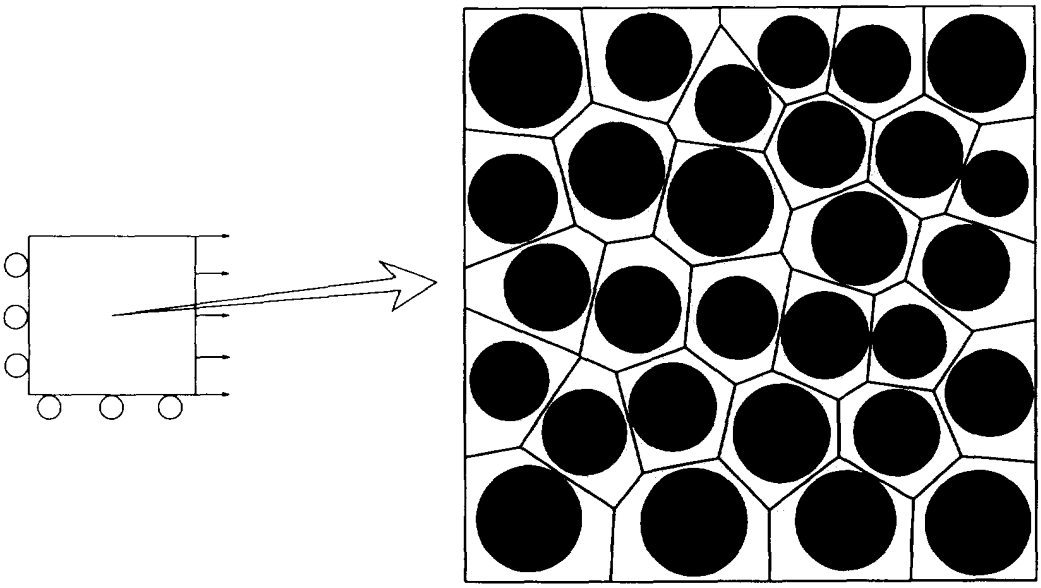

Fig. 8. RME for a randomly distributed composite with 29 circular inclusions at 55% volume fraction.

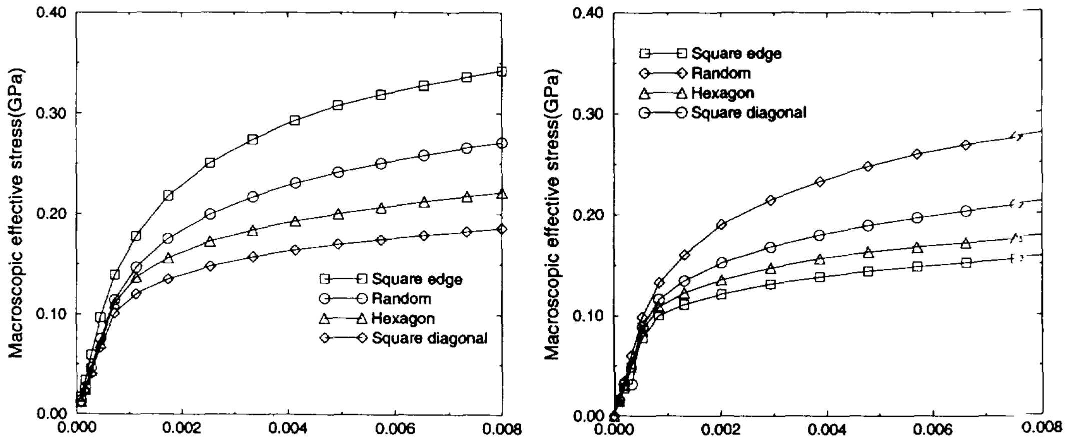

(a) (b)

Fig. 9. Effective macroscopic stress–strain responses of various distributions under (a) simple tension (b) simple shear.

strains are volume preserving. This leads to direct dependence of transverse plastic strains on the longitudinal strains, and the microstructure contributes only to the elastic part of the transverse strain. The behavior is however quite different when solved with VCFEM-HOMO. In reality, only a part of the microstructure yields at the strains considered, and this is reflected in the VCFEM-HOMO results. For smaller inclusion volume fractions, a large portion of the unit cell is the matrix that goes plastic at initial yield. This gives the close proximity in prediction by both models. This behavior changes significantly at higher volume fraction, where larger portions of the matrix remain elastic. The absolute value of the transverse strain by VCFEM-HOMO is much smaller than that of effective continuum model. Another

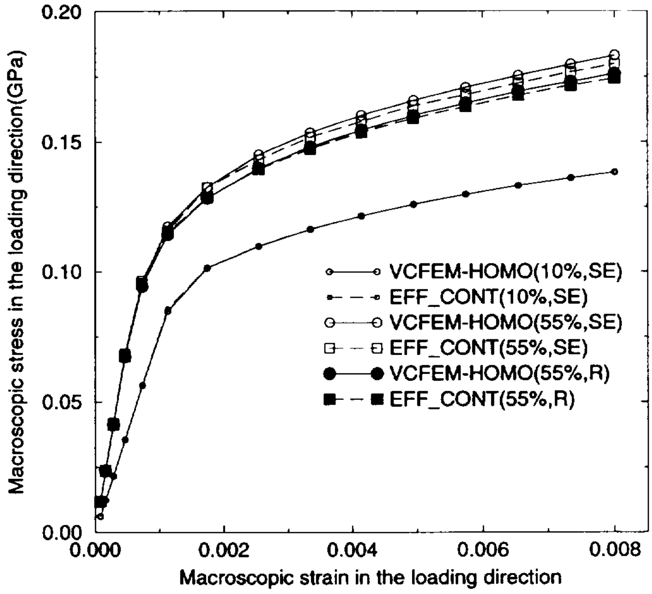

Fig. 10. Macroscopic stress–strain relations for various microstructures by VCFEM-HOMO and effective continuum model.

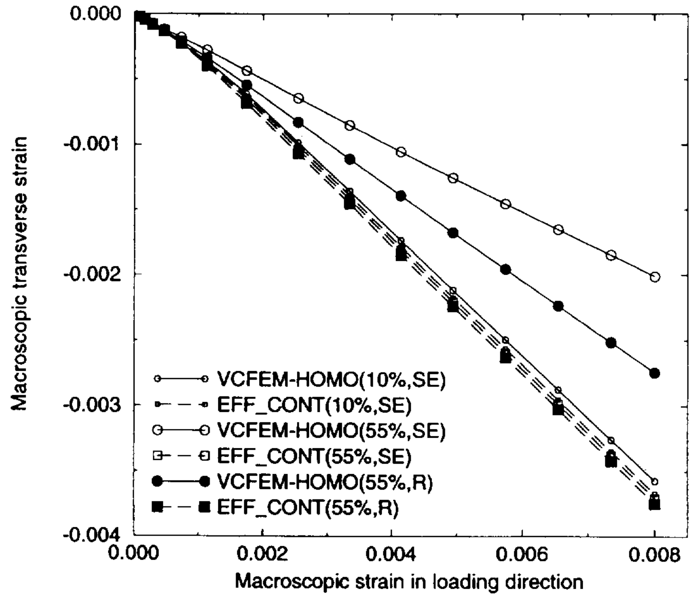

Fig. 11. Transverse strain-axial strain relations for various microstructures by VCFEM-HOMO and effective continuum model.

observation is that the difference between VCFEM-HOMO and continuum model results for the random microstructure is less than that for the square edge microstructure. This may be attributed to the anisotropic behavior of the latter that is not accounted for in the continuum models. This example clearly points out the need for using the coupled analysis especially at higher volume fractions of heterogeneous microstructures.

The second example deals with porous materials, for which VCFEM-HOMO results are compared with the Tvergaard–Gurson (T–G) continuum model [38, 39]. Plane strain simple tension, simple shear, and biaxial tension tests are carried out for square edge packed materials with a low void volume fraction of 5%. For comparison plane strain simulations, the T–G model for long cylindrical voids [38] is implemented in ABAQUS through the UMAT window. In this module, numerical integration of the rates of state variables is carried out in a way similar to Aravas [40], for spherical voids. The macroscopic ABAQUS model for both analyses consists of one QUAD4 element and the microscopic model for VCFEM-HOMO is illustrated in Fig. 5. The yield condition in the plane strain T–G model [38] is stated as

$$\Phi = \frac{\sigma_e^2}{\sigma_o^2} + 3\,f\cosh\left(-\frac{\sqrt{3}\,(\sigma_{11}+\sigma_{22})}{2\,\sigma_o}\right) - (1+2.25\,f^2) \tag{68}$$

where σ_e is the effective stress, σ_o is the matrix flow stress, f is the void volume fraction and σ_{ij} are the principal components of the Cauchy stress tensor. An important assumption in this model is:

$$(1-f)\sigma_o\dot{\epsilon}_o^{p} = \sigma_{ij}\dot{\epsilon}_{ij}^{p} \tag{69}$$

which means that the equivalent plastic work is derived solely from the entire matrix part of the microstructure.

Effective stress–strain plots in simple tension and simple shear (Figs. 12(a) and (b)) show good agreement between two methods, with T–G model producing a slightly higher value of initial yield. This is because, yield in the T–G model is manifested only after a significant portion of the microstructure has become plastic. VCFEM-HOMO, on the other hand, shows signs of inelasticity at the very onset of plastic deformation in the microstructure. The two approaches are, however, at significant variance for the biaxial loading case as seen in Fig. 13(a). Though the initial yield points are fairly close, the post yield behavior shows considerable difference between two models. As in the previous example, the main reason for this difference may be attributed to the assumption in T–G model that the entire microstructural matrix becomes plastic upon initial yield. In biaxial loading, as $(\sigma_{11}+\sigma_{22})$ increases in Eq. (68), the effective macroscropic stress σ_e must diminish to near zero values for satisfying the yield condition. Physically, this also indicates that the large regions of plastic localization causes the effective stress to drop drastically. From the VCFEM-HOMO simulation it is however seen in Fig. 13(b), that a significant portion of the microstructure does not yield. Consequently, the effective stress in Fig. 13(a) is higher by VCFEM-HOMO than by the T–G predictions at the end of loading.

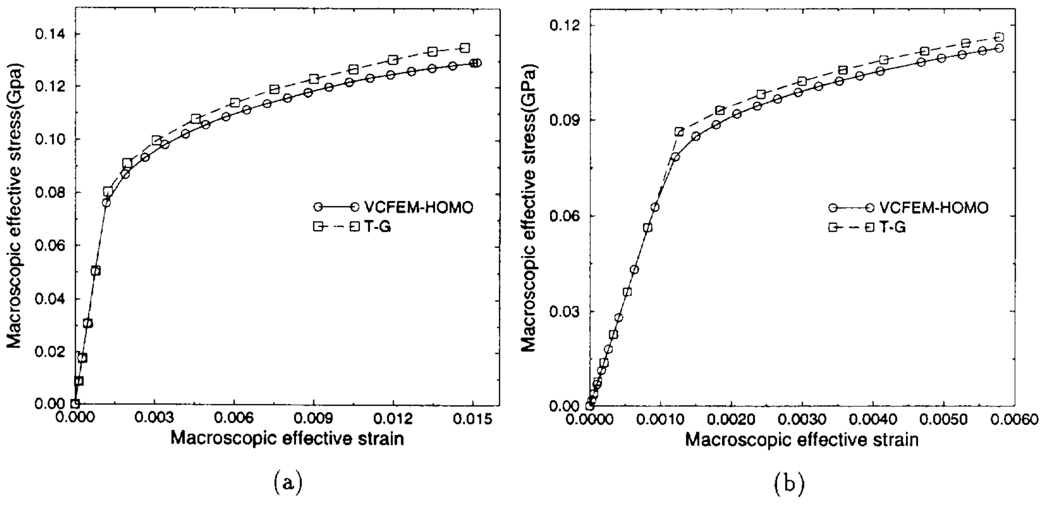

(a) (b)

Fig. 12. Effective macroscopic stress–strain plots by VCFEM-HOMO and Tvergaard-Gurson model for 5% void volume fraction in plane strain. (a) Simple tension; (b) simple shear.

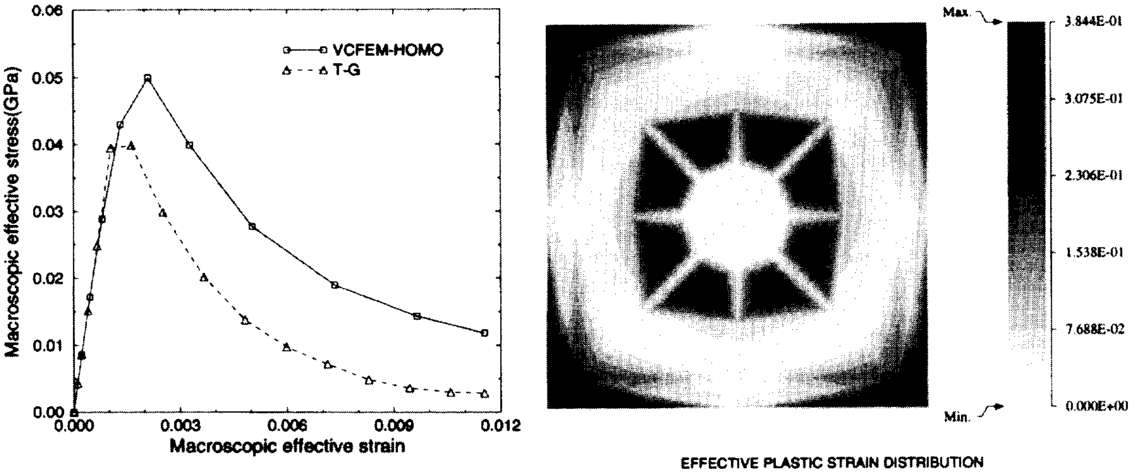

(a) (b)

Fig. 13. (a) Effective macroscopic stress–strain plots by VCFEM-HOMO and Tvergaard-Gurson model for 5% void volume fraction in biaxial tension; (b) Contour plot of microstructural effective plastic strain at the end of loading.

As a final example a multiple scale analysis for a porous plate with a hole is conducted by VCFEM-HOMO and compared with the T–G model incorporated in ABAQUS. Uniaxial tension of the plate is considered under plane strain conditions. The representative material element (RME) in the VCFEM-HOMO analysis is a square edge packing with 5% circular void volume fraction. Figs. 14(a) and (b) shows excellent agreement in contour plots of effective macroscopic stress distribution by VCFEM-HOMO and ABAQUS with T–G model. The stress–strain evolution at three specific points (A), (B) and (C) are compared in Fig. 14(c). This near perfect match is expected, since most points in the plate are essentially in an uniaxial state of stress.

6.1.3. Comparisons with some analytical and experimental results

Plane strain VCFEM-HOMO results are compared with analytical 2 and 3-phase model predictions due to Zhao and Weng [41] and experimental results due to Adams [42] for unidirectional composites. The material properties are:

Aluminum

$E = 58$ GPa (Young's Modulus), $\nu = 0.33$ (Poisson's Ratio)

$Y_0 = 89$ MPa (Initial Yield Stress), $\sigma_{\mathrm{eqv}} = Y_0 + 175(\epsilon_{\mathrm{eqv}}^{\mathrm{pl}})^{0.125}$ MPa (Post Yield Hardening Law)

Boron

$E = 385$ GPA (Young's Modulus), $\nu = 0.2$ (Poisson's Ratio)

A square macroscopic element, that has a microstructural RME of a 2×1 rectangular edge packing with a circular inclusion of $V_f = 34\%$, is loaded in uniaxial tension. Fig. 15 shows that VCFEM-HOMO results provide a better agreement with experimental results than the analytical model, which assume a square edge packed RME.

6.1.4. Characteristic modes in elastic-plastic deformation

Characteristic modes in elastic-plastic homogenization represent instantaneous microstructural deformation response to applied unit components of macroscopic strain tensor. These modes χ_{p}^{kl} are obtained from Eq. (65). Characteristic modes are essential in obtaining the elastic-plastic tangent modulus E_{ijkl}^{H} for macroscopic analysis.

The macroscopic element is subjected to uniaxial stretching, and the microstructural RMEs considered are square edge/random packing for circular voids (20% volume fraction), and square edge packing for circular inclusion (40% volume fraction). Fig. 16(a) and (b) show the characteristic modes for the porous

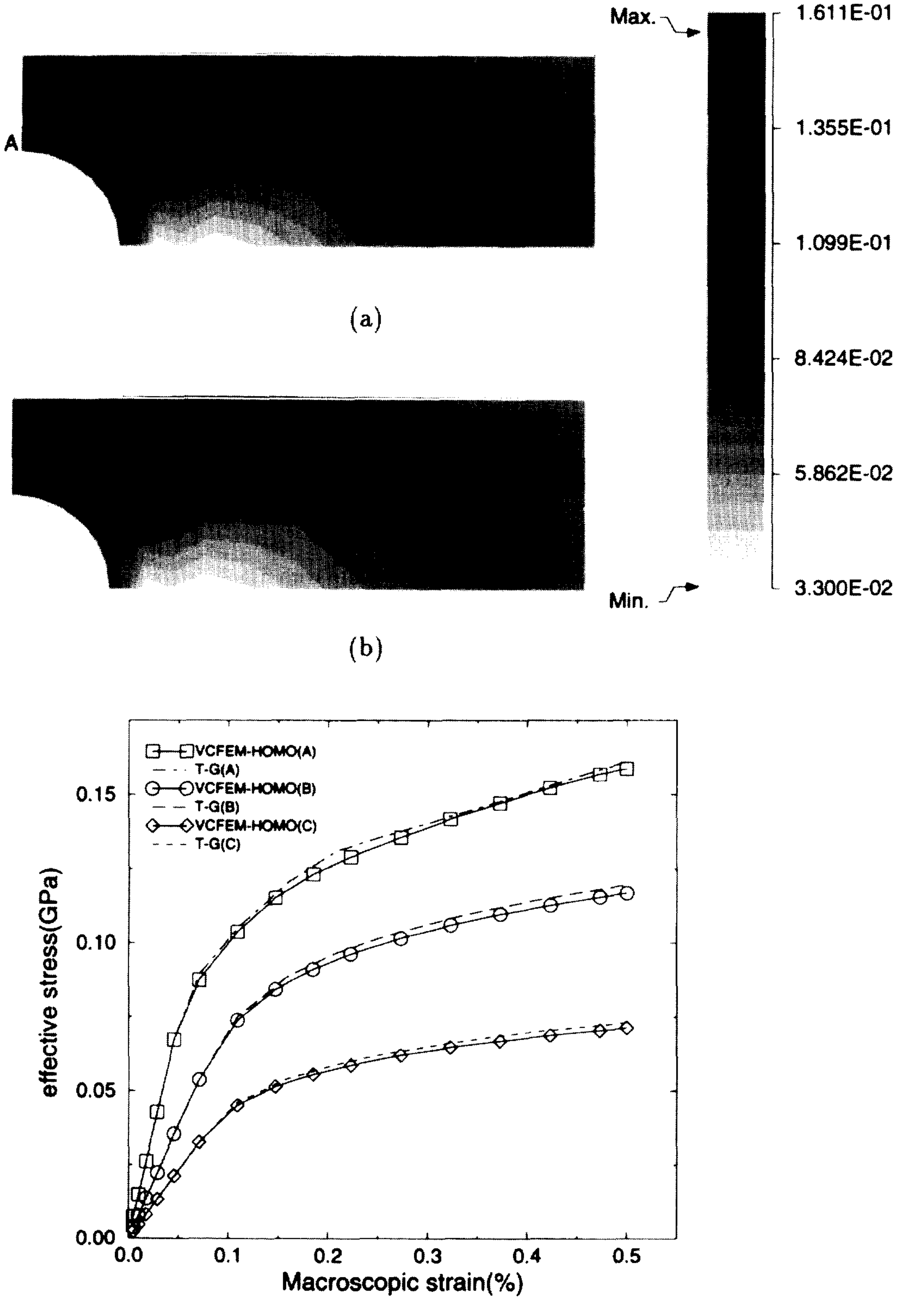

(a)

(b)

(c)

Fig. 14. Macroscopic effective stress distribution in a plate with a hole in uniaxial tension at 5% strain. (a) By VCFEM-HOMO; (b) ABAQUS with T–G model (c) effective stress–strain evolution plots at three points in the structure.

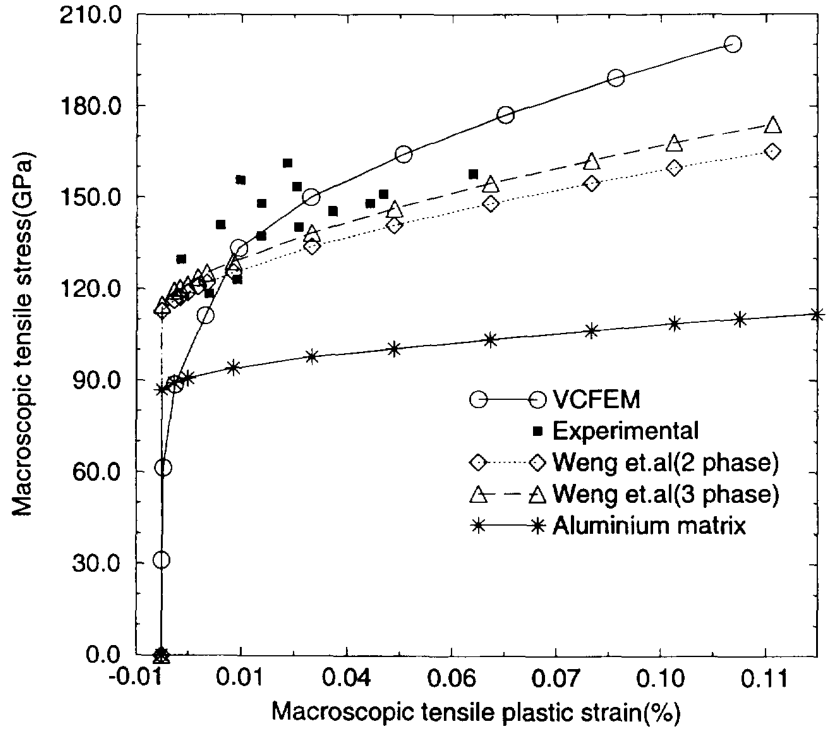

Fig. 15. Macroscopic stress–strain responses for a Boron-Aluminum composite by VCFEM-HOMO, analytical and experimental techniques.

material and corresponding tangent modulus at the beginning of the loading and after 1% macroscopic stretching, respectively. The initial modes depict the deformed void aligned in the direction of straining, but this changes with plastic straining, implying the influence of internal variable evolution. Fig. 17 shows corresponding modes for the random microstructure. Fig. 18 shows characteristic modes for composite microstructure with regular distribution. The difference between the modes for porous and composite materials emanates from the high inclusion stiffness that results in larger matrix deformation.

6.2. *Multiple scale analysis*

Two problems are considered for multiple scale analysis with VCFEM-HOMO. The effects of various distributions, sizes, and shapes, on the overall behavior of the heterogeneous material is investigated. In particular, the RME's considered are (a) square edge packing with a circular heterogeneity, (b) square diagonal packing with a circular heterogeneity, (c) random packing with 15 circular heterogeneities and (d) random packing with 15 elliptical heterogeneities. The material microstructure is assumed to consist of voids, inclusions, or a combination of both.

6.2.1. *Plane strain analysis of plate with holes*

This set of examples deals with a thick plate with an uniform array of large circular holes in plane strain uniaxial tension. Only a portion of the plate, shown in Fig. 19(a), is considered from symmetry considerations. Dimensional details are given in the Fig. 19(a). The macroscopic ABAQUS model consists of 128 QUAD4 elements. The left and right edges are constrained to move in vertical straight lines, and the top and bottom edges are pulled to an overall strain of 0.5%.

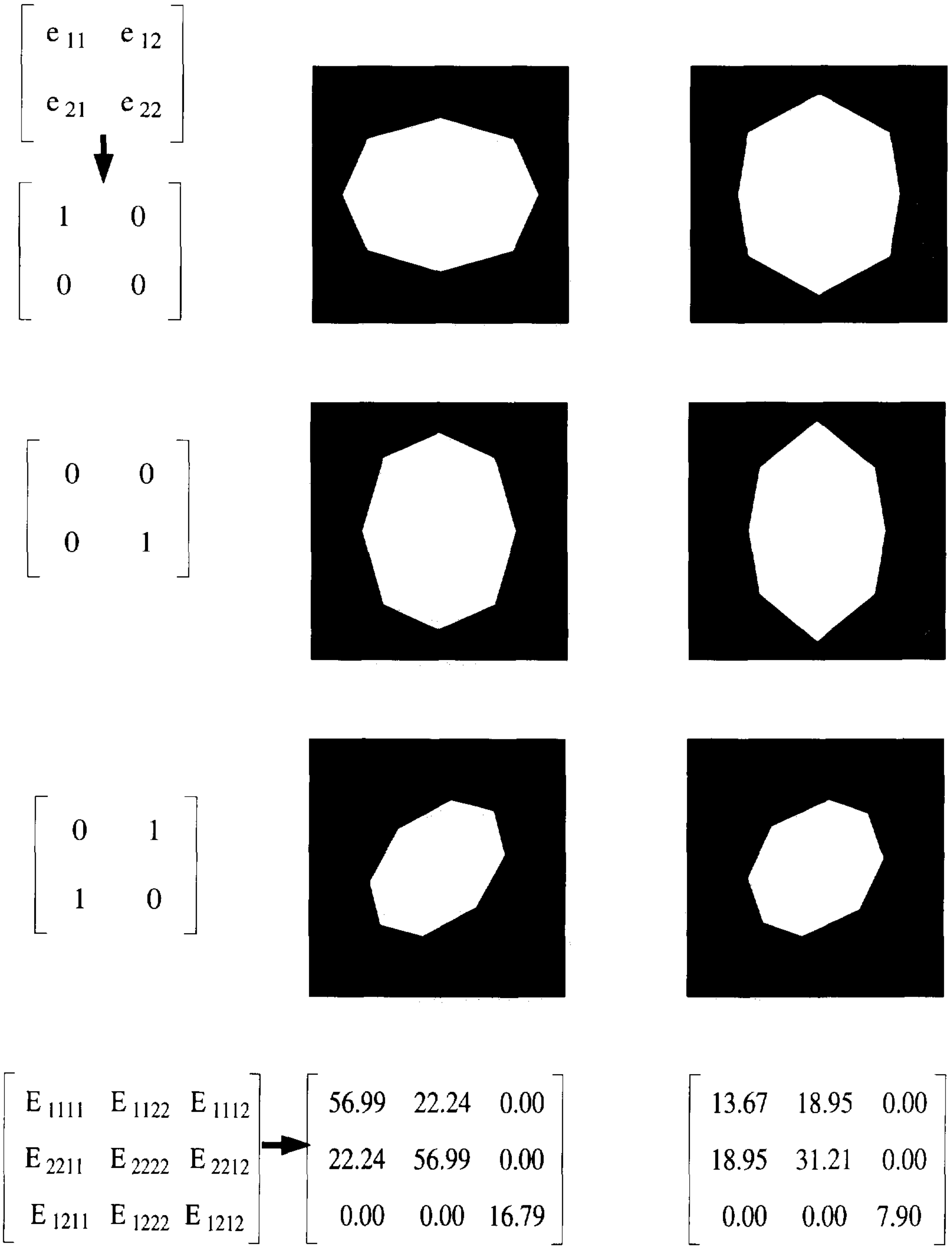

$$\begin{bmatrix} e_{11} & e_{12} \\ e_{21} & e_{22} \end{bmatrix} \downarrow \begin{bmatrix} 1 & 0 \\ 0 & 0 \end{bmatrix} \quad \begin{bmatrix} 0 & 0 \\ 0 & 1 \end{bmatrix} \quad \begin{bmatrix} 0 & 1 \\ 1 & 0 \end{bmatrix}$$

$$\begin{bmatrix} E_{1111} & E_{1122} & E_{1112} \\ E_{2211} & E_{2222} & E_{2212} \\ E_{1211} & E_{1222} & E_{1212} \end{bmatrix} \rightarrow \begin{bmatrix} 56.99 & 22.24 & 0.00 \\ 22.24 & 56.99 & 0.00 \\ 0.00 & 0.00 & 16.79 \end{bmatrix} \quad \begin{bmatrix} 13.67 & 18.95 & 0.00 \\ 18.95 & 31.21 & 0.00 \\ 0.00 & 0.00 & 7.90 \end{bmatrix}$$

Fig. 16. Characteristic modes for voided RME with square edge distribution. (a) At the start of loading; (b) after 1% stretching.

In the first example, a porous microstructure with a 40% void volume fraction is considered. Various morphologies are considered are shown in Figs. 19(b)–(e). Figs. 20, 22, 24 and 26 show the effective stress contours plots, and Figs. 21, 23, 25 and 27 show the contours plots of the effective plastic strains at the structural level and also in a microstructural RME at the corner point A. It is observed that the maximum effective stress generally occurs at this point. The macroscopic effective stress distributions exhibit very similar patterns for all microstructures considered. There is a narrow ligament between two large holes

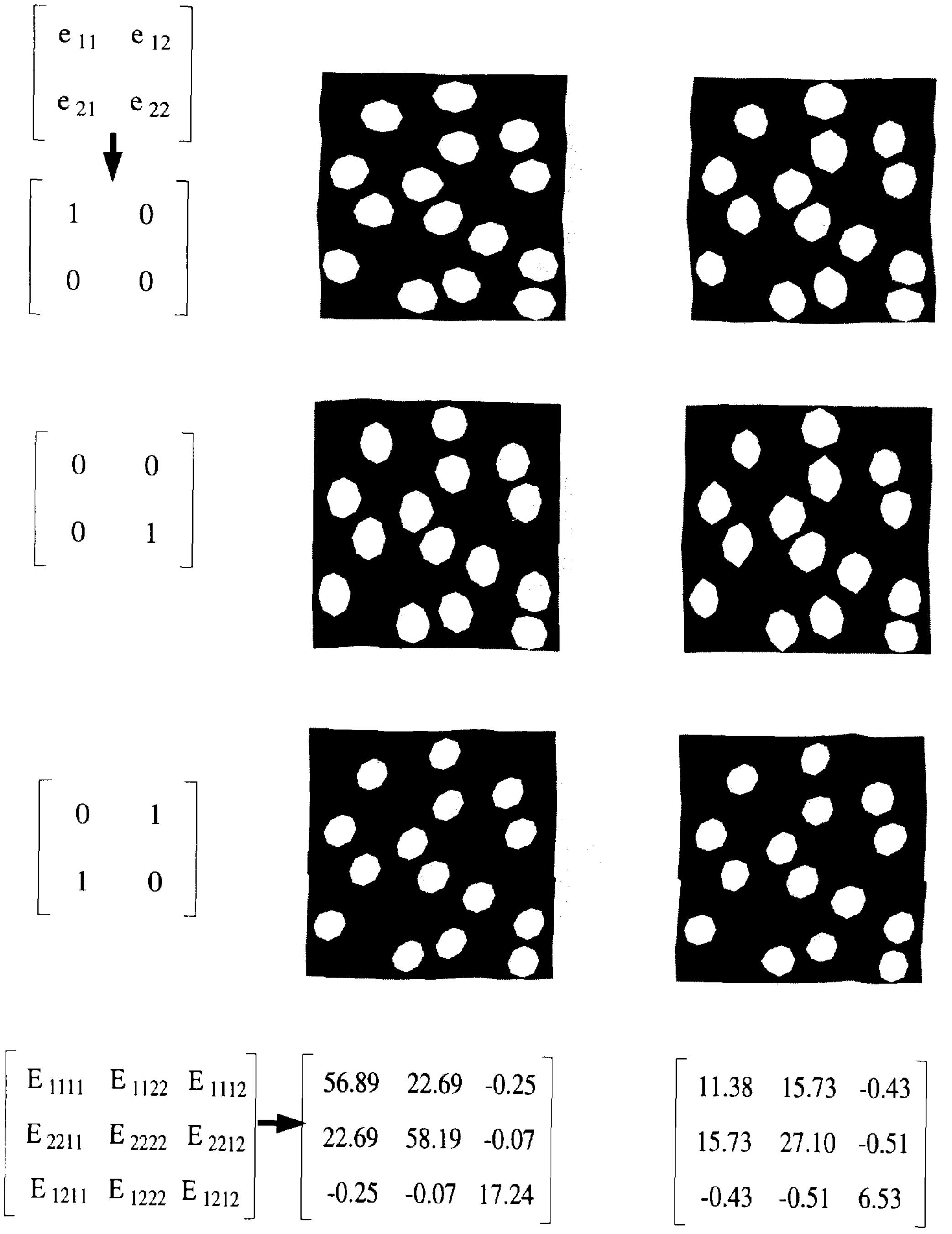
e11 e12
e21 e22
1 0
0 0
0 0
0 1
0 1
1 0
E1111 E1122 E1112
E2211 E2222 E2212
E1211 E1222 E1212
56.89 22.69 -0.25
22.69 58.19 -0.07
-0.25 -0.07 17.24
11.38 15.73 -0.43
15.73 27.10 -0.51
-0.43 -0.51 6.53

Fig. 17. Characteristic modes for voided RME with random distribution. (a) At the start of loading; (b) after 1% stretching.

along which strains localize as the deformation intensifies. Similarity in the patterns of macroscopic stress distribution is explained from an observation that the macroscopic state of stress at each point is essentially uniaxial. Thus, anisotropy emanating from the microstructural morphology does not play an important role in this example. Magnitude of stresses and plastic strains are however considerably different depending on the microstructural arrangement. This is further evidenced in a macroscopic

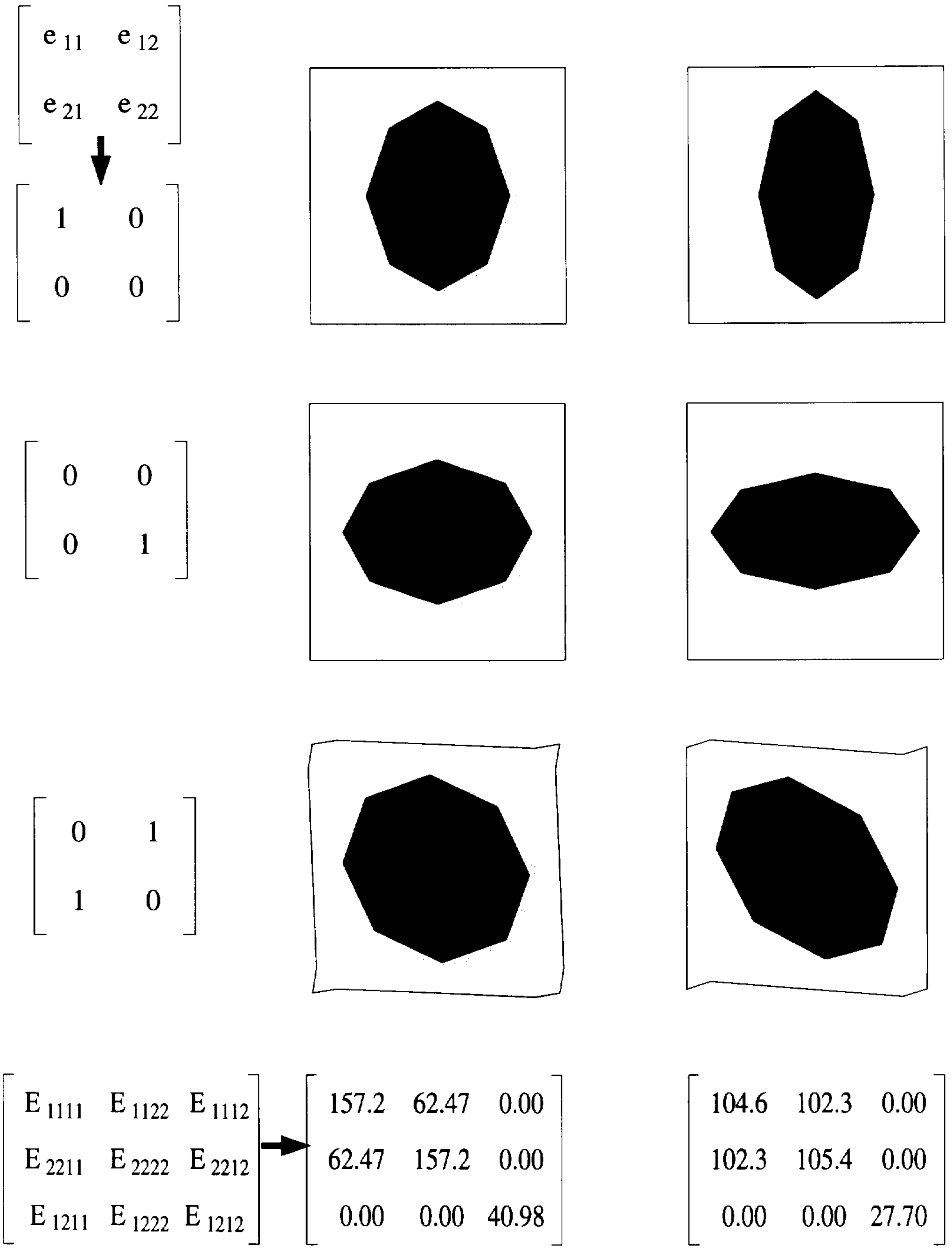

$$\begin{bmatrix} e_{11} & e_{12} \\ e_{21} & e_{22} \end{bmatrix} \downarrow \begin{bmatrix} 1 & 0 \\ 0 & 0 \end{bmatrix} \qquad \begin{bmatrix} 0 & 0 \\ 0 & 1 \end{bmatrix} \qquad \begin{bmatrix} 0 & 1 \\ 1 & 0 \end{bmatrix}$$

$$\begin{bmatrix} E_{1111} & E_{1122} & E_{1112} \\ E_{2211} & E_{2222} & E_{2212} \\ E_{1211} & E_{1222} & E_{1212} \end{bmatrix} \rightarrow \begin{bmatrix} 157.2 & 62.47 & 0.00 \\ 62.47 & 157.2 & 0.00 \\ 0.00 & 0.00 & 40.98 \end{bmatrix} \qquad \begin{bmatrix} 104.6 & 102.3 & 0.00 \\ 102.3 & 105.4 & 0.00 \\ 0.00 & 0.00 & 27.70 \end{bmatrix}$$

Fig. 18. Characteristic modes for composite RME with square edge distribution. (a) At the start of loading; (b) after 1% stretching.

stress–strain plot (Fig. 28 (a)) at the point *A*. The square edge and square diagonal distributions yield nearly identical response. The random void distributions exhibit significantly more ductile behavior compared to the regular distributions. The ductility in the random distribution stems from the plastic strain concentration in regions of clustered voids.

A comparison of the macroscopic and microscopic contour plots reveals that the true stress in the mi-

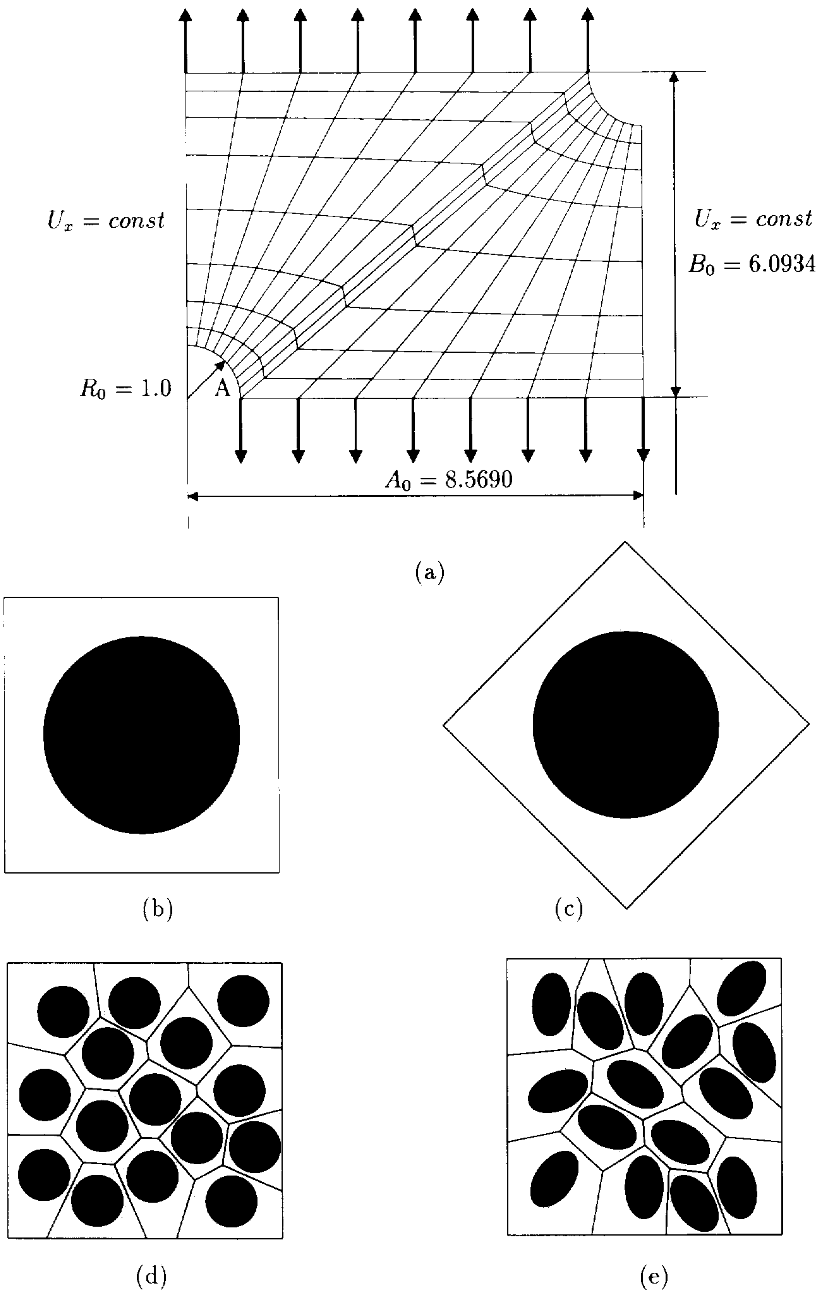

Fig. 19. (a) ABAQUS model for thick plate with circular holes. Various RMEs at 40% volume fraction; (b) square edge packing; (c) square diagonal packing; (d) random packing with 15 circular heterogeneities; (e) random packing with 15 elliptical heterogeneities.

crostructure is significantly higher than the macroscopic stresses. For example, at point A the maximum microscopic effective stress is 160% higher for square edge, 175% higher for square diagonal, 265% higher for random circular and 340% higher for random elliptical packing. An interesting observation is that, though the random distribution models shows more ductile behavior, it gives rise to local regions of significantly higher microscopic stresses. In the analysis of porous materials with large void volume fractions, the interaction between microstructural voids, and consequently the inter-void distances ap-

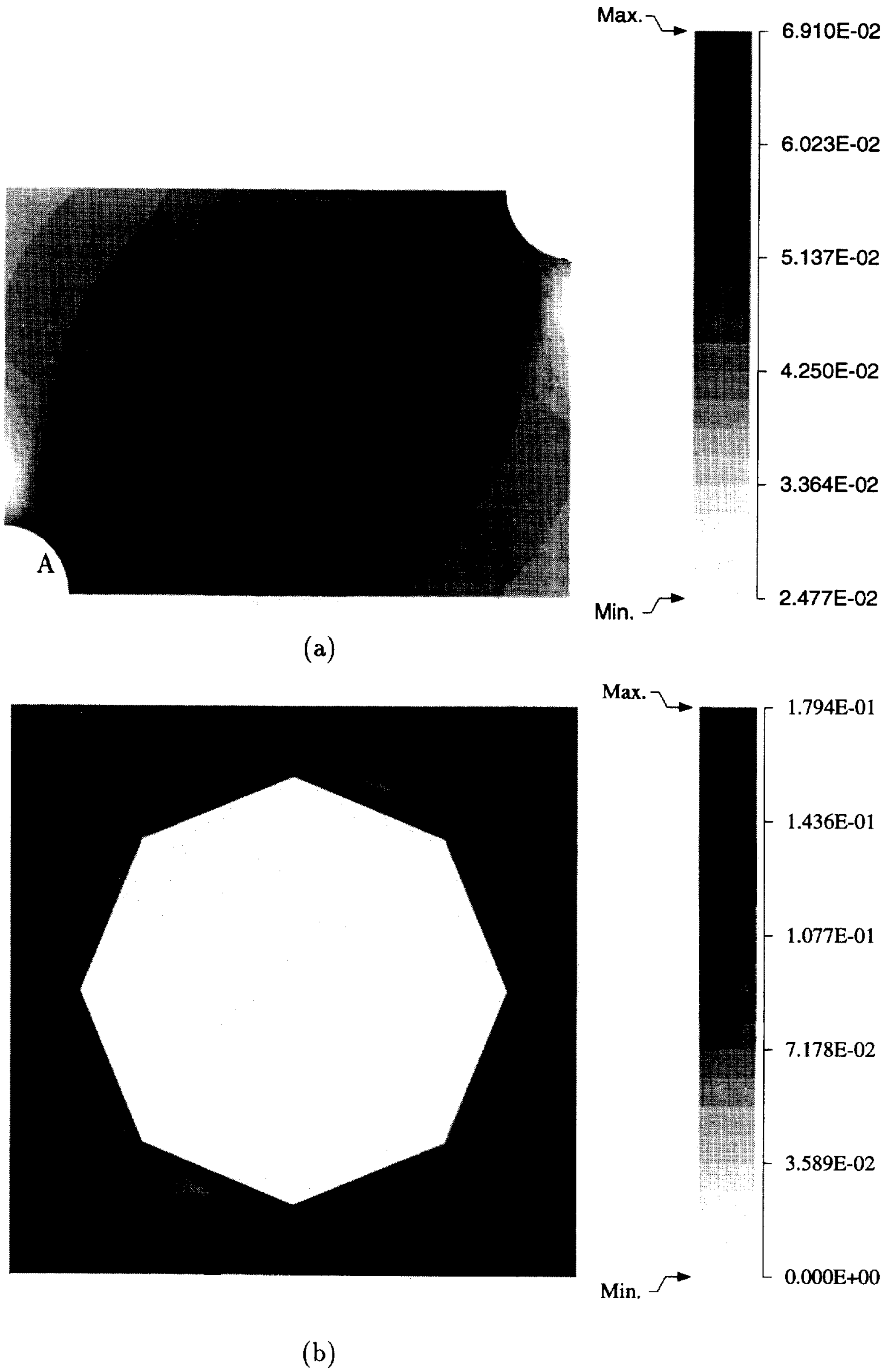

Fig. 20. Von Mises stress distribution for porous material with square edge packing. (a) Macroscopic stress; (b) microscopic stress at point A.

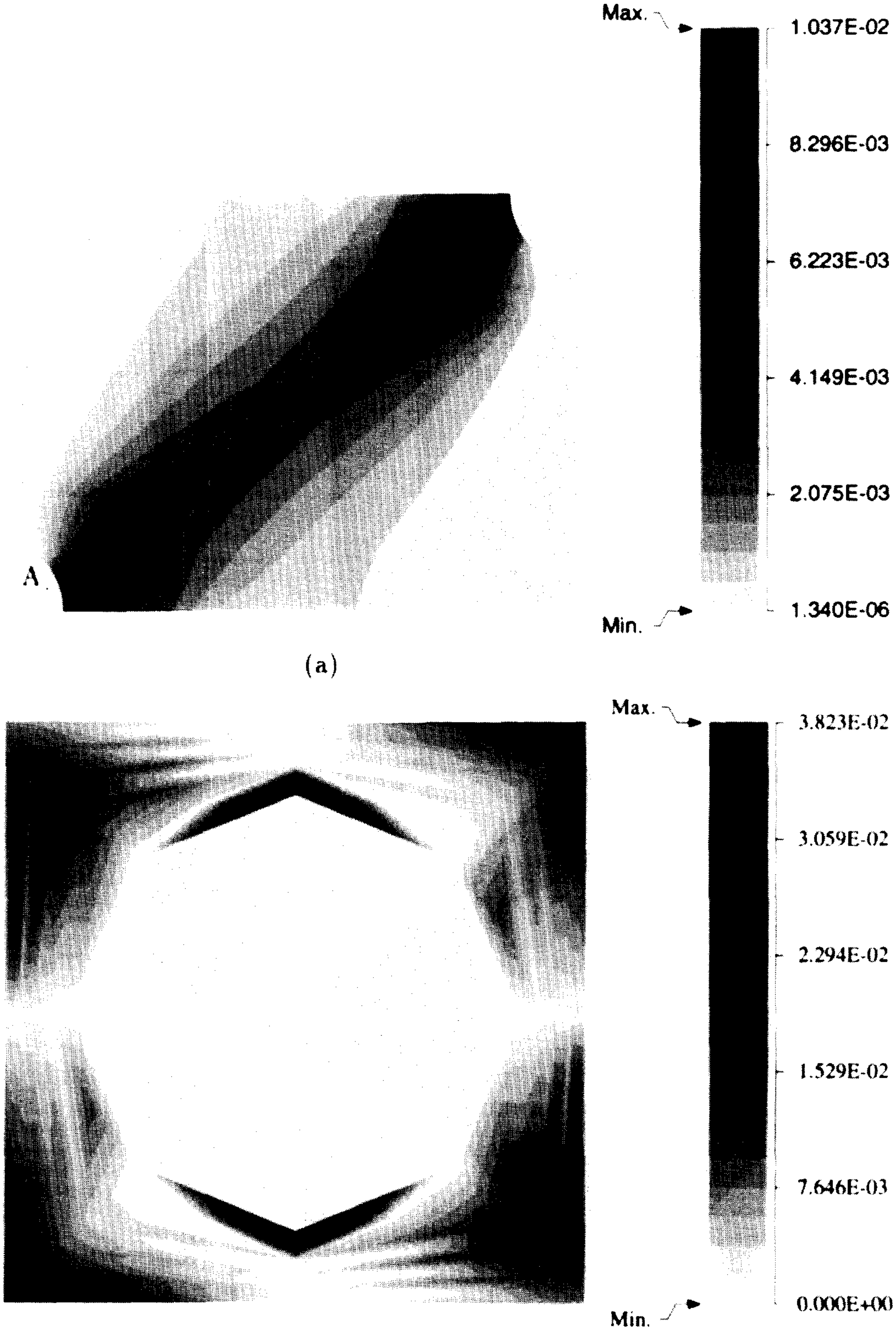

(a)

(b)

Fig. 21. Effective plastic strain distribution for porous material with square edge packing. (a) Macroscopic strain; (b) microscopic strain at point A.

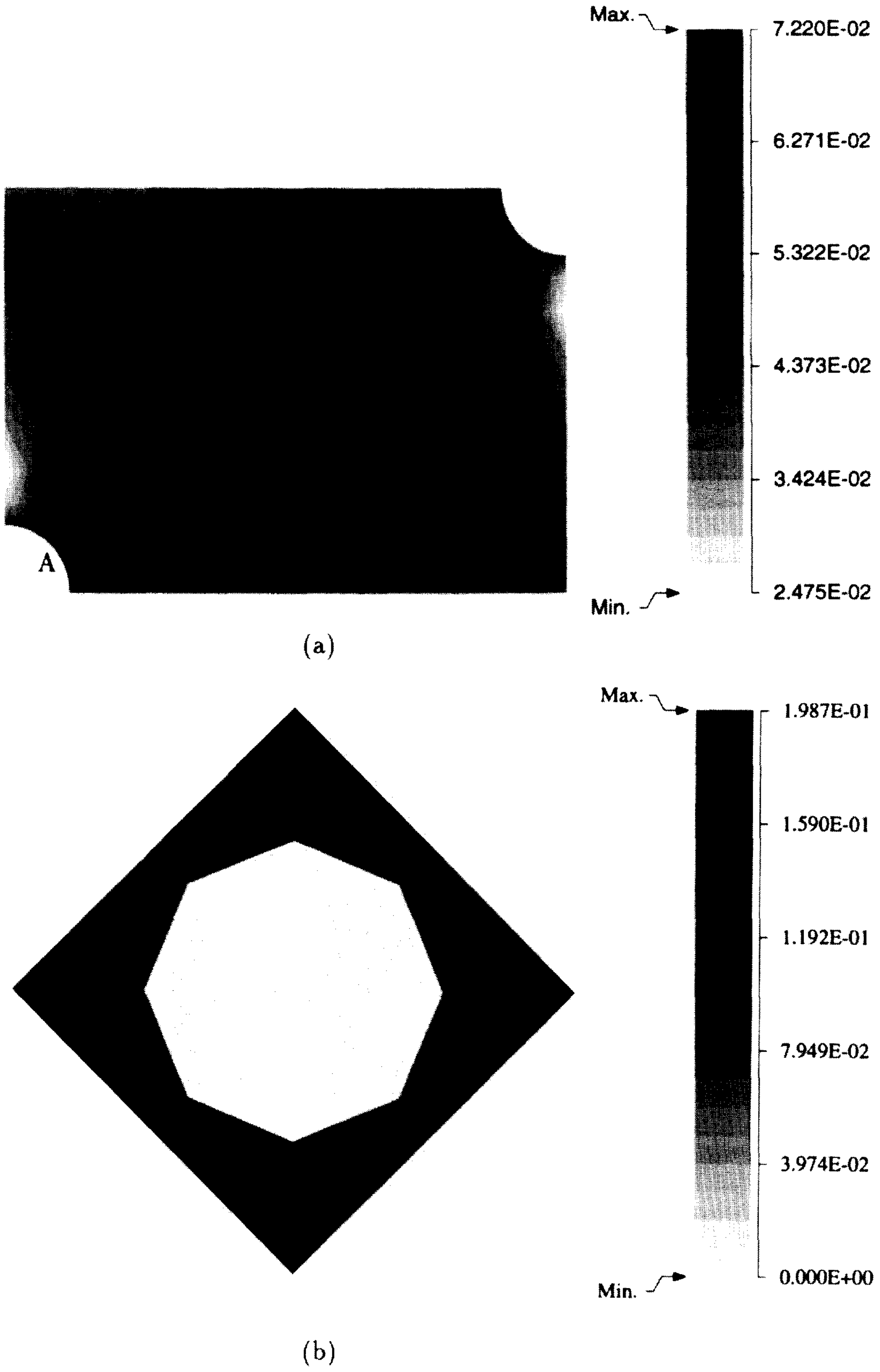

Fig. 22. Von Mises stress distribution for porous material with square diagonal packing. (a) Macroscopic stress; (b) microscopic stress at point A.

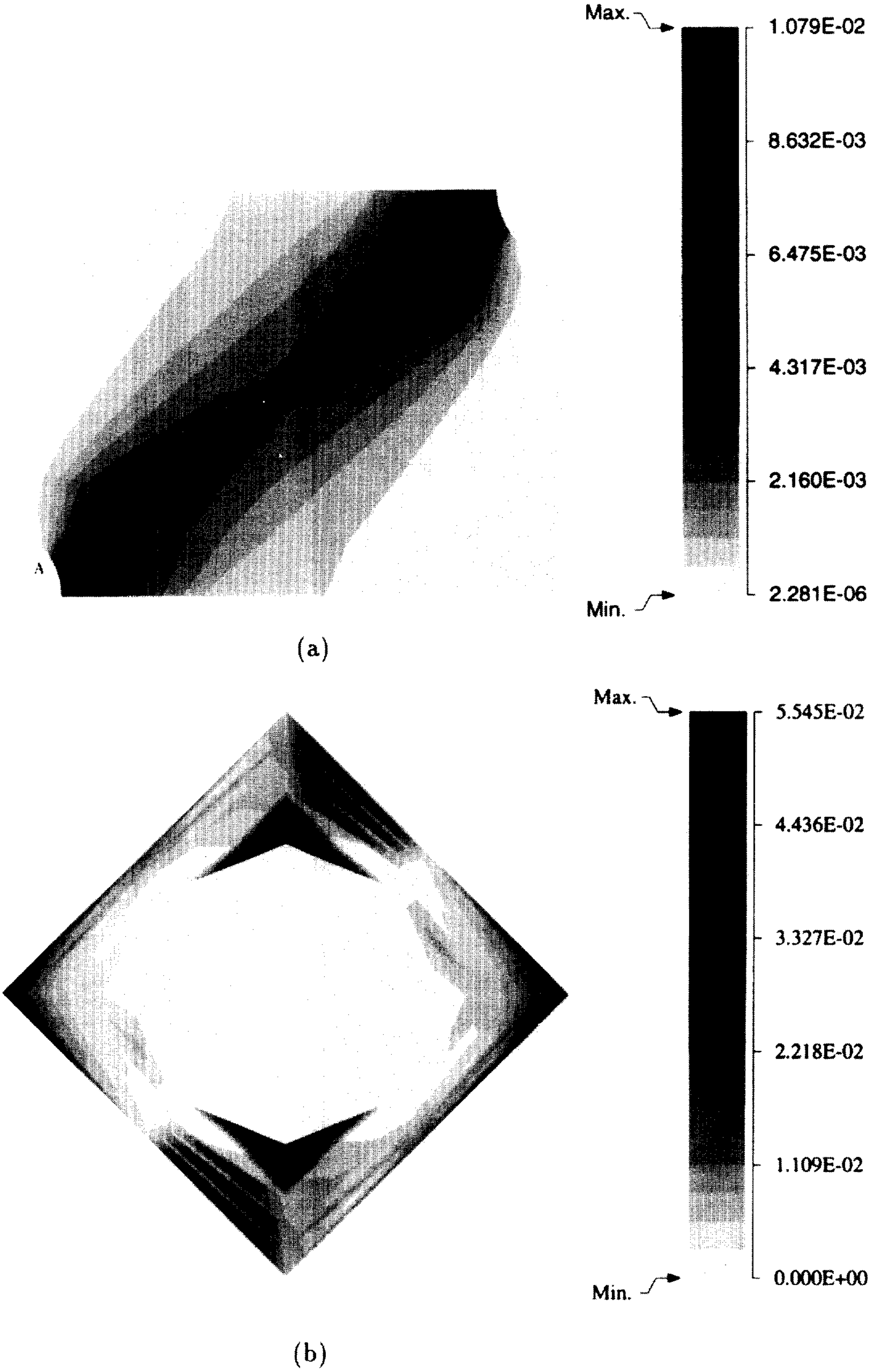

Fig. 23. Effective plastic strain distribution for porous material with square diagonal packing. (a) Macroscopic strain; (b) microscopic strain at point A.

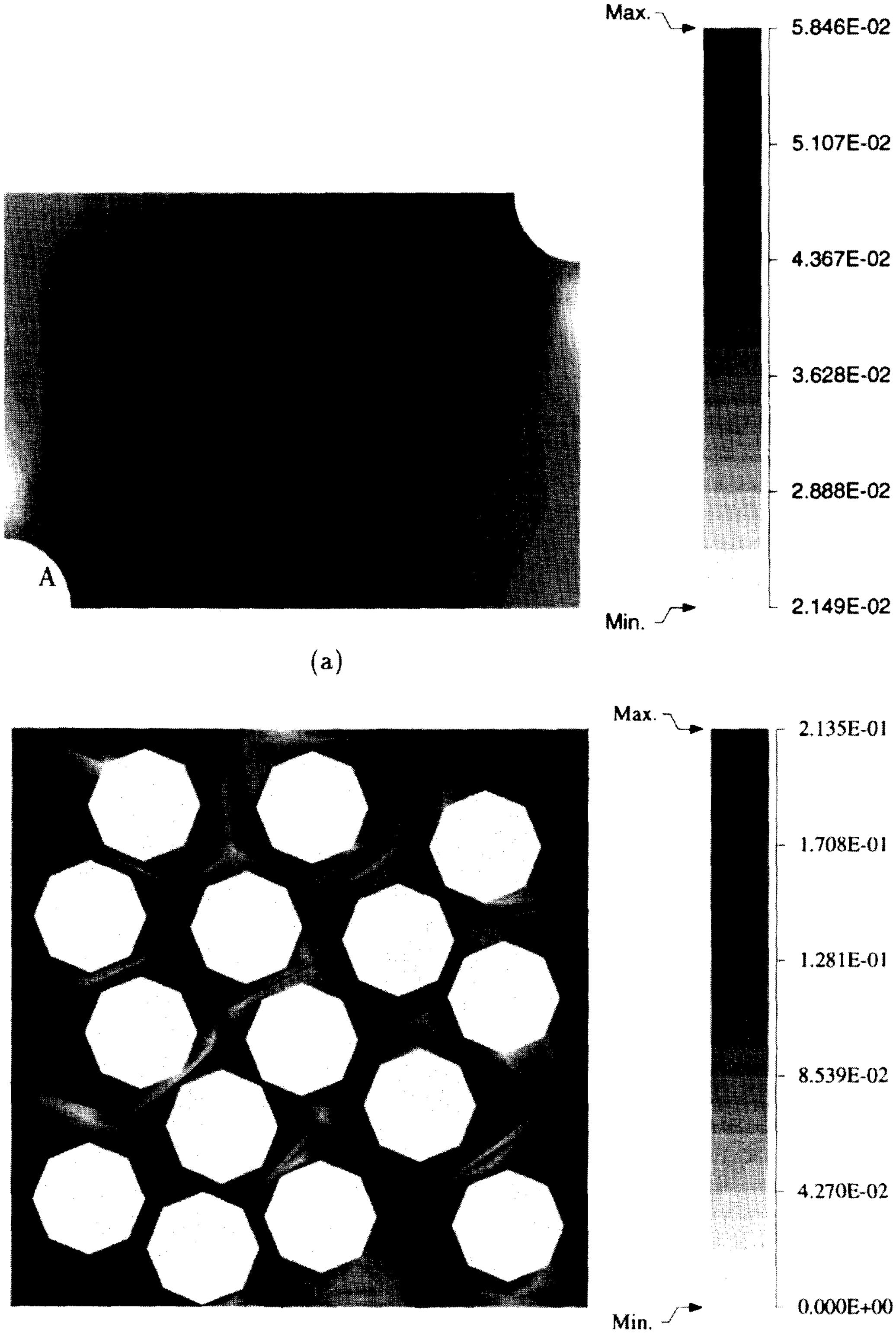

(a)

(b)

Fig. 24. Von Mises stress distribution for porous material with random circular packing. (a) Macroscopic stress; (b) microscopic stress at point A.

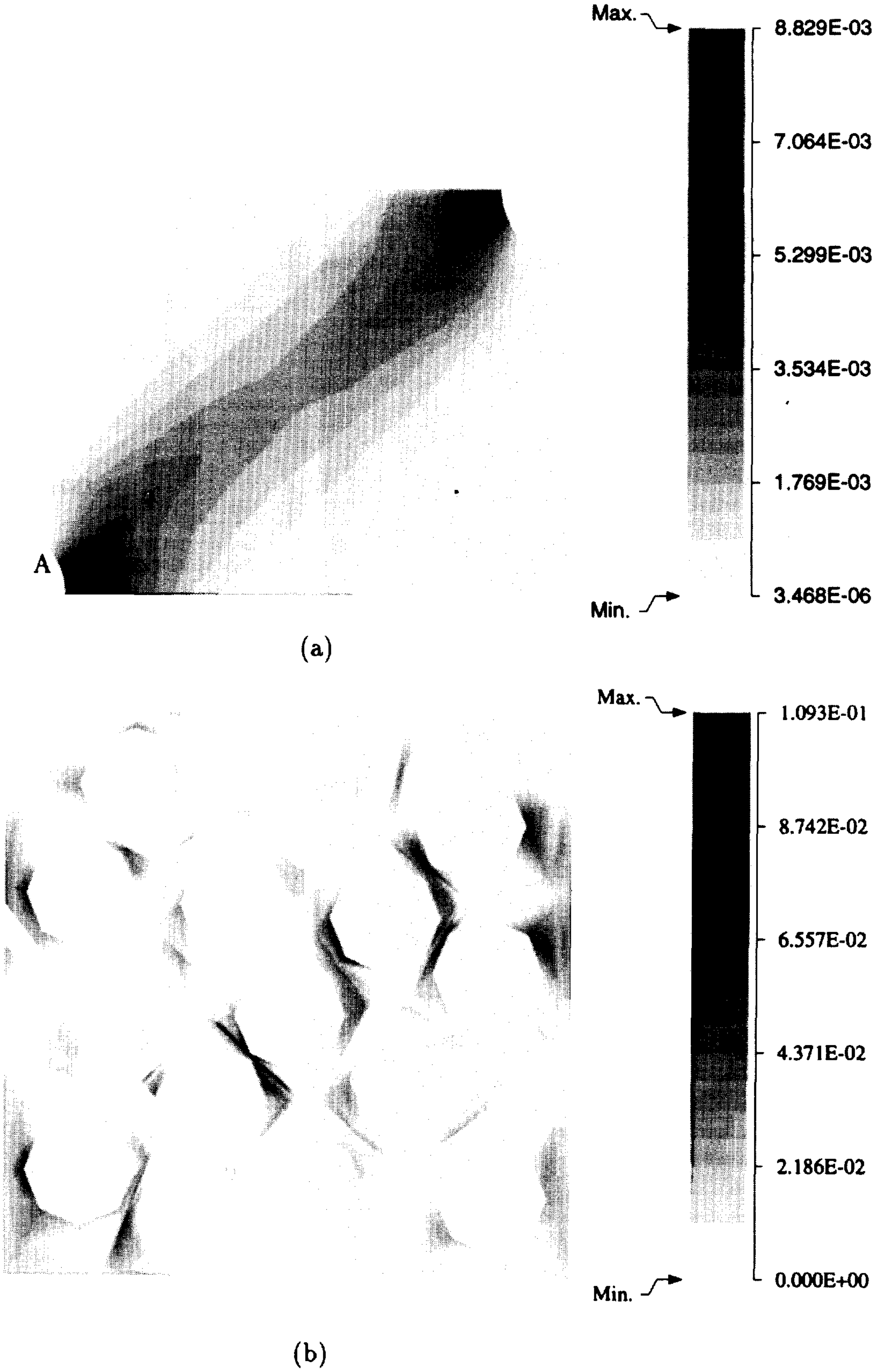

Fig. 25. Effective plastic strain distribution for porous material with random circular packing. (a) Macroscopic strain; (b) microscopic strain at point A.

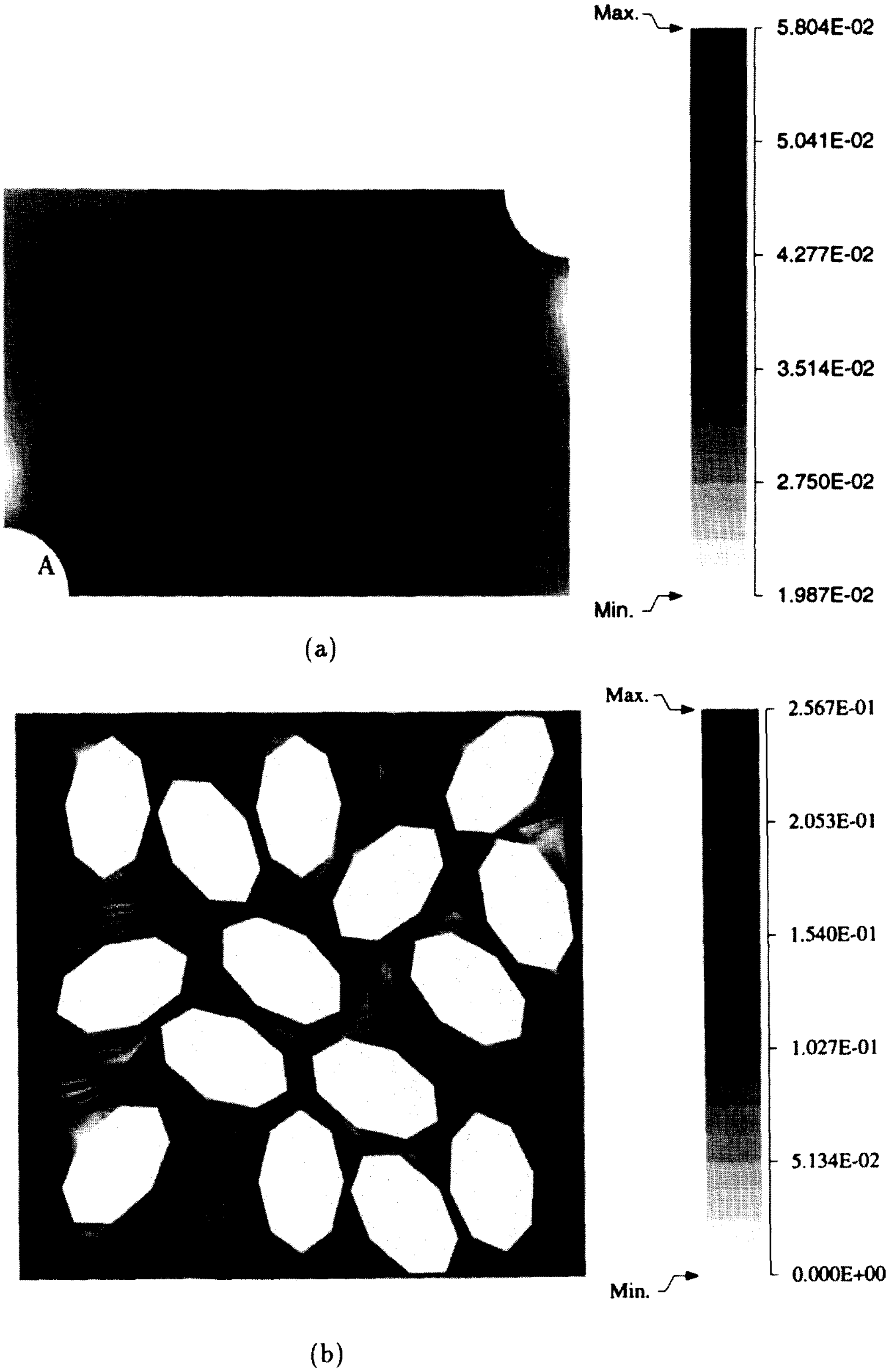

Fig. 26. Von Mises stress distribution for porous material with random circular packing. (a) Macroscopic stress; (b) microscopic stress at point A.

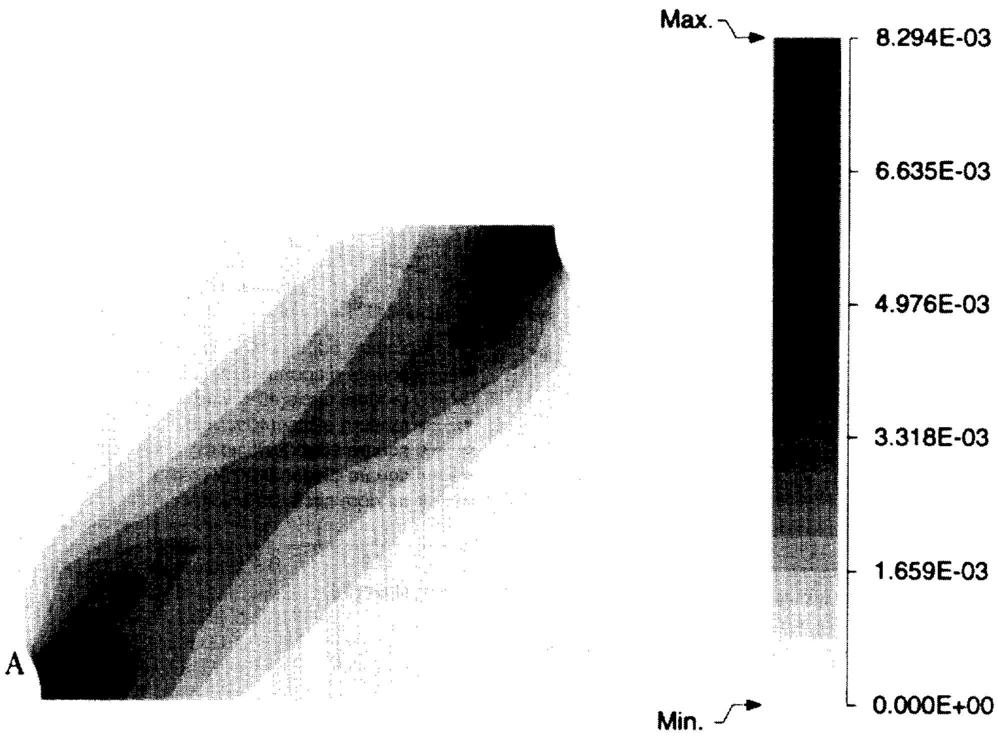

(a)

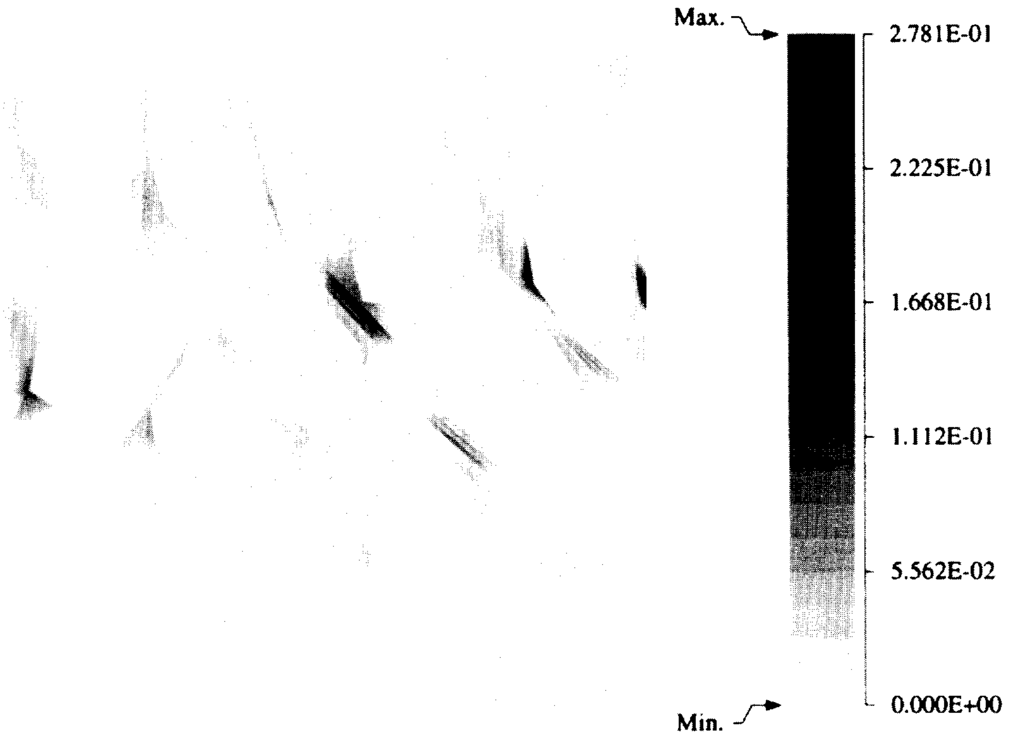

(b)

Fig. 27. Effective plastic strain distribution for porous material with random elliptical packing. (a) Macroscopic strain; (b) microscopic strain at point A.

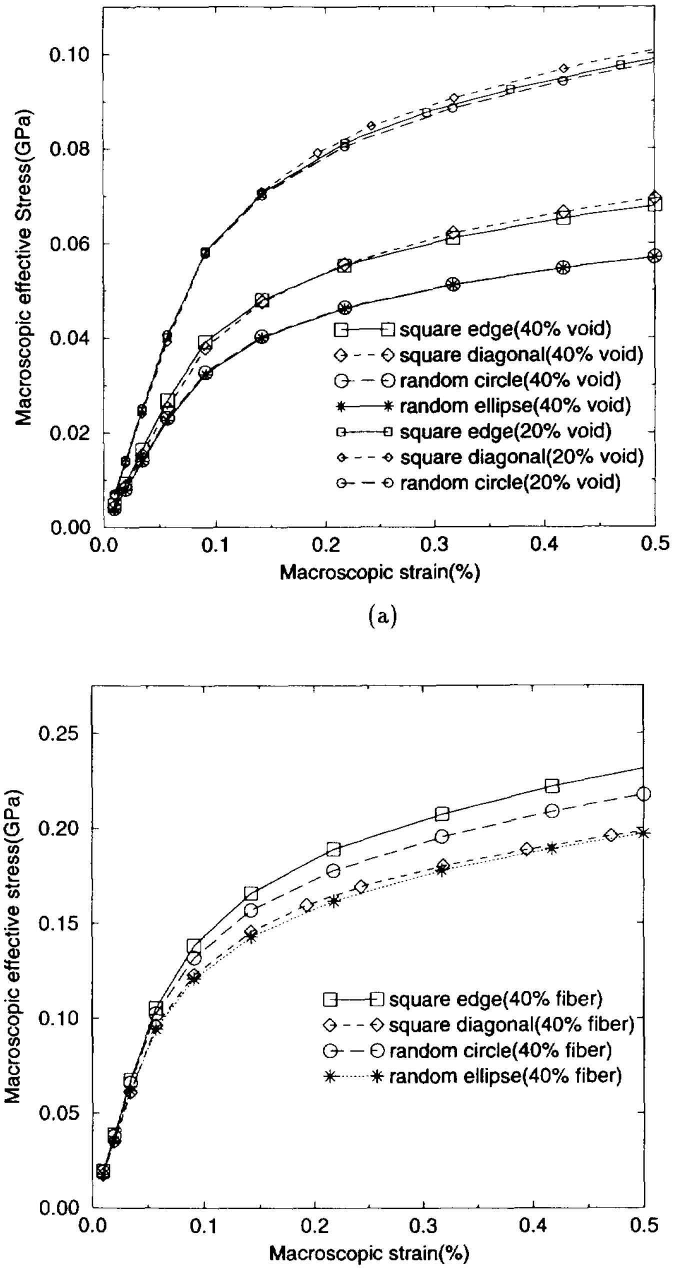

(b)

Fig. 28. Evolution of effective stress with evolving strain at point A in the heterogeneous plate with 40% second phase volume fraction for: (a) porous material; (b) composite material.

pears to play a more dominant role than the arrangement itself, both for macroscopic and microscopic response.

The same problem is considered again with the microstructure changed to a FT/Al composite. The same microstructural morphologies are used with 40% fiber volume fraction. Figs. 29–32 show the effective stress contour plots at the end of loading. The macroscopic plots show that the localization ligament between two macroscopic holes is much less severe and more diffused compared to the porous material.

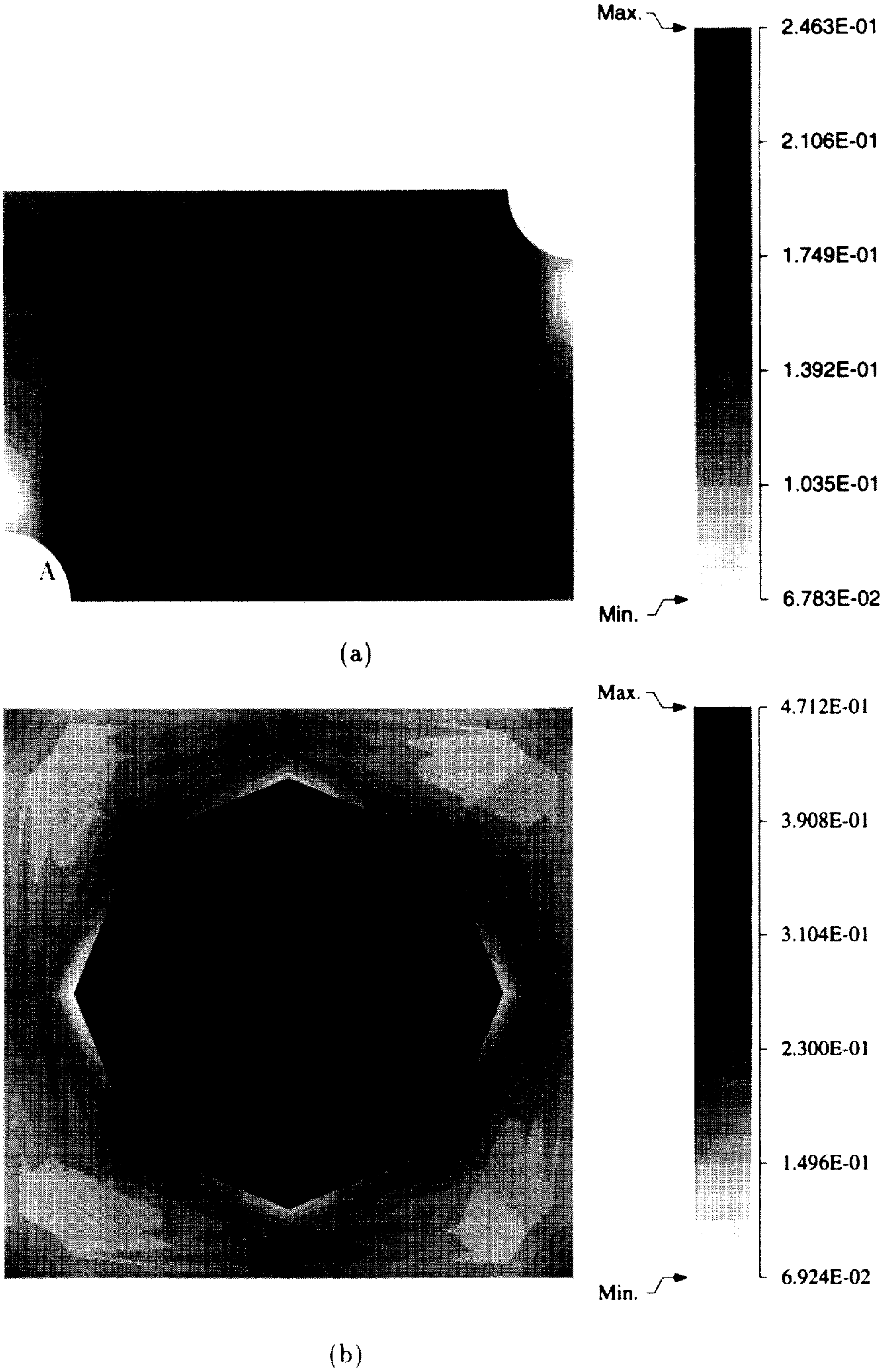

Fig. 29. Von Mises stress distribution for composite material with square edge packing. (a) Macroscopic stress; (b) microscopic stress at point A.

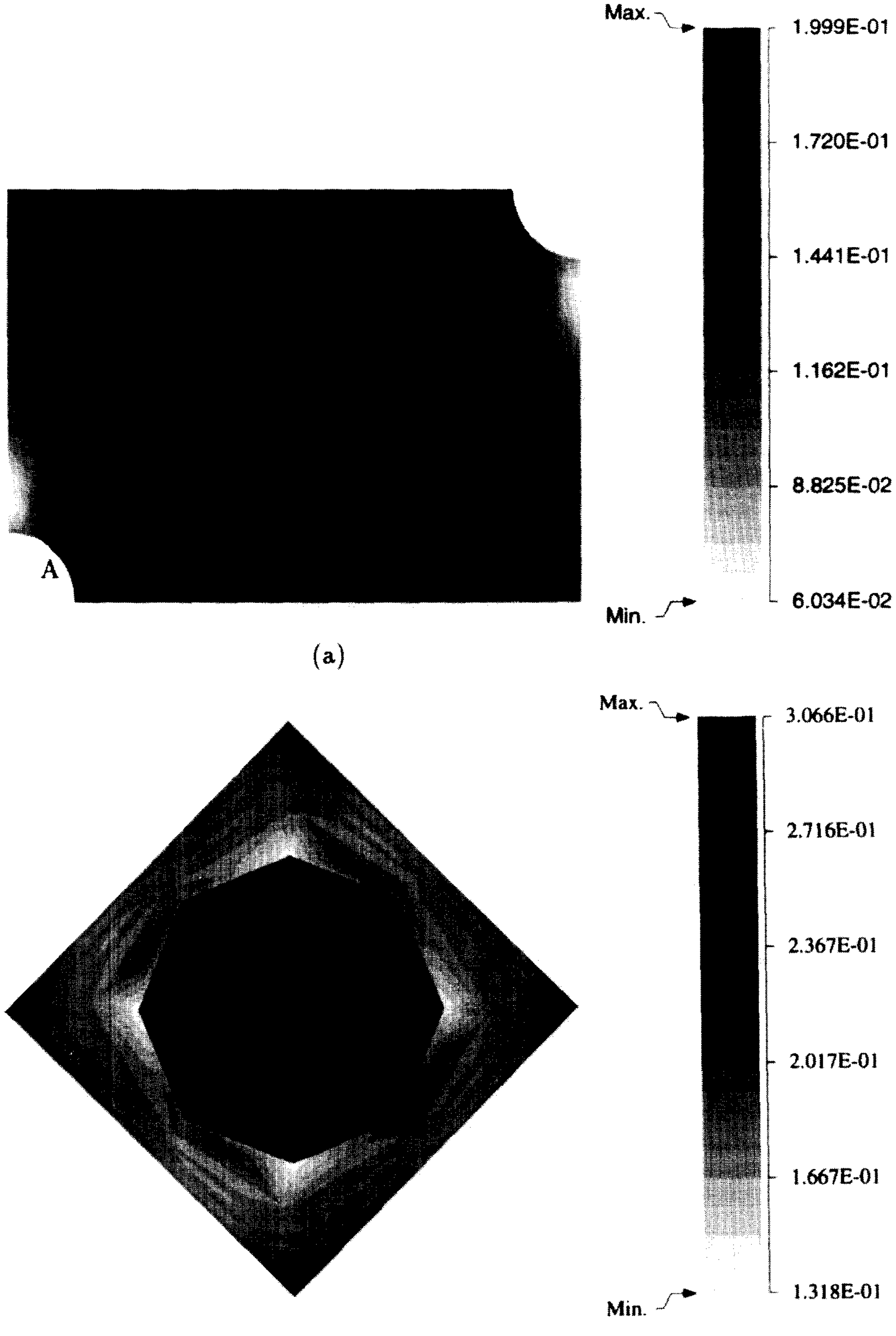

(a)

(b)

Fig. 30. Von Mises stress distribution for composite material with square diagonal packing. (a) Macroscopic stress; (b) microscopic stress at point A.

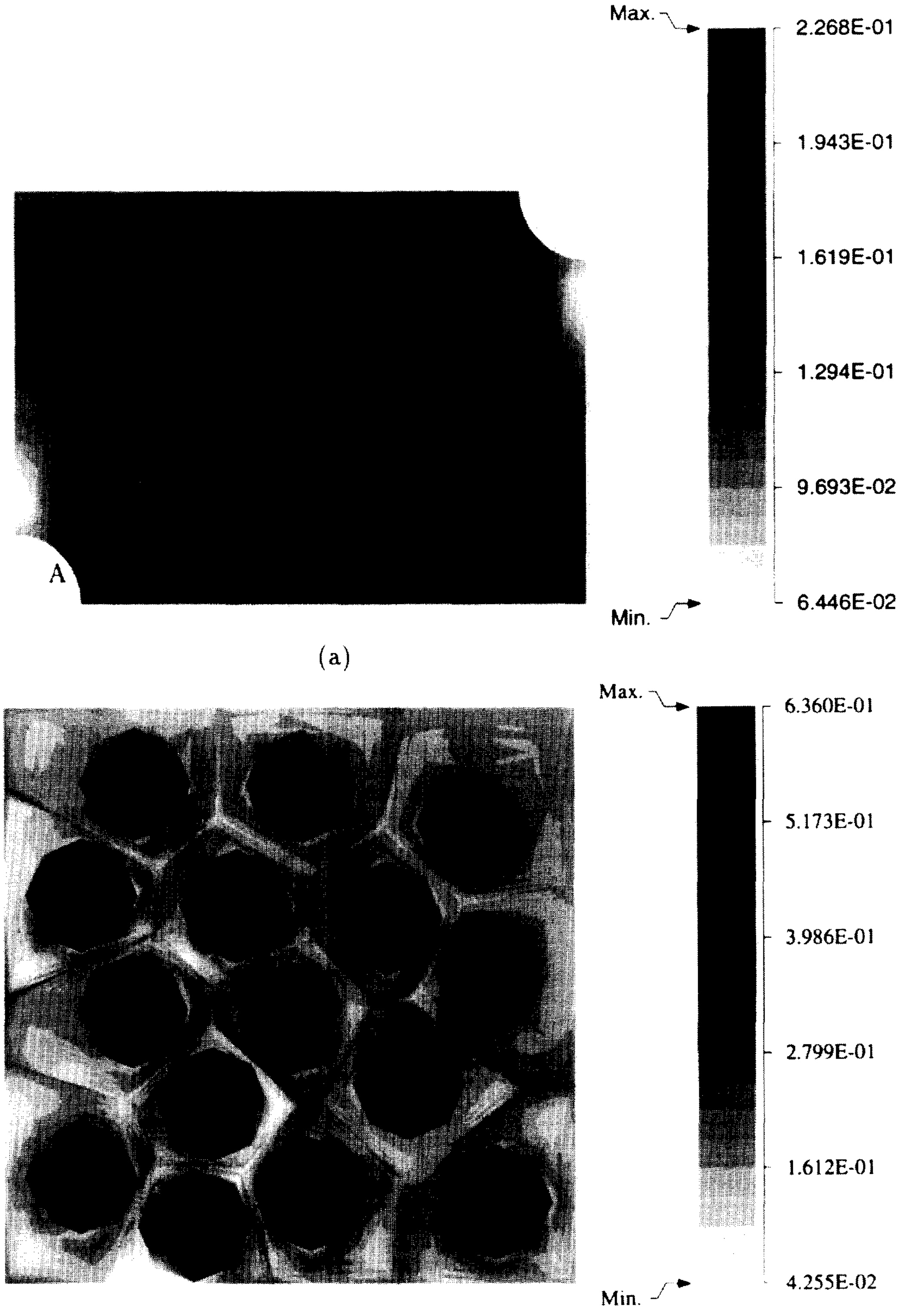

(a)

(b)

Fig. 31. Von Mises stress distribution for composite material with random circular packing. (a) Macroscopic stress; (b) microscopic stress at point A.

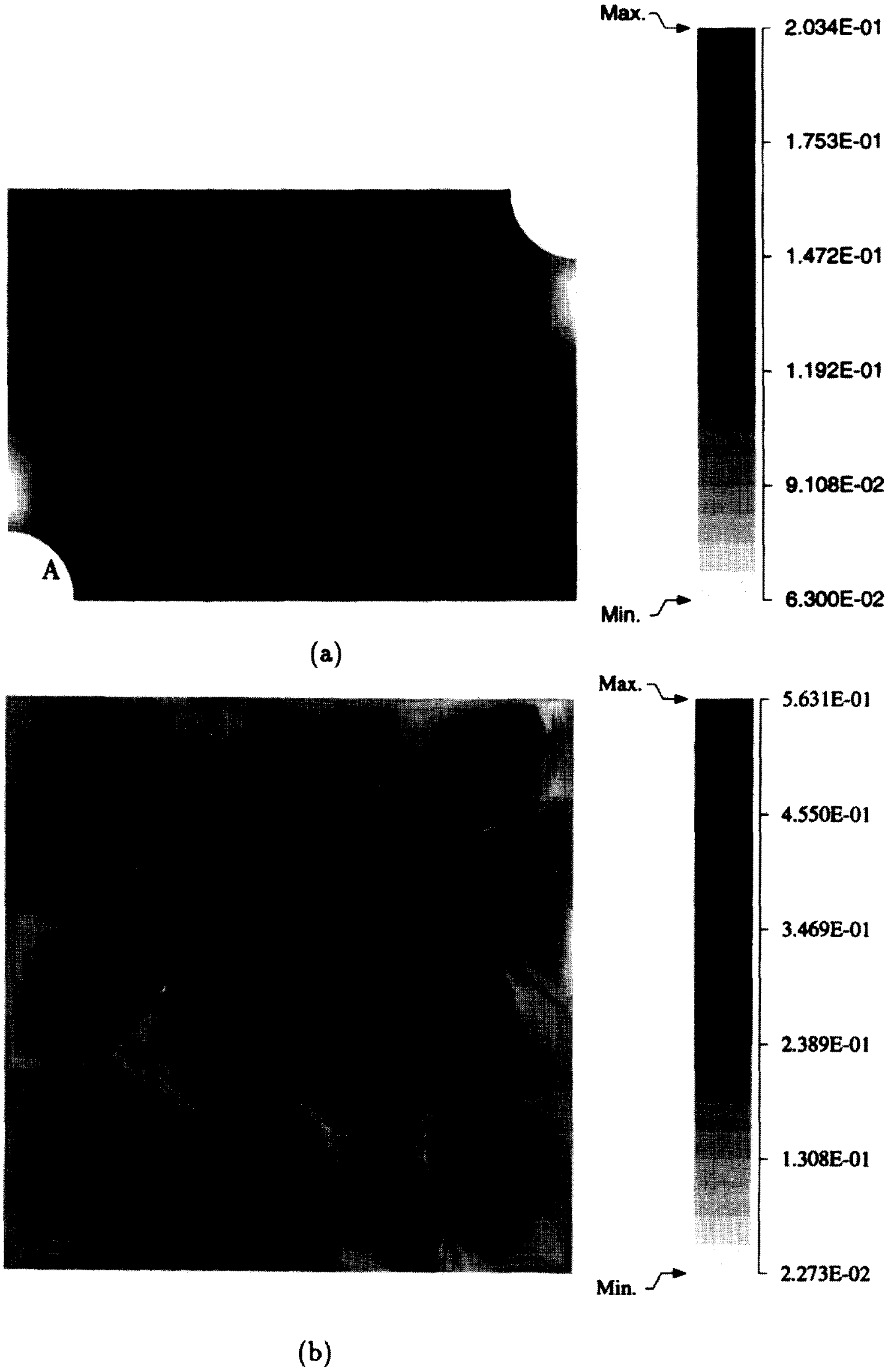

Fig. 32. Von Mises stress distribution for composite material with random circular packing. (a) Macroscopic stress; (b) microscopic stress at point A.

For the same level of macroscopic strain, the square edge packing yields the highest values of effective stress while the square diagonal packing yields the lowest, with the random packings in between. This is also evidenced in the macroscopic stress–strain plot at point *A* in Fig. 28(b). As opposed to the porous microstructure, the arrangement of the composite microstructure has a major effect on the macroscopic response. The distribution pattern is again similar for all RMEs due to the predominantly uniaxial state

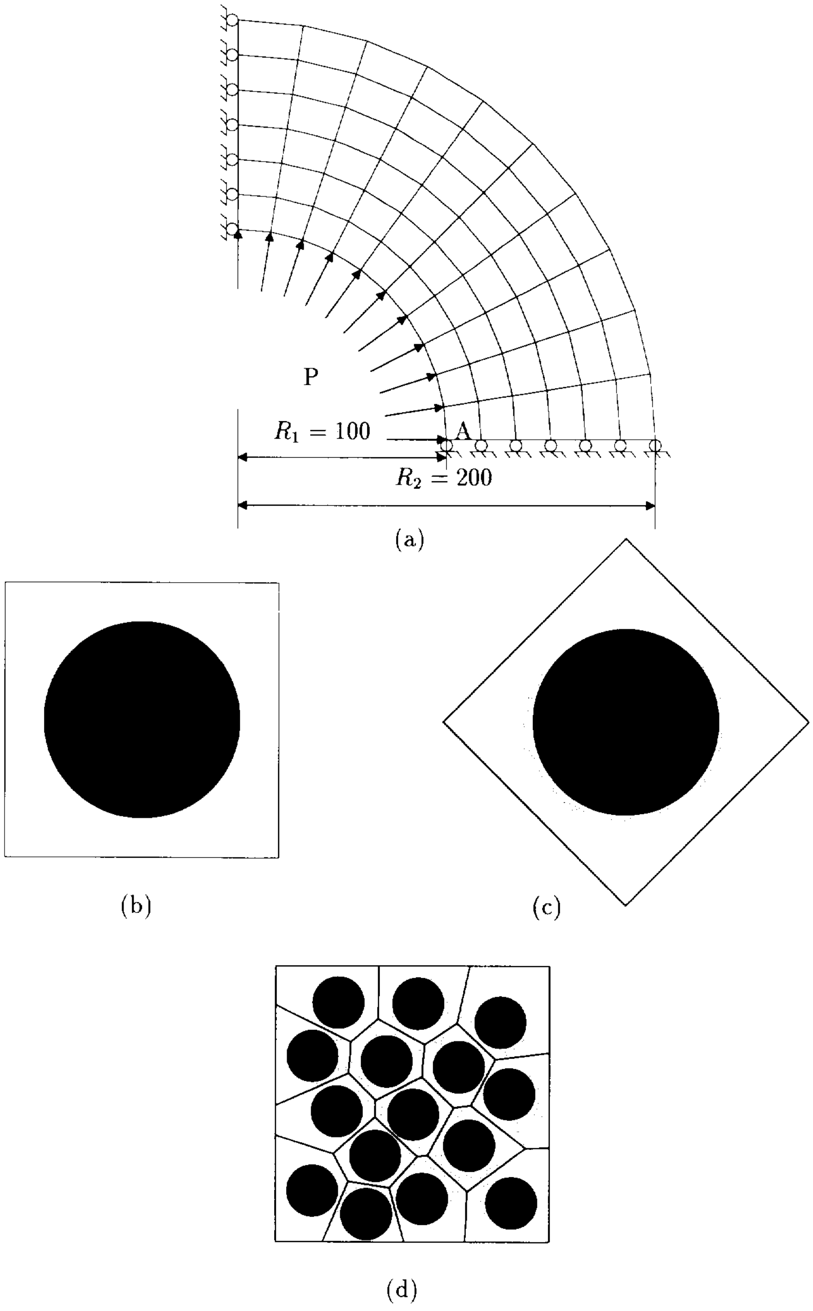

Fig. 33. (a) Macroscopic ABAQUS model of thick cylinder with internal pressure, microscopic VCFE models for: (b) square edge; (c) square diagonal; (d) random packings.

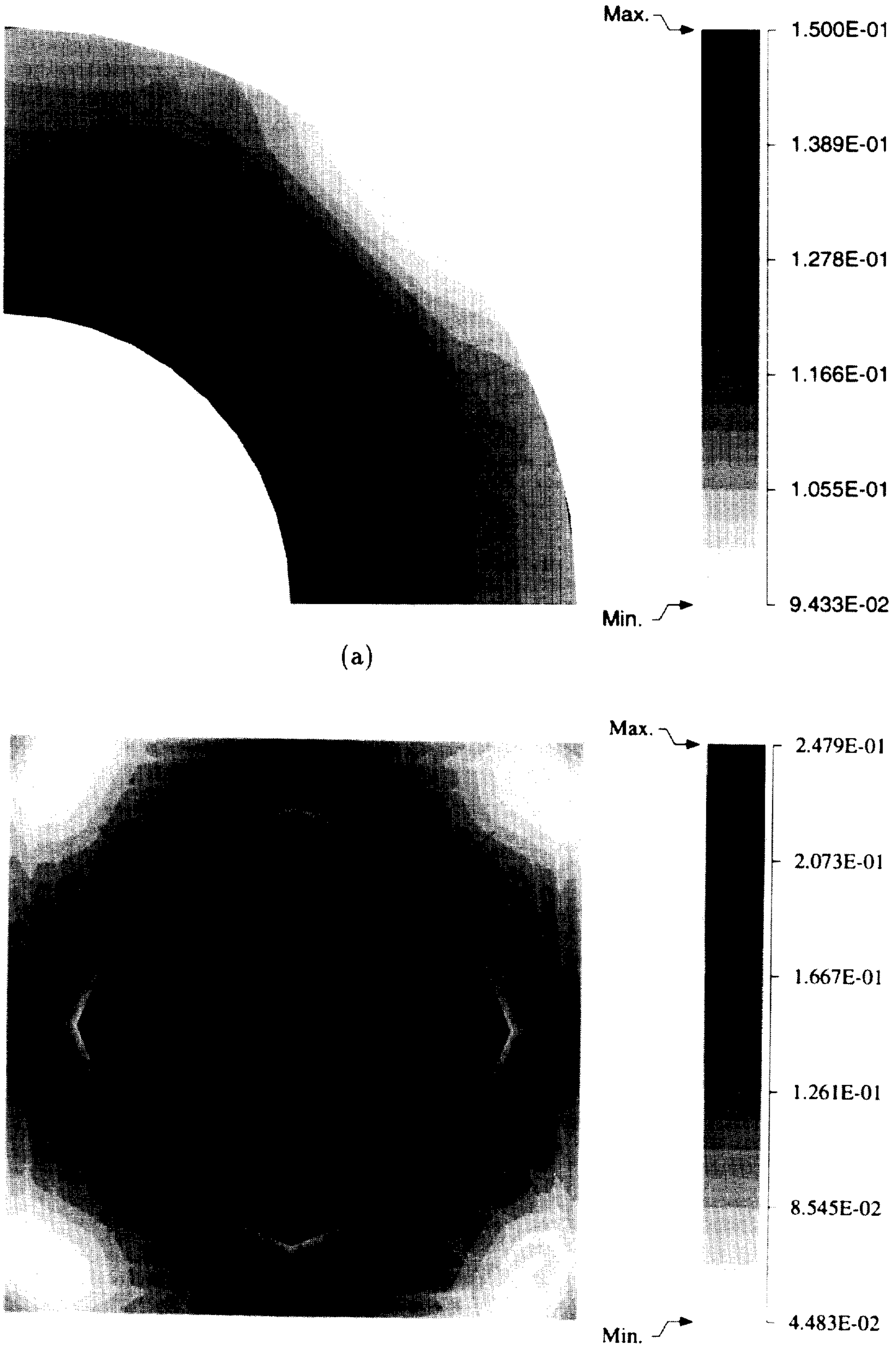

(a)

(b)

Fig. 34. Von Mises stress distribution for square edge packing. (a) Macroscopic stress; (b) microscopic stress at point A.

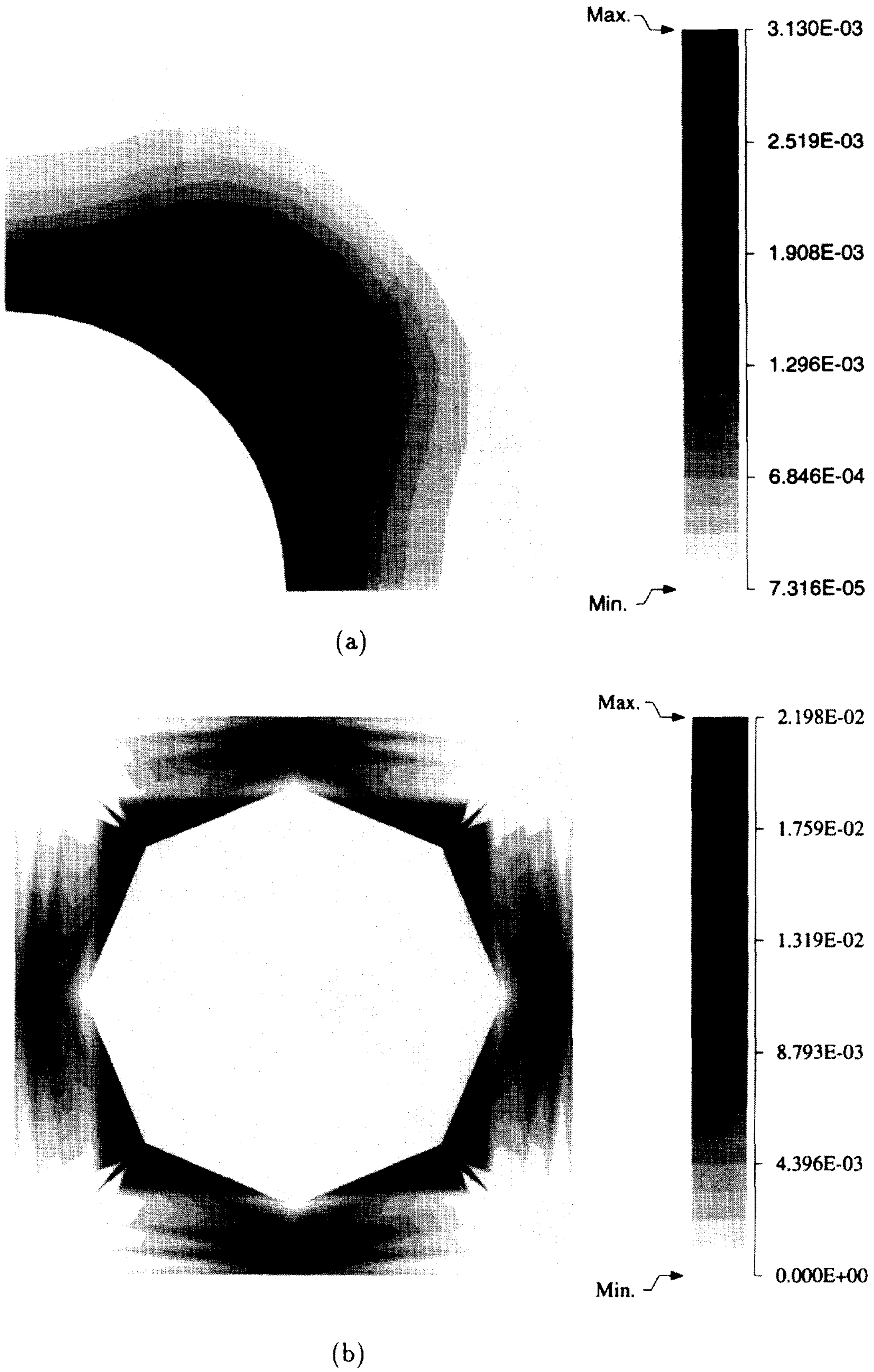

Fig. 35. Effective plastic strain distribution for square edge packing. (a) Macroscopic stress; (b) microscopic stress at point A.

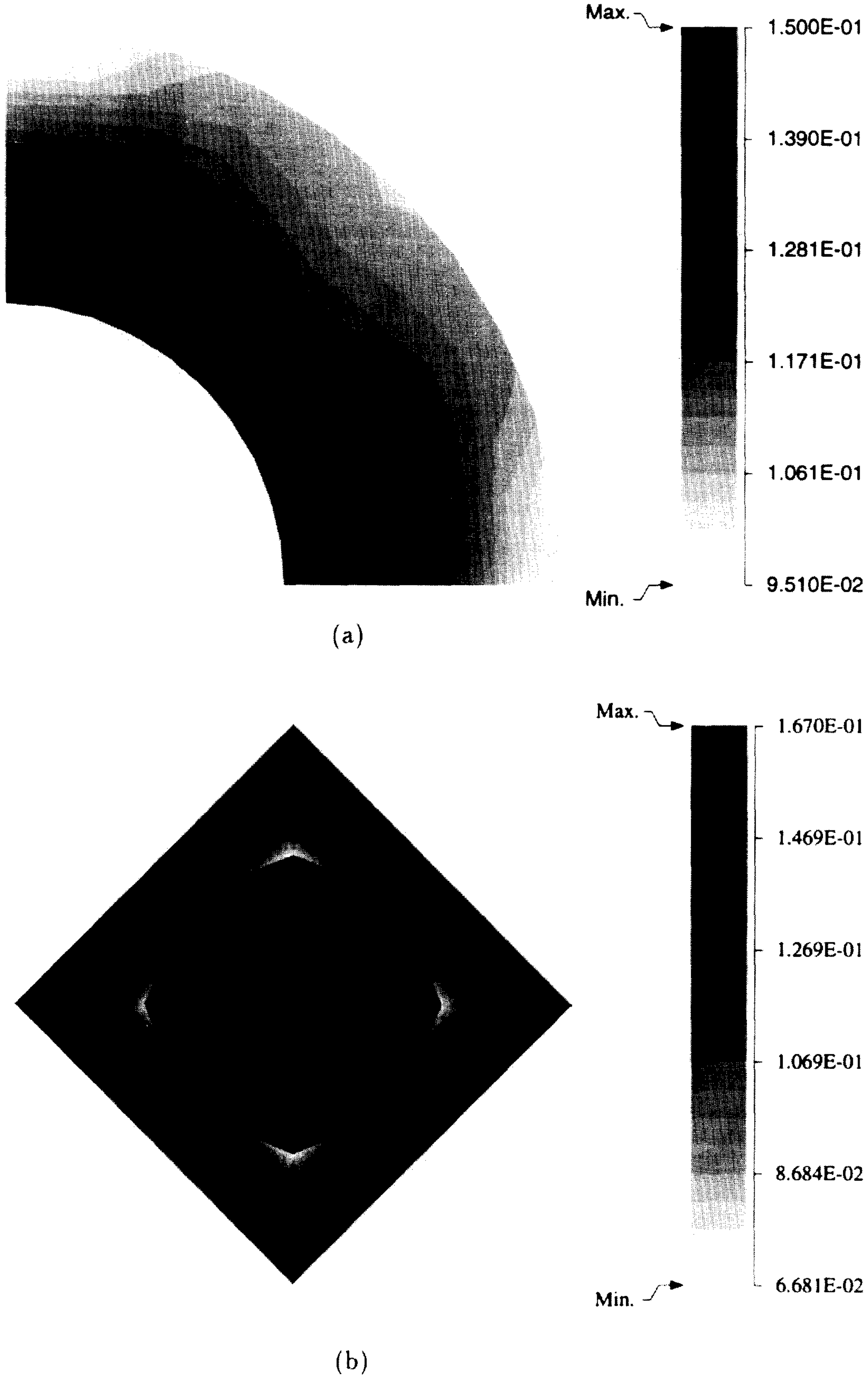

Fig. 36. Von Mises stress distribution for square diagonal packing. (a) Macroscopic stress; (b) microscopic stress at point A.

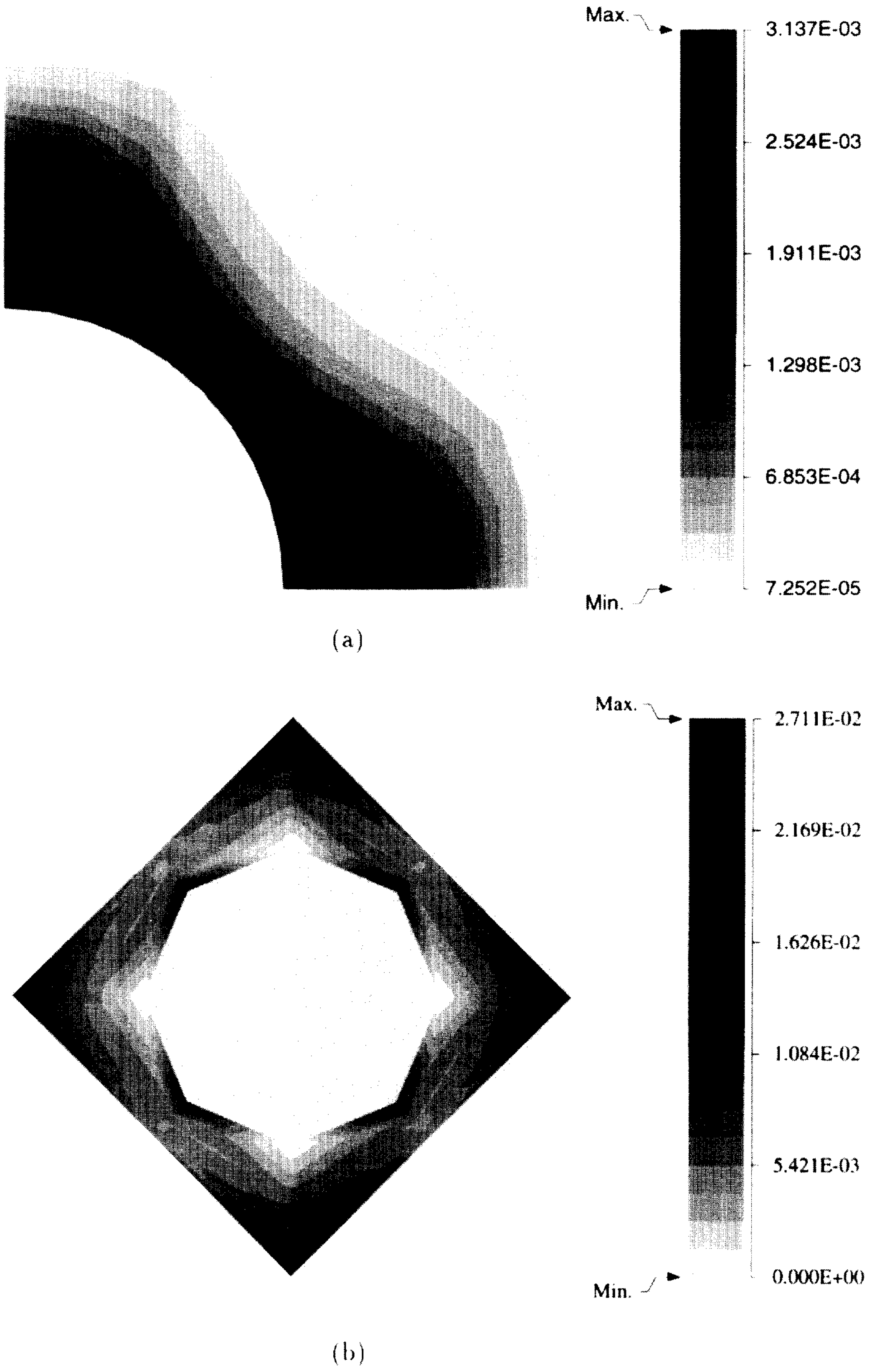

Fig. 37. Effective plastic strain distribution for square diagonal packing. (a) Macroscopic stress; (b) microscopic stress at point A.

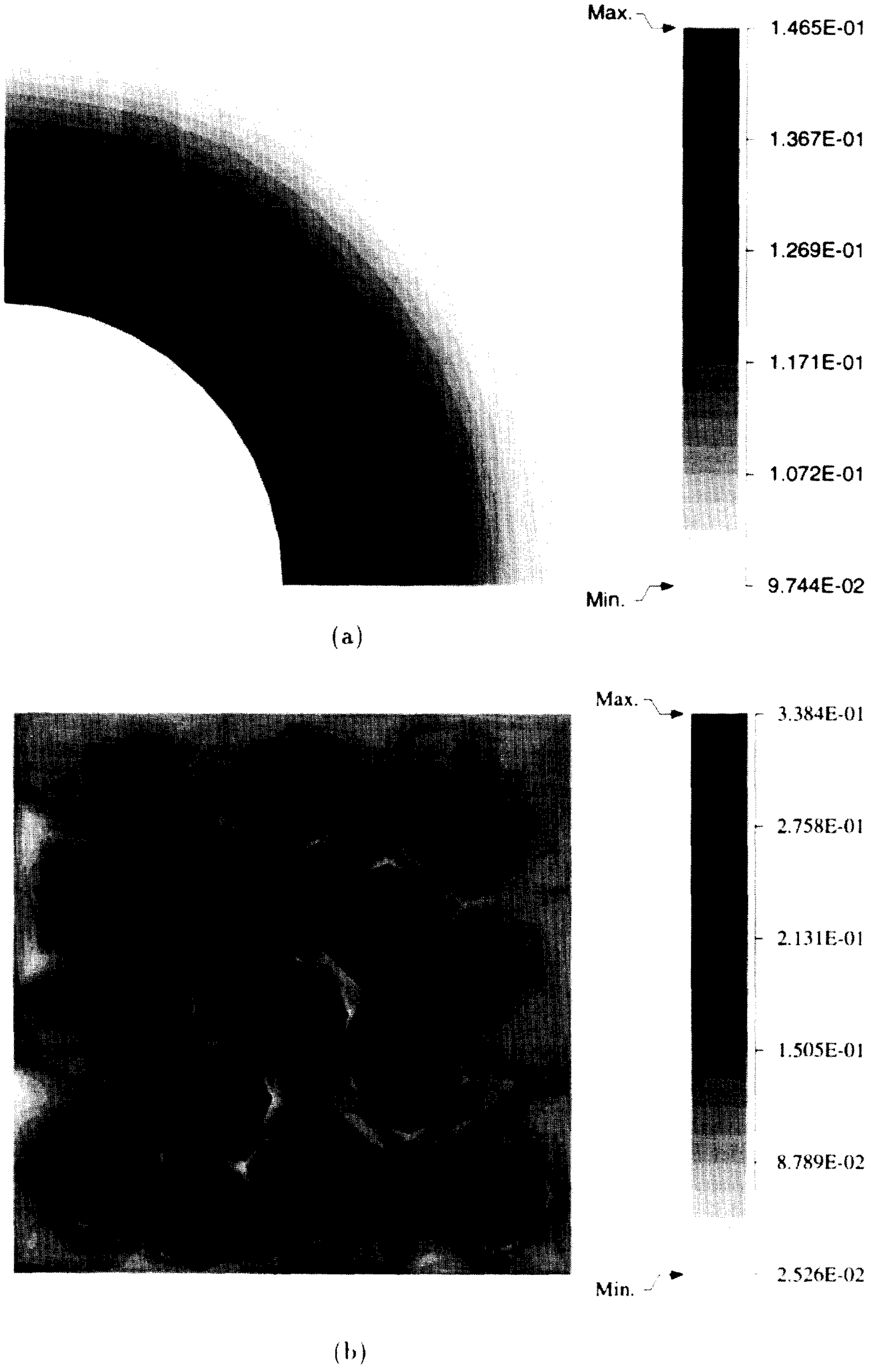

Fig. 38. Von Mises stress distribution for random packing. (a) Macroscopic stress; (b) microscopic stress at point A.

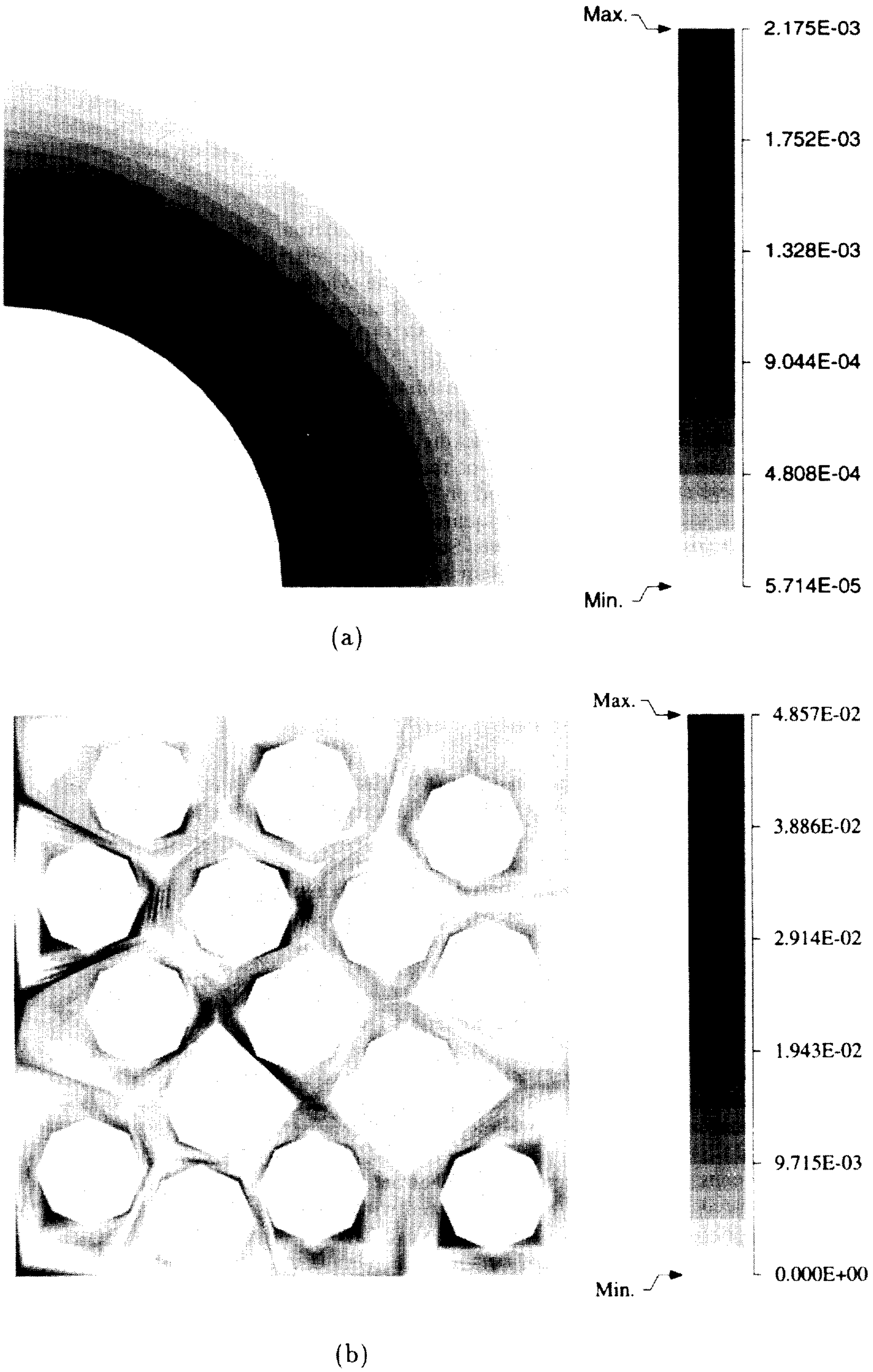

(a)

(b)

Fig. 39. Effective plastic strain distribution for random packing. (a) Macroscopic stress; (b) microscopic stress at point A.

of local stress. The microscopic contour plots reveal that the true stress in the microstructure is significantly higher than the macroscopic counterparts. For example, at point A the maximum microscopic effective stress is 91% higher for square edge, 50% higher for square diagonal, 180% higher for random circular and 177% higher for random elliptical packing. This shows that high stress concentration occurs in certain fibers for random microstructures, and are consequently more susceptible to microstructural damage by fiber cracking or debonding for identical levels of macroscopic stresses.

6.2.2. *Thick cylinder with internal pressure*

In this example a thick composite cylinder is subjected to internal pressure that is increased from 0 to a maximum of 0.1 GPa. Only a quarter of the cylinder is modeled from symmetry considerations with 60 QUAD4 elements in ABAQUS. The dimensions of the cylinder and boundary conditions are shown in Fig. 33(a). The cylinder is analyzed for three different microstructures with 40% fiber volume fraction under plane strain conditions. The microstructural VCFEM models for square edge, square diagonal and random packings are displayed in Figs. 33(b)–(d).

Figs. 34, 36, 38 show contour plots of the Von Mises stress and Figs. 35, 37 and 39 show the corresponding effective plastic strains at macroscopic and microscopic levels at the end of loading. The macroscopic plots show that for the random packing the stresses and strains depend only on the radial location (r) and not the angular location (θ) of the point. However, for the square edge and square diagonal packings, these state variables depend on both the (r) and (θ) coordinates, leading to 'earing' effects. The results of the square edge and square diagonal packings are mutually rotated by 45° as expected from the microstructural orientations. Such earing effects are known to be consequences of anisotropy in the microstructures. In this problem, most macroscopic points are in a triaxial state of state, as opposed to the previous example where most points were in a uniaxial stress state. This amplifies the effect of anisotropy in the macroscopic stress and strain distributions. Effective behavior of the random packing is near isotropic and hence the stress strain distributions are independent of θ coordinates.

7. Conclusions

In this paper, a multiple-scale computational tool (VCFEM-HOMO) is devised for performing elastic-plastic analysis of heterogeneous materials with inclusions and voids in the microstructure. The microscopic analysis is conducted with the Voronoi Cell finite element model while a conventional displacement based FEM code (ABAQUS in this paper) executes the macroscopic analysis. Coupling between the scales is accomplished through the user based UMAT window in ABAQUS, for incorporating the effective constitutive model from VCFEM by asymptotic homogenization.

The VCFEM developed for porous and composite materials in [26, 27] is used in conjunction with homogenization for a wide variety of arbitrary microscopic phase distributions. In this model for small deformation elasto-plasticity, stress functions are motivated from essential characteristics of micromechanics by accounting for the heterogeneity shape and influence. This is achieved by transforming any arbitrary shaped heterogeneity to a unit circle using a mapping similar to the Schwarz–Christoffel conformal mapping. Stress functions are then constructed in terms of mapped coordinates. The introduction of micromechanics consideration tremendously enhances VCFEM accuracy for various microstructures at very moderate computational efforts. The accuracy and efficiency of VCFEM are established by comparing with conventional FEM commercial packages. For a wide range of problems VCFEM delivers very similar accuracy at a considerably low computational effort. This is evidenced by the drastically reduced degrees of freedom needed for convergence, compared with the conventional codes. The D.O.F. ratio varies from as low as 20 for simple microstructures, to even 100 for more complex cases. This translates into a reduction factor of 15–30 in the CPU time for execution, even with a non-optimized research code. Furthermore, user effort required to generate the model is much lower for VCFEM than for many commercial packages.

Numerical examples conducted with VCFEM-HOMO establish the effectiveness of homogenization, when compared with the FEM calculations with constitutive relations from unit cell and effective continuum models. They also point out the limitations of assumptions made in the latter methods, and emphasize situations when coupled multiple scale analysis becomes necessary. The effect of various microscopic arrangements on the mechanical response at the two scales are investigated through these examples. Significant influence is observed in both the microscopic and macroscopic responses. For example, the square edge and square diagonal distributions give severe anisotropic effects, while random distributions are more isotropic at a point in the structure. Multiple scale computations with microscopic FEM models at each element integration point in the structure are in general quite exhaustive. For complex microstructures, the efficiency of microstructural VCFEM makes it possible to realize computations of this magnitude in comparison with conventional FEM. The more complex multiple scale models in this paper took approximately 2–3 CPU hours to run on a CRAY-YMP at the Ohio Supercomputer Center. Though reasonable, major improvements in efficiency of the scale coupling is presently being pursued.

In conclusion, the Voronoi Cell finite element model with asymptotic homogenization (VCFEM-HOMO) emerges as an important tool for analyzing arbitrary microstructures in many materials. It is easily adapted with commercial packages at the structural scale, and this makes it very attractive. A shortcoming of the homogenization method in its present form, is however the incorporation of boundary condition at regions of material discontinuity. Boundary conditions should be applied in the microstructure and not at the macroscopic level as is presently done. The boundary effect can become pronounced in some cases, and then homogenization results become less accurate near the boundary (see [22, 23]). Incorporation in VCFEM-HOMO to avoid the boundary effects is presently being pursued and will be reported in a forthcoming paper.

Acknowledgement

Support of this work by the Unites States Army Research Office through grant No. DAAL03-91-G-0168 (Program Director: Dr. K.R. Iyer), and by the National Science Foundation through grant No. MSS-9301807 (Mechanics and Materials) is gratefully acknowledged. Computer support by the Ohio Supercomputer Center through grant # PAS813-2 is also gratefully acknoweldged.

References

[1] T. Christman, A. Needleman and S. Suresh, An experimental and numerical study of deformation in metal-ceramic composites, Acta Metall. Mater. 37 (1989) 3029–3050.
[2] Z. Hashin and S. Strikman, A variational approach to the theory of the elastic behavior of multiphase materials, J. Mech. Phys. Solids 11 (1963) 127–140.
[3] S. Nemat-Nasser and M. Hori, Micromechanics: Overall Properties of Heterogeneous Materials (North-Holland, Amsterdam, 1993).
[4] H.S. Chen and A. Acrivos, The effective elastic moduli of composite materials containing spherical inclusions at non-dilute concentrations, Int. J. Solids Struct. 14 (1978) 349–364.
[5] R. Hill, A self consistent mechanics of composite materials, J. Mech. Phys. Solids 13 (1965) 213–222.
[6] B. Budiansky, On the elastic modulii of some heterogeneous materials, J. Mech. Phys. Solids 13 (1965) 223–227.
[7] R.M. Christensen and K.H. Lo, Solutions for effective shear properties in three phase sphere and cylinder models, J. Mech. Phys. Solids 27 (1979) 315–330.
[8] G.P. Tandon and G.J. Weng, A theory of particle reinforced plasticity, J. Appl. Mech. 55 (1988) 126–135.
[9] G. Dvorak and Y.A. Bahei-el-din, Plasticity analysis of fibrous composites, J. Appl. Mech. 49 (1982) 327–335.
[10] G. Dvorak and Y.A. Bahei-el-din, A bimodal plasticity theory of fibrous composite materials, Acta Mech. 69 (1987) 219–241.
[11] M. Paley and J. Aboudi, Micromechanical analysis of composites by the generalized cell model, Mech. Mater. 14 (1992) 127–139.
[12] S. Nemat-Nasser, T. Iwakuma and M. Hejazi, On composites with periodic structure, Mech. Mater. 1 (1982) 239–267.
[13] G. Bao, J.W. Hutchinson and R.M. McMeeking, Plastic reinforcement of ductile matrices against plastic flow and creep, Acta Metallur. Mater. 39 (1991) 1871–1882.
[14] V. Tvergaard Analysis of tensile properties for a whisker-reinforced metal matrix composite, Acta Metall. Mater. 38 (1990) 185–194.
[15] A. Benssousan, J.L. Lions and G. Papanicoulau, Asymptotic Analysis for Periodic Structures (North Holland, Amsterdam, 1978).
[16] E. Sanchez-Palencia, Non-homogeneous media and vibration theory, Lecture notes in Physics, 127 (Springer-Verlag, Berlin Heidelberg, 1980).

[17] A. Toledano and H. Murakami, A high order mixture model for periodic particulate composites, Int. J. Solids. Struct. 23(7) (1987) 989–1002.

[18] J.M. Guedes and N. Kikuchi, Preprocessing and postprocessing for materials based on the homogenization method with adaptive finite element methods, Comput. Methods Appl. Mech. Engrg. 83 (1991) 143–198.

[19] P. Suquet, Local and global aspects in the mathematical theory of plasticity, in: A. Sawczuk and G. Bianchi, eds., Plasticity Today—Modeling Methods and Applications (Elsevier, London, 1985).

[20] J.M. Guedes, Non-linear computational model for composite material using homogenization, Ph.D. Dissertation, University of Michigan, MI, 1990.

[21] C.-H. Cheng, Modeling of the elasto-plastic behavior for composite materials using homogenization method, Ph.D. Dissertation, University of Michigan, MI, 1992.

[22] V.Z. Parton and B.A. Kudryavtsev, Engineering Mechanics of Composite Structure (CRC Press, Boca Raton, FL, 1993).

[23] S.J. Hollister and N. Kikuchi, A comparison of homogenization and standard mechanics analyses for periodic porous composites, Comput. Mech. 10 (1992) 73–95.

[24] N.S. Bakhvalov and G.P. Panasenko, Homogenization in periodic media, Mathematical Problems of the Mechanics of Composite Materials, Nauka, Moscow, 1984.

[25] F. Devries, H. Dumontet, G. Duvant and F. Lene, Homogenization of damage for composite structures, Int. J. Numer. Methods Engrg. 27 (1989) 285–298.

[26] S. Ghosh and S. Moorthy, Elastic-plastic analysis of arbitrary heterogeneous materials with the Voronoi cell finite element method, Comput. Methods Appl. Mech. Engrg. 121 (1995) 373–409.

[27] S. Moorthy and S. Ghosh, A model for analysis of arbitrary composite and porous microstructures with Voronoi cell finite elements, Int. J. Numer. Mech. Engrg., in press.

[28] S. Ghosh, K. Lee and S. Moorthy, Multiple scale analysis of heterogeneous elastic structures using homogenization theory and Voronoi cell finite element method, Int. J. Solids Struct. 32(1) (1995) 27–62.

[29] S. Ghosh and Y. Liu, Voronoi cell finite element method for micropolar thermo-elastic heterogeneous materials, Int. J. Numer. Methods Engrg. 38(8) (1995) 1361–1398.

[30] S. Ghosh and S.N. Mukhopadhyay, A two dimensional automatic mesh generator for finite element analysis of random composites, Comput. Struct. 41 (1991) 245–256.

[31] ABAQUS/Standard User's Manual, Version 5.4 Hibbit Karlsson and Sorensen Inc., 1994.

[32] P. Suquet, Elements of homogenization theory for inelastic solid mechanics, in: E. Sanchez-Palencia and A. Zaoui, eds., Homogenization Techniques for Composite Media (Springer-Verlag, New York, 1987) 194–278.

[33] T.H.H. Pian, Derivation of element stiffness matrices by assumed stress distribution, AIAA J. 2 (1964) 1333–1336.

[34] S.N. Atluri, On the hybrid finite element model for incremental analysis of large deformation problems, Int. J. Solids Struct. 9 (1973) 1177–1191.

[35] S.N. Atluri, On some new general and complimentary energy theorems for the rate problems in finite strain, classical elastoplasticity, J. Struct. Mech. 8(1) (1980) 61–92.

[36] P. Tong, T.H.H. Pian and S.J. Lasry, A hybrid-element approach to crack problems in plane elasticity, Int. J. Numer. Methods Engrg. 7 (1973) 197–308.

[37] R. Piltner, Special finite elements with holes and internal cracks, Int. J. Numer. Methods Engrg. 21 (1973) 197–308.

[38] V. Tvergaard, Influence of voids on shear band instability under plane strain conditions, Int. J. Fracture 17 (1981) 389–407.

[39] V. Tvergaard, Material failure by void coalescence in localized shear bands, Int. J. Solids Struct. 18 (1982) 659–672.

[40] N. Aravas, On the numerical integration of a class of pressure-dependent plasticity models, Int. J. Numer. Methods Engrg. 24 (1987) 1395–1416.

[41] Y.H. Zhao and G.J. Weng, Theory of plasticity for inclusion and fiber-reinforced composite in: G.J. Weng, M. Taya and H. Abe, eds., Micromechanics and Inhomogeneity, The Toshio Mura Anniversary Volume (Springer-Verlag, Berlin, 1989) 599–622.

[42] D.F. Adams, Inelastic analysis of a unidirectional composite subjected to transverse normal loading, J. Comput. Mater. 4 (1970) 310–328.